

# Ludwig-Maximilians-University



Master Thesis:

On anisotropic thermal conduction in cluster  
cooling flows

---

submitted by: Alexander Arth (#8045125)      submitted at: September 11, 2013      submitted to: Prof. Dr. Harald Lesch



# Ludwig-Maximilians-Universität



Master Arbeit:

Zur anisotropen Wärmeleitung in Cluster Cooling  
Flows

abgegeben von:

abgegeben am:

eingereicht bei:

---

Alexander Arth (#8045125) September 11, 2013 Prof. Dr. Harald Lesch



## *Abstract*

Latest X-ray observations revealed the importance of cooling flows in galaxy clusters. However current cosmological simulations of cluster formation are not resolving the cooling flows in much details.

In this work we will use the massively parallel TreePM/SPMHD Code GADGET-3 originally developed by Springel et al. In 2004 Jubelgas et al. included an isotropic implementation of thermal conduction into GADGET for cluster formation simulations. They used the classical Spitzer conduction and also considered the effect of saturation in low density gas. With this implementation the temperature profile of the simulated clusters was definitely changed, although it's detailed structure was lost.

Theoretical discussions of observations show, that the classical Spitzer conduction is not sufficient to describe the cooling flows in galaxy clusters. Binney & Cowie already suggested ideas of further development in 1981. They considered the effect of magnetic fields on different scales in the clusters and showed, that heat flows perpendicular to magnetic fields should be suppressed.

Therefore we want to derive a new numerical scheme for anisotropic heat conduction in SPH. In this thesis we will discuss several approaches to achieve this and present test cases as well as results from galaxy cluster simulations regarding our new implementation in GADGET-3.

We find that anisotropic heat conduction is very similar to overall suppressed isotropic conduction. For a rather small galaxy cluster we do not find drastic differences between these both cases.

This has to be further investigated by simulating more galaxy clusters for a better statistics. One needs to have a closer look especially at more massive clusters to maximize the effect of anisotropic conduction for a more detailed analysis.

# Contents

<b>1</b>	<b>Galaxy Clusters and cooling flows</b>	<b>1</b>
1.1	Physics of the ICM . . . . .	2
1.2	The Perseus cluster in different wavebands . . . . .	11
1.3	Possible solutions of the cooling flow problem . . . . .	19
<b>2</b>	<b>Thermal conduction and magnetic fields</b>	<b>25</b>
2.1	Isotropic thermal conduction . . . . .	25
2.2	Anisotropic thermal conduction . . . . .	29
2.3	Implications on cluster cooling flows . . . . .	34
2.4	Short excursion: Detection of magnetic fields . . . . .	38
<b>3</b>	<b>Smoothed Particle Hydrodynamics</b>	<b>45</b>
3.1	Lagrangian derivation of SPH equations . . . . .	45
3.2	Interpolation formulas . . . . .	51
3.3	Different kernels and their characteristics . . . . .	54
3.4	MHD equations in SPH . . . . .	60
<b>4</b>	<b>Thermal conduction in GADGET</b>	<b>63</b>
4.1	Isotropic implementation . . . . .	63
4.2	Anisotropic implementation . . . . .	67
4.2.1	An easy idea . . . . .	67
4.2.2	The split up approach . . . . .	68
4.2.3	A fully consistent numerical scheme . . . . .	73
4.2.4	Summary and expectations for the different schemes . . . . .	80
4.3	Tests for the code . . . . .	83
4.3.1	Temperature step problem . . . . .	83
4.3.2	Sinusoidal temperature variation . . . . .	105
4.3.3	Hot gas sphere . . . . .	117
4.4	Summing up the test results . . . . .	123
<b>5</b>	<b>Application to Galaxy Clusters</b>	<b>125</b>
5.1	Sample clusters from the Dianoga set . . . . .	125
5.2	Comparison runs with different settings . . . . .	128

5.2.1	Analysing a non-conductive run . . . . .	128
5.2.2	Changes due to different conduction implementations . . . . .	138
5.2.3	Adding radiative cooling, star formation and supernova feed- back . . . . .	143
5.3	Comparison to existing simulations with grid codes . . . . .	149
<b>6</b>	<b>Conclusion and Outlook</b>	<b>151</b>
<b>7</b>	<b>List of figures</b>	<b>I</b>
<b>8</b>	<b>Sources</b>	<b>III</b>
<b>Appendix A</b>	<b>The Conjugate Gradient Method</b>	<b>A1</b>
<b>Appendix B</b>	<b>The second order error term</b>	<b>B1</b>
<b>Appendix C</b>	<b>Complex integration</b>	<b>C1</b>
	<b>Acknowledgement</b>	

# 1 Galaxy Clusters and cooling flows

Galaxy clusters are the largest gravitationally bound objects which have formed in the observable universe so far. They consist usually out of 50 or more member galaxies. The typical mass of an entire cluster is bigger than  $3 \cdot 10^{14} M_{\odot}$ . This mass is however not dominated by the optically visible stars in the galaxies but by dark matter and (in comparison to stars) the hot gas between the galaxies. As a rule of thumb a typical cluster consists out of 84% dark matter, 13% hot gas and only 3% stars. The free gas is called **Intra Cluster Medium** and has a typical temperature of  $3 \cdot 10^7 K$ . This corresponds to a wavelength of about  $5 \cdot 10^{-11} m$ . Therefore emissions by this hot gas component can be typically observed in the X-ray. It is very important to fully understand these processes in order to infer for example the total mass of galaxy clusters. Details on the radiation processes will follow in the next section where we discuss the physics of the ICM in general. [[Schneider, 2008](#), [Peterson and Fabian, 2006](#)]

We will also present problems which arise through comparison of models and observations concerning cooling flows and show some existing ideas to solve those problems and discuss their success. We will then focus onto thermal conduction in a fully ionized plasma and present a numerical implementation and simulation results using that code.

## 1.1 Physics of the ICM

For a general overview of the ICM we follow the review papers of [Fabian, 1994], [Peterson and Fabian, 2006] and [Sarazin, 2008].

As already mentioned the hot intra cluster gas has temperatures of about  $10^7 K$ . Some temperature profiles from measurements are shown in figure 1.

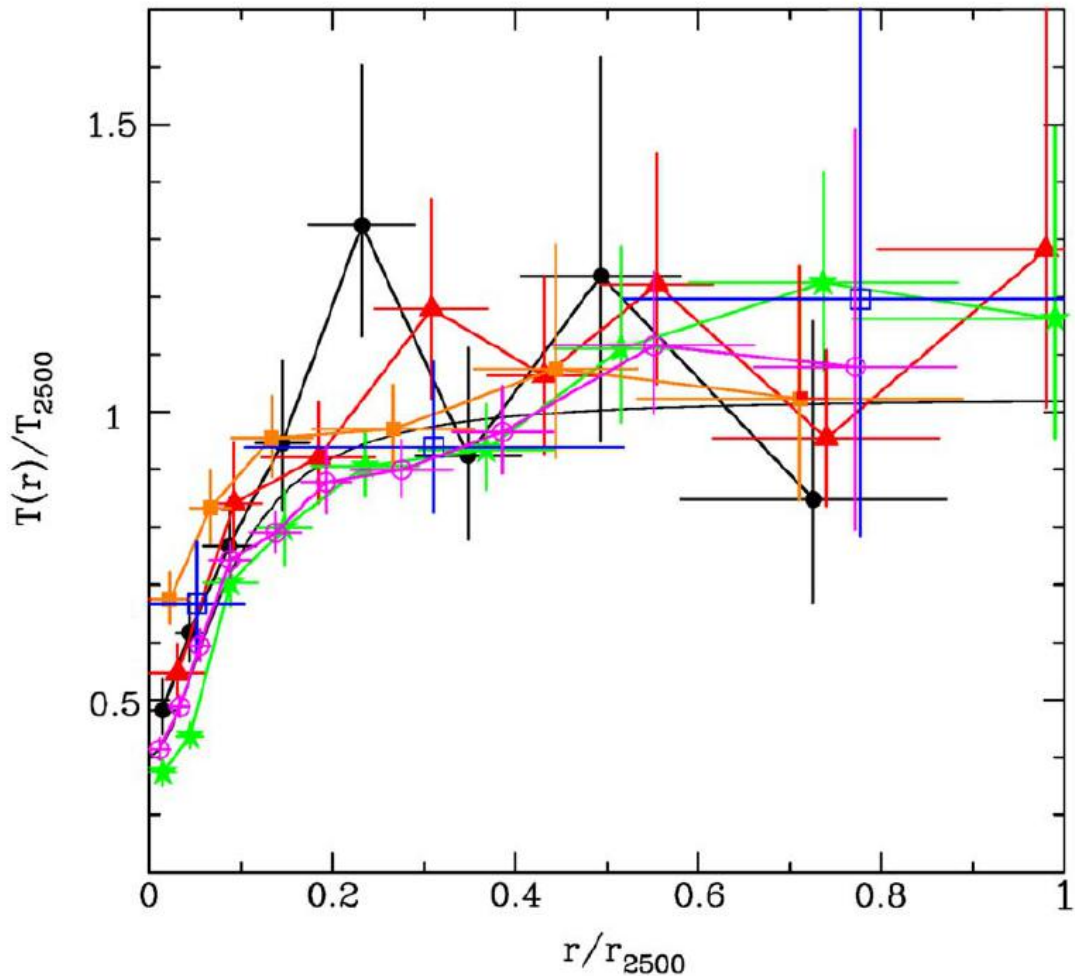


Figure 1: Temperature plotted against the distance to the cluster center for several galaxy clusters using Chandra data. Both axes are scaled to their values at  $r_{2500}$ . (The radius where the density is equal to 2500 times the critical density.) One can see, that the temperature decreases strongly when going into the cluster core. [Peterson and Fabian, 2006]

Obviously the temperature declines strongly in the inner parts of the cluster. The plasma seems to be more or less isothermal in the outer parts. The X-ray emitting ICM is usually contained in a radius of about  $2Mpc$ . Therefore it's origin can not be a single galaxy but has to be an extended region with a considerable gas component.<sup>1</sup>

The origin of the gas is still uncertain. It cannot be pure primordial since it is highly metal enriched. So at least some of the gas must have undergone the process of star formation and supernova explosions. Another possibility for metal enrichment of the ICM is the stripping of gas from young galaxies during the formation of the cluster. In both cases the gas receives it's kinetic energy from the member galaxies. Therefore we can conclude, that the sound speed of the gas will be similar to the galaxy velocities of several  $1000 km/s$  at  $10^8 K$ . It is likely that most of the gas in the ICM was shock heated this way and not only accelerated gravitationally. This leads to the high temperatures the ICM should have, inferred by X-ray observations.

Having a look at typical densities inside the ICM, one can distinguish between so called *peaked* and *non-peaked* clusters which have gas densities of roughly  $10^{-1} cm^{-3}$  and accordingly  $10^{-3} cm^{-3}$ . For comparison, the mean cosmic density of baryons is only about  $10^{-8} cm^{-3}$  ([Peterson and Fabian, 2006]). So the inter cluster medium is dense enough to be really visible but it is still optically thin, meaning that the mean free path inside is pretty large. This property is very important for observations, since emitted light won't be reabsorbed to a large fraction and can therefore be observed very well. This allows us to extensively study the properties of the ICM in an unperturbed state.

One can calculate the typical time which is needed to bring the gas into kinetic equilibrium (for general particles of type 1 in a field of particles of type 2) via collisions as

$$t_{eq}(1, 2) = \frac{3m_1 \cdot \sqrt{2\pi} (k_B T)^{3/2}}{8\pi \cdot \sqrt{m_2} n_2 Z_1^2 Z_2^2 e^4 \cdot \ln \Lambda} \quad (1.1.1)$$

with the so called Coulomb logarithm which is defined by the minimum and maximum collision parameters:

$$\ln \Lambda = \ln \frac{b_{max}}{b_{min}} \quad (1.1.2)$$

---

<sup>1</sup>The typical size of an elliptical galaxy is only of the order of  $1 - 100 kpc$ . [ast, 2013]

For electron-electron collisions this is equal to

$$\begin{aligned} \ln \Lambda &= 23.5 - \ln \left( n_e^{-1/2} T_e^{-5/4} \right) - \left( \frac{10^{-5} + (\ln T_e - 2)^2}{16} \right)^{-1/2} \\ &\approx 37.8 + \ln \left[ \left( \frac{T_e}{10^8 \text{ K}} \right) \left( \frac{n_e}{10^{-3} \text{ cm}^{-3}} \right)^{-1/2} \right] \end{aligned} \quad (1.1.3)$$

The weak logarithmic dependence on the temperature and the density is often neglected for calculations regarding the ICM. Usually one uses just the constant value  $\ln \Lambda \approx 37.8$ . [Sarazin, 1986],[Jubelgas et al., 2004],[Huba, 2011]

After that this equilibration time all particles will have velocities according to a Maxwellian distribution for their respective temperature. Calculating this time for electrons and protons with typical cluster conditions one gets values which are about one magnitude lower than typical cluster ages. Therefore electrons and ions are supposed to have almost the same temperature.

Regarding the mean free path we want to mention, that it is however still small enough for the ICM to be treated as a fluid. [Spitzer, 1956] gives a formula to calculate the typical mean free path of electrons as:

$$\lambda_e = \frac{3^{3/2} (k_B T_e)^2}{4\pi^{1/2} n_e e^4 \ln \Lambda} \approx 22.5 \left( \frac{T_e}{10^8 \text{ K}} \right)^2 \left( \frac{n_e}{10^{-3} \text{ cm}^{-3}} \right)^{-1} \text{ kpc} \quad (1.1.4)$$

The outcome is much lower than the typical size of a galaxy cluster, however it is small enough to allow a pure hydrodynamic formulation in all parts of the cluster. But this formula does not take the influence of magnetic fields into account, which then decrease the mean free path drastically. Further calculations regarding the collision time in a plasma are presented in details in section 2.2.

We can use combined techniques of imaging and spectroscopy to infer properties of the ICM like temperature and density and also the origin of the radiation itself. To understand the origin of the radiation, we need to point out that galaxy clusters typically contain not negligible magnetic fields of the order of  $\mu G$ . [Taylor et al., 2006]

Therefore the ICM can be assumed as a fully ionized plasma. For this temperature the emitted radiation is in the X-ray band and typically consists mainly of

continuous free-free emission (also called bremsstrahlung). Additional components are continuous bound-free emission (recombination) and two-photon decays of 2s levels in helium like ions. These processes can be best identified by comparing characteristics shown in the spectra. We know for example that bremsstrahlung has a more or less flat spectrum with an upper exponential cutoff. The cutoff frequency is defined through the highest energy an emitted photon can get from the electron, i.e. the average thermal energy of electrons. For details see for example [Flynn, 2006].

Bremsstrahlung is radiation due to acceleration of electrons in the Coulomb field of the ions. Dependent on the velocity of the electrons (or rather their temperature) the emitting wavelength is different. Since the electron velocities are distributed continuously (typically following a Maxwell-Boltzmann distribution) we also get a continuous spectrum.

In contrast to that, line emission happens at discrete wavelengths which are however broadened by various effects like the Doppler effect. The strongest lines belong to the Fe  $K\alpha$  complex at about 6.7 keV. For low energies even more lines from lighter elements become crucial.

Which one of these two processes dominates radiation is also temperature dependent:

The emissivity due to free-free radiation scales mainly like  $\propto T^{-1/2} \cdot \exp\left(-\frac{h\nu}{k_B T}\right)$ . It is the dominant effect for gas above roughly  $2 \cdot 10^4 K$ . We will show actual spectra when we discuss the **Perseus** cluster in section 1.2. By analysing the spectral information about the received light one can verify the mentioned components as origin of the radiation.

An important consequence of the emission of X-ray radiation is strong cooling of the gas. Reducing the thermal pressure which stabilizes the gas against gravity, it will start to fall into the cluster core. However this infall reheats the gas again which works stabilizing and slows down the whole process. Therefore the infall will stay subsonic. The key temperature at which these processes equilibrate is the *virial temperature*.<sup>2</sup> This process is what we call a *cooling flow*. As an example, [Fabian et al., 1981] have calculated mass inflow of several hundred solar masses per year for **NGC1275** in the **Perseus** cluster.

---

<sup>2</sup>We will further discuss the virial temperature in section 5.2.1

For our analysis we define some typically used quantities: the so called *cooling time* and *cooling radius*. The time it takes for an optically thin plasma to cool, can be defined as the gas enthalpy over the energy loss per unit volume. Therefore we get

$$t_{cool} = \frac{\frac{5}{2}n_e k_B T}{n_e^2 \Lambda} \approx t_U \cdot \frac{T}{10^8 K} \left( \frac{n_e}{10^{-2} cm^{-3}} \cdot \frac{\Lambda}{10^{-23} erg cm^3 s^{-1}} \right)^{-1} \quad (1.1.5)$$

with

- $\mathbf{n_e}$ : the electron number density
- $\mathbf{\Lambda}$ : the cooling function
- $\mathbf{t_U} \approx 13.82 Gyr$ : the age of the universe<sup>3</sup>

The gas enthalpy is used instead of the thermal energy, because the gas is compressed while it cools and therefore the heat capacity rises accordingly.

The equation shows, that for typical values the cooling time is similar to the age of the universe and therefore approximately the age of galaxy clusters. Therefore cooling plays an important role and cooling flows can in principle occur.

About two third of low and moderate redshift clusters have cooling times less than 10 *Gyr*, for one third it is even less than 3 *Gyr*.

For this calculation we needed the cooling function, which is usually used in a tabulated form. It follows an equation of the form

$$\Lambda(T, Z_i) = \int_0^{\infty} dE E \frac{d\alpha}{dE}(E, T, Z_i) \quad (1.1.6)$$

with  $d\alpha/dE$  being the energy dependent line/continuum power. Typical X-Ray luminosities are in the range of  $L_X \sim 10^{43} - 10^{45} \frac{erg}{s}$  depending on the clusters mass. Typical results for different abundances in clusters are shown in figure 2.

---

<sup>3</sup>For latest measurements of cosmological parameters see [Aghanim et al., 2013].

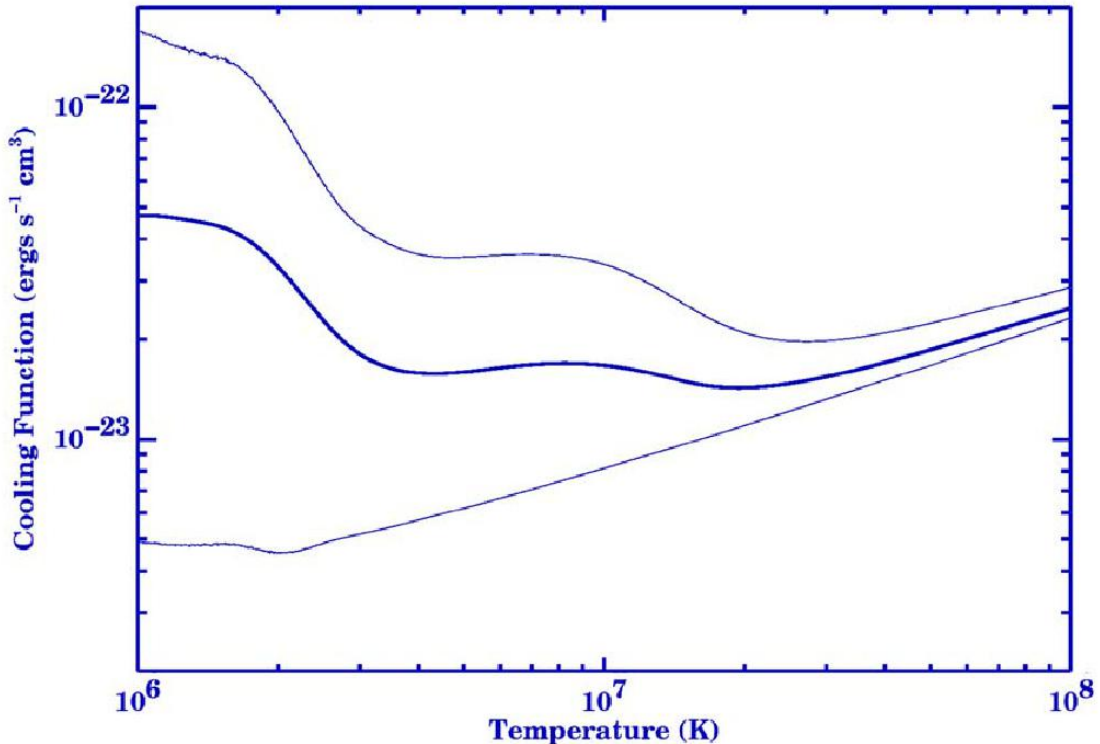


Figure 2: Different cooling times dependent on the temperature for three abundances. From top to bottom: solar abundances, one third of solar abundances and pure hydrogen and helium. Plotted is the temperature region in which free-free radiation and line emission operate. The curves are basically the solution of equation 1.1.6. We see that typical values lie between  $5 \cdot 10^{-24}$  and  $2 \cdot 10^{-22} \frac{erg\ cm^3}{s}$ . [Peterson and Fabian, 2006]

The cooling time exceeds however the gravitational free-fall time. Therefore we can approximate the gas as in hydrostatic equilibrium.

For completeness, the cooling time only due to free-free radiation can be calculated as

$$t_{cool\ f-f} \approx 69 n_{-3}^{-1} T_8^{1/2} Gyr \quad (1.1.7)$$

It is important to state, that the cooling accelerates as the gas cools, since the increase due to rising density through gravitational infall is stronger than the decrease due to the temperature dependence. For line emission this effect is even bigger due a different temperature dependence. This is often called the *cooling catastrophe*.

The cooling radius is then simply defined as the radius, where the cooling time equals the age of the galaxy cluster. In figure 3 one can see the cooling time plotted against the distance from the cluster's center for several galaxy clusters. The horizontal line marks the typical cluster age, so we can read of typical cooling radii as 100 – 200 *kpc*.

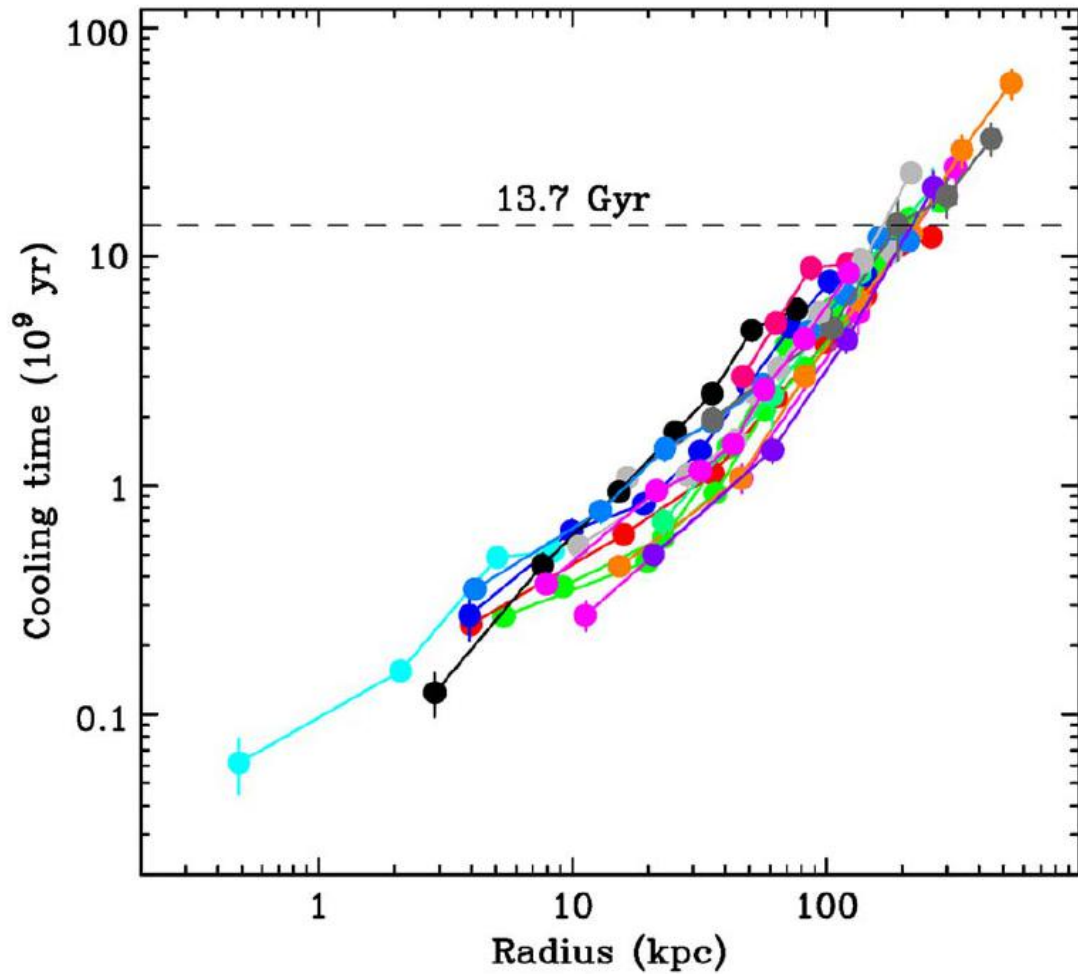


Figure 3: Different cooling times plotted against the distance from the cluster center for several galaxy clusters using Chandra data. The horizontal line marks approximately the age of the universe (new measurements suggest a value of 13.82 *Gyr* [Aghanim et al., 2013]) Without any disturbance all plasma within 100 – 200 *kpc* would have enough time to cool.[Peterson and Fabian, 2006]

Within  $r_{cool}$  we can assume the gas to lose energy due to cooling. To support the pressure, it has to contract further. Assuming we have no matter sources within this region, the result is a cooling flow. Since we find the necessary conditions for cooling flows in most of the cluster observations we can assume the cooling flows to be long-lived and fairly stable.

We can further define the total luminosity of the cooling gas, i.e. inside the cooling radius. This luminosity measurement can be used to determine the mass deposition rate (or accretion rate) due to the cooling flow. Assuming that only radiation of thermal energy and the energy gained by contraction is crucial, we can write the luminosity of the cooling gas as

$$L_{cool} = \frac{5 \dot{M}}{2 \mu} k_B T \quad (1.1.8)$$

with the reduced mass of the gas particles  $\mu$ . Plugging in typical luminosities we get values of  $\dot{M} = 50 - 100 \cdot M_{\odot} \text{ yr}^{-1}$ .<sup>4</sup> For some clusters like Hydra A even bigger mass deposition rates are found. By measuring a whole set of galaxy clusters one can find an empiric relation between the accretion rate and the age of a cluster of

$$\dot{M} \propto t_a^{1/3} \quad (1.1.9)$$

Therefore the error of the cluster age estimate does not influence the results too much.

So far we have assumed a spherical symmetric and homogeneous setup. Without going into detail, we can define the cooling flow equations for this kind of setup in a steady state model as

$$\dot{M} = 4\pi r^2 \rho v \quad (1.1.10)$$

$$\rho \frac{d\Phi}{dr} = \frac{d(\rho T)}{dr} \quad (1.1.11)$$

$$\rho v \frac{d}{dr} \left( \frac{5}{2} T - \Phi \right) = -n_e n_H \Lambda + \text{interactions} \quad (1.1.12)$$

$$\frac{1}{r^2} \frac{d}{dr} \left( r^2 \frac{d\Phi}{dr} \right) = 4\pi G (\rho + \rho_{DM}) \quad (1.1.13)$$

---

<sup>4</sup>See for example [Fabian et al., 1981] for measurements.

However X-ray observations show, that inhomogeneities and mixtures of density and temperature exist. Usually the cluster cores are especially well resolved and observers find that the accretion rate scales only linear with  $r$ . For the homogeneous model we would expect flatter X-ray surface brightness profiles. A so called multiphase gas model can take this into account. For details about multiphase models see for example [Fabian et al., 2006].

Still homogeneous models lead in general to fairly good results and are usually the only feasible method due to complexity and the lack of detailed information.

Also non steady state models have been considered so far, but without the expected success. See for example [Meiksin, 1990] for details.

Moreover there is another inconsistent aspect in the X-ray observations involving the soft X-ray spectrum which does not totally match a simple cooling flow model. This issue can be solved by assuming intrinsic absorption in the flow. [Fabian et al., 2003]

## 1.2 The Perseus cluster in different wavebands



Figure 4: Picture of the **Perseus** cluster (**Abell 426**) in the optical band. The bright blobs here are the galaxies of the cluster. The dominant galaxy is **NGC 1275** on the left in the image. A more detailed image of the galaxy is shown in figure 5. [Source: Apod <http://apod.nasa.gov/apod/ap110712.html>]

After that overview we want to discuss the details of what can be found in the different wavebands and not only the X-ray and the implications on cooling flow models. A detailed discussion can be found in [Fabian, 1994] and [Fabian et al., 2003].

In figure 4 you can see an optical image of one of the closest galaxy clusters we know: the **Perseus** Cluster. In the optical band we see the light emitted by stars in the member galaxies of the cluster, which is also known as **Abell 426**. The Abell catalogue is a collection of galactic over-densities which was published in 1958 for the first time. The **Perseus** cluster has a redshift of  $z = 0.0183$  and its central galaxy is called **NGC 1275** (left part of the image or in detail figure 5).

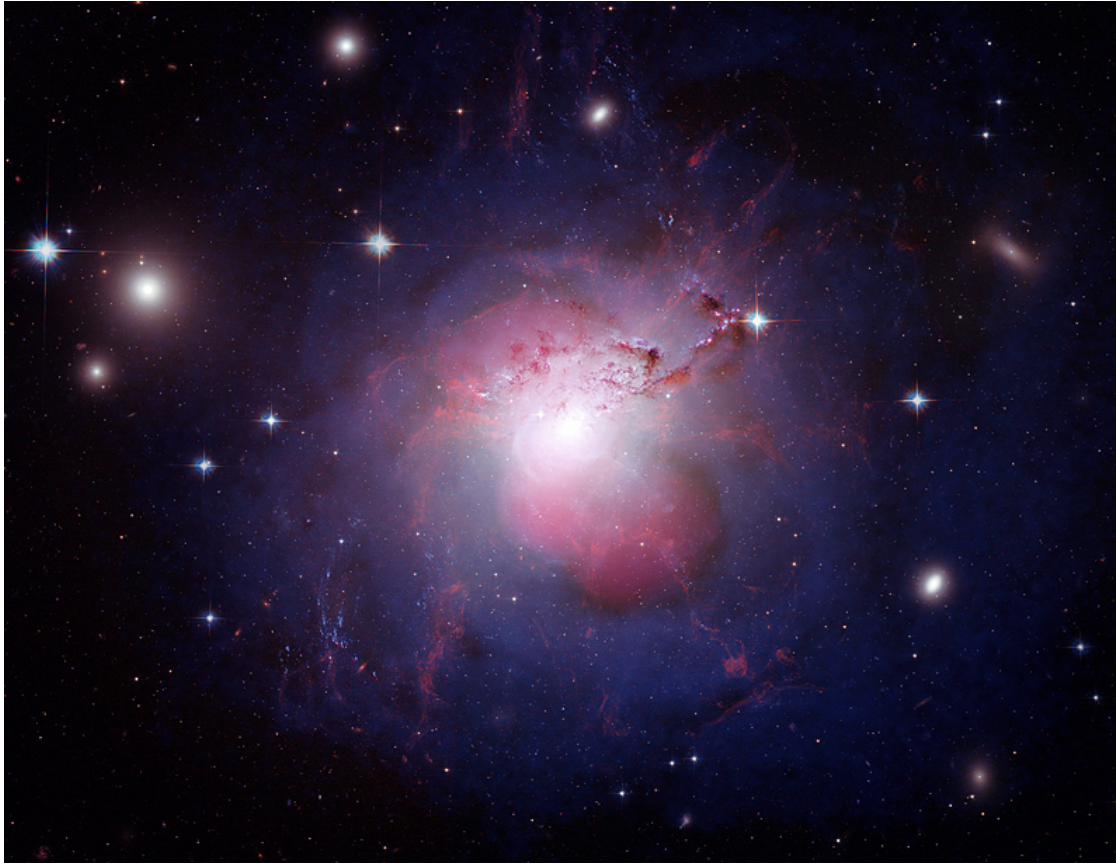


Figure 5: Composite image of several observations of **NGC 1275 (Perseus A)** combining optical observations (HST), X-ray (Chandra ACIS) and radio data (VLA). The cooling gas is represented by the violet shells around the center, while the radio lobes are shown in pink. [Source: Chandra <http://chandra.harvard.edu/photo/2008/perseus/>]

High resolution X-ray observations of the hot gas (done by [Fabian et al., 2003]) can be seen in figure 6.

Since X-ray observations have been our focus all along, let us start to give some details on **Perseus** properties in this waveband. Interestingly it's cooling flow does not peak in the center of the cluster but about  $20\text{ kpc}$  off. This is probably due to the two radio lobes which can be found in the cluster which seem to be holding off the cooling flow. More details on the radio lobes will follow when we come to that waveband.

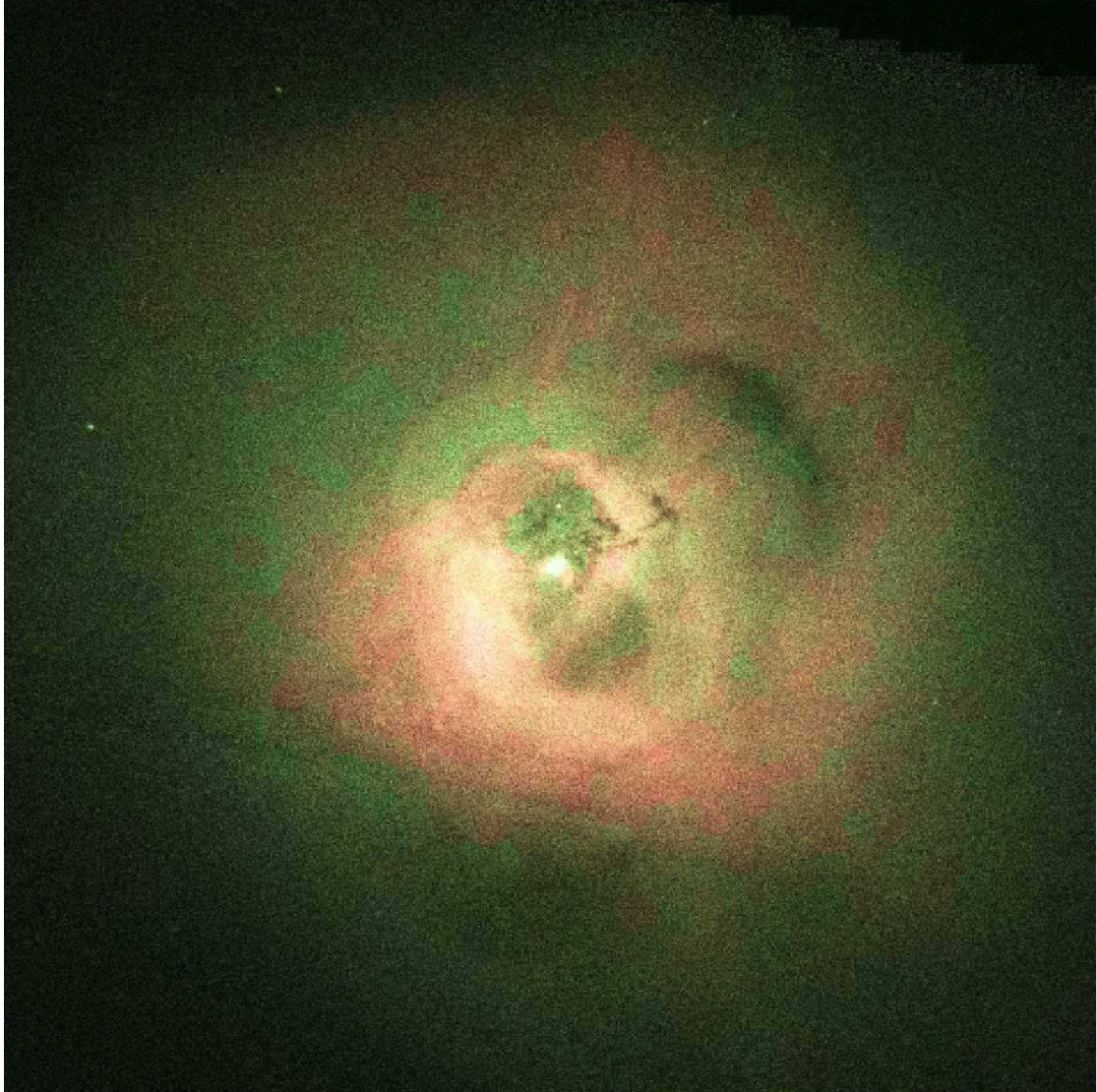


Figure 6: Central regions of the **Perseus** cluster (Abell 426) in the X-ray band emitted by cooling gas taken from Chandra data. Intensity between  $0.3\text{ keV}$  and  $7\text{ keV}$  colour coded by temperature. The X-ray emission is sharply peaked around the center of the cluster. The two darker regions are radio bubbles surrounded by hard X-ray radiation, which have been blown out by jets from the radio source **3C 84**. The picture is of size 131 kpc squared. [Fabian et al., 2003]

Measurements of the Fe XVII line lead to a cooling time less than  $3 \cdot 10^7 \text{yr}$ .<sup>5</sup> These measurements agree with those of the hotter gas. Spectral information about the inner core of the **Perseus** cluster (and therefore mainly of **NGC 1275**) is shown in figure 7. Note, that the Fe XVII line emission lies in the left corner of the plot and is therefore totally different than the main part of the emission in higher energy channels. The theoretical line spectrum is shown in figure 8.

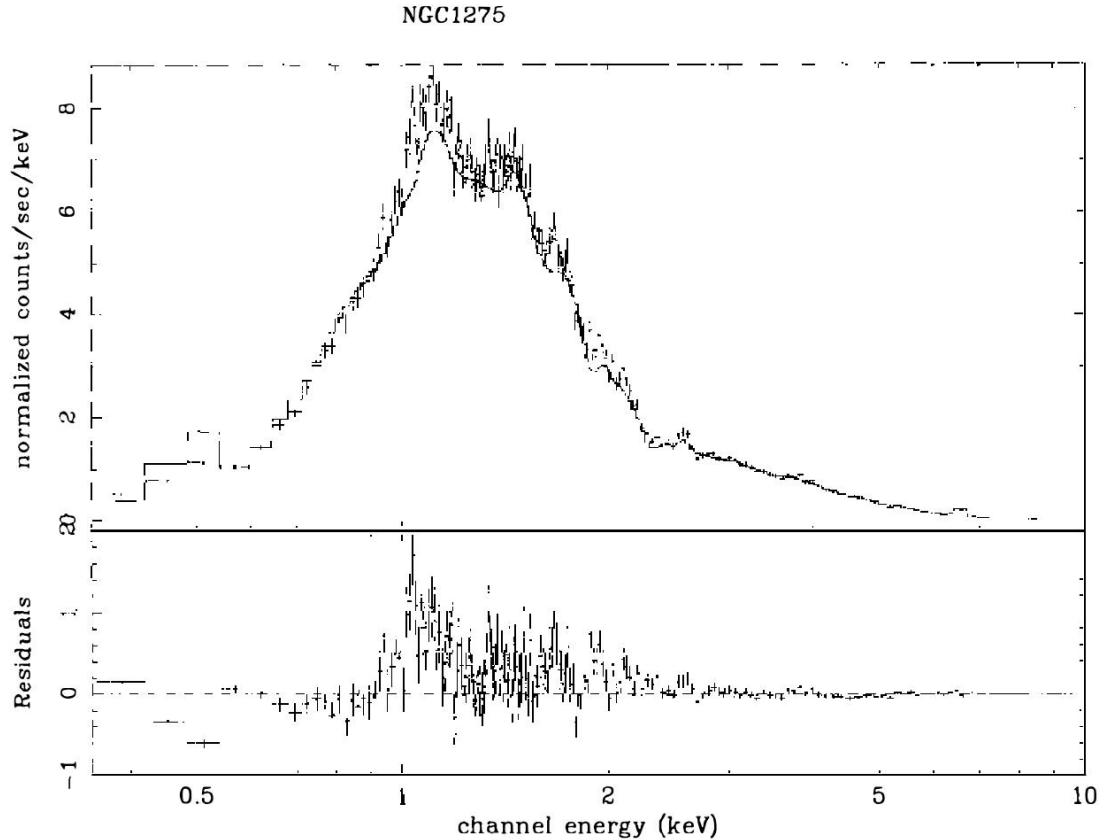


Figure 7: Spectral information of the inner core of the **Perseus** cluster. Shown is the spectrum in the upper panel and the residuals in the lower panel. Positive residuals indicate a more soft emission while negative ones show that excess absorption is required. The spectrum can be well fitted by a cooling flow spectrum plus isothermal hot emission. Details about the line emission can be found in figure 8. [Fabian, 1994]

<sup>5</sup>The Fe XVII line is measured for gas with temperature lower than  $5 \cdot 10^6 \text{K}$

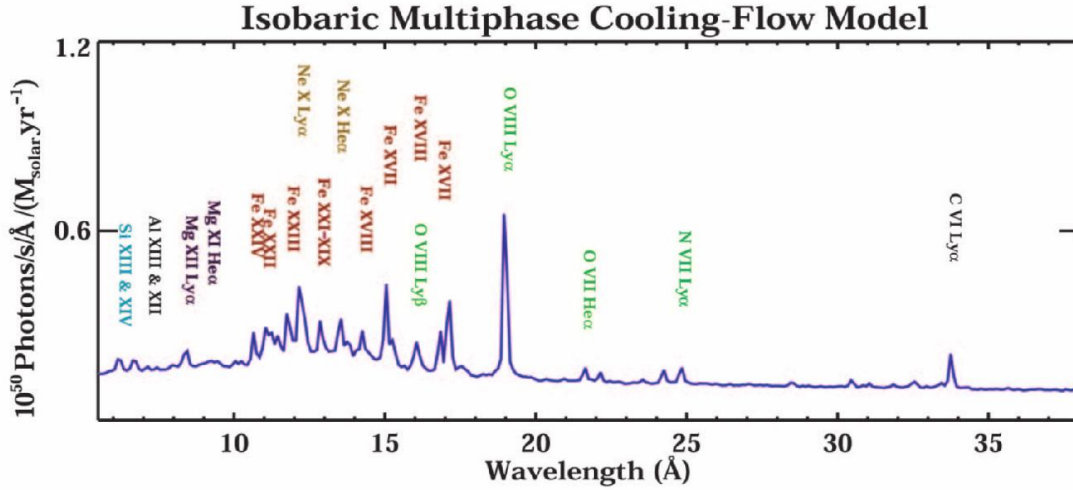


Figure 8: Typical emission lines which overlay the thermal Bremsstrahlung spectrum. The most prominent lines belong to iron and oxygen. The spectrum is produced using a isobaric cooling flow model with a maximum temperature of 6 keV. [Peterson et al., 2003]

In total the X-ray evidence from imaging and spectra combined indicates strongly the existence a steady long-lived cooling flow. The question is now if this prediction can be proven or falsified by observations in other wavelengths.

In one short sentence: there is only little evidence for cooling flows in the optical band. Central regions of cooling flow clusters often show optical line nebulosity in regions up to 10 kpc with luminosities above  $10^{43} \text{ erg s}^{-1}$  in  $H\alpha$ . In **NGC 1275** the total UV and optical luminosity is even over  $3 \cdot 10^{43} \text{ erg s}^{-1}$ . However most observed nebulae are about one or two orders of magnitude less luminous and some cooling flow clusters do not show this kind of line emission at all. These nebulae are probably powered by the energy of the hot gas or it's turbulence.

Additionally one can usually see a blue optical continuum emission extended over several kpc. Earlier we estimated the mass deposition rates of typical cooling flows. Without any disturbance the gas should cool until it can not emit in the X-ray any longer and contract while that. These over-dense regions of cold gas should be a massive source of star formation in the cluster core. This kind of increased star formation rate should then be visible in the optical continuum data, where we find however only little evidence. The central galaxies should be much brighter in

blue colour than they are observed if the whole cold gas would form stars with a normal initial mass function (IMF). We would expect about a factor of 10 more star formation than has been observed. Therefore the cold gas (if it exists) remains in it's state for some reason or forms some kind of non visible objects. This is very often called the *cooling flow problem* because it indicates something in the model is missing. Attempts to solve this mystery will be discussed in section 1.3.

Before we come to the radio emission we want to mention briefly, that there have been observations in the infrared which could correspond to cooling flows. However this seems not to be totally clear until today. For a discussion please see [Fabian, 1994] and references therein.

As we have already stated earlier, in the **Perseus** cluster sits the radio source **3C 84** which is most like responsible for the displacement of the high X-ray region from the cluster center. Figure 9 shows radio observations overlaid on a smoothed X-ray map, where this effect can be seen very well. The puzzling aspect about these radio lobes is, that despite the assumed heating effect the coolest gas is seen close to them (see again figure 6).

Strong central radio sources like **3C 84** seem to be very common in cooling flow clusters. Other examples are **Cygnus A**, **Hydra A** or **Virgo A**. They are produced by the relativistic outflow of an active galactic nucleus (AGN) surrounded by a dense medium which is provided by the cooling flow. However not every cooling flow cluster hosts a powerful radio source like this. An example would be **Abell 478**. [Fabian, 1994]

**NGC 1275** has additionally an outer radio halo which is mainly due to acceleration of electrons in the presence of a magnetic field. Therefore we can study the magnetic field strength and structure in clusters through detailed radio observations. Typical magnetic field strengths are between  $0.1 - 10 \mu G$ . By compression of gas through the cooling flow the magnetic field can however even exceed these values. Observing the detailed structure is very complicated, since small scale changes can not be resolved very well. Over the whole range of cluster gas one could talk about chaotic magnetic fields, where entangling and also reconnection play an important role.

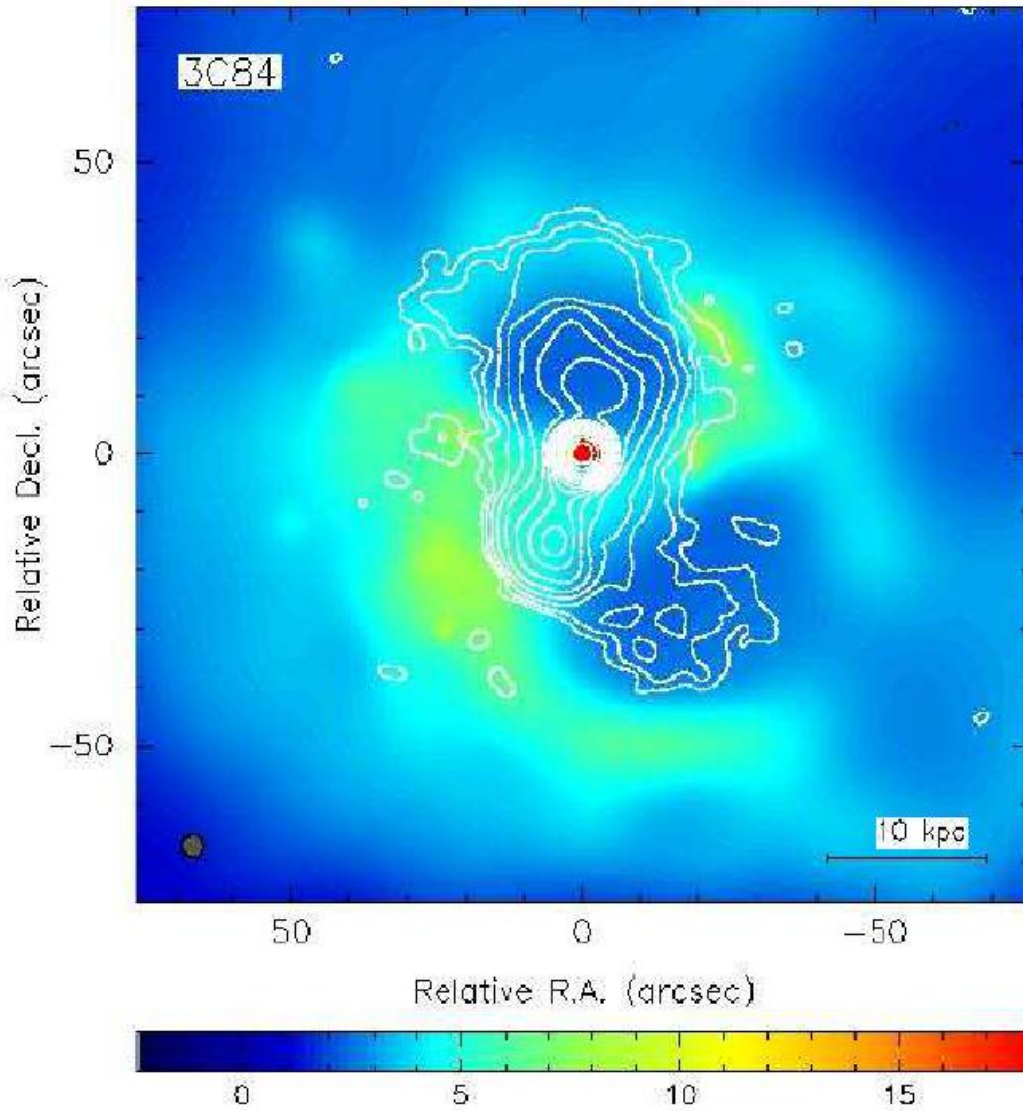


Figure 9: 1.4 GHz radio image of the **Perseus** cluster combined with a smoothed X-ray map (0.5–7 keV). The two radio lobes coincide very well with displacement of the high X-ray regions. [Fabian, 2002]

Typical length scales for field reversal are found to be  $1 - 10 \text{ kpc}$ .

Summing up the findings from the different wavebands we clearly see, that cooling is happening in the galaxy clusters, one identifies as cooling flow clusters purely from X-ray informations. Observations confirm, that the gas has a high density, a high pressure and a short cooling time. No general occurring anomalies are found so far. But for example optical observations only show no direct indications of cooling flows but in the most inner parts of clusters (several  $\text{kpc}$ ). It is very difficult to prove the (non-) existence of cooling flows using data from other wavebands than X-ray. [Fabian, 1994]

As already stated, some implications of the model do not match the observations: The amount of cold gas ( $T < 1 \text{ keV}$ ) we would expect to find due to the large mass accretion rates we estimated is not observed so far. Additionally it is not clear, why we cannot see the gas cooling any further. The radiation could be absorbed or the cooling could not be radiative any more but due to mixing. Nevertheless one question still remains: What happens to the expected cold gas? This is the main question which we want to tackle in the next section.

### 1.3 Possible solutions of the cooling flow problem

Throughout the years there have been many attempts to solve the problem of the not detected cold gas. We want to show different attempts<sup>6</sup> and discuss the success so far before we focus on thermal conduction for the rest of this thesis.

We can distinguish two main categories of ideas to solve the problem:

1. The gas evolves to a non visible state, or at least one which could not be observed so far.
2. A mechanism has to be taken into account, which balances the cooling flow and prevents the gas to cool beyond the boundary of  $1 - 2 \text{ keV}$ . This would most likely be some kind of heating process, but there are also some different approaches to this.

Since the first category is highly speculative, we will discuss only on ideas of the latter type in this thesis. For further reading we just want to mention, that cold molecular gas ( $T \approx 3 \text{ K}$ ) like fractal hydrogen could be a candidate for an invisible final state. The properties of this gas are thoroughly discussed in [Pfenniger and Combes, 1994] while [Salomé and Combes, 2003] show that cold molecular gas can indeed be detected in cooling flow clusters.

For all the possible ideas concerning the second type of solution we can establish one constraint: the timescale on which the process happens has to be comparable to the cooling time. If the timescale of the process is too short it will probably overwhelm the cooling flow. If it's too long, it is dynamically not really important won't solve the problem. [Peterson et al., 2003]

One general problem with heating mechanisms is, that most heating mechanisms are proportional to volume whereas the cooling rate is proportional to the density. This tends to make the gas unstable: Some regions will carry on cooling while others heat up. [Peterson and Fabian, 2006]

Furthermore the mechanism we look for, would have to stop the temperature change of gas at a temperature of  $1 - 3 \text{ keV}$ . It needs to work against cooling over the full range of temperatures, and thus radii, to be effective. Therefore a lot of energy is needed. Estimations show, that this would not be a problem for

---

<sup>6</sup>Without claim of completeness.

smaller clusters like **Virgo**, however the big ones like **Abell 1835** would need an enormous amount of energy ( $\sim 10^{46}$  *erg/s*). [Fabian, 2002]

So let us at first discuss one idea which is not related to heating processes at all. In the last section we stated, that with a normal IMF we would expect a factor 10 more star formation through the predicted amounts of cold gas, than is been observed. Therefore a first approach could be, to state, that for some reasons stars are simply not formed according to a normal IMF. Nearly all cooled stars would have to form stars less massive than  $0.6 M_{\odot}$ . Since even "normal" star formation is still not totally understood in all details, we do not want to go into more detail about that approach. It is still highly speculative! Further discussions can for example been found in [Bregman and David, 1989] and references therein.

Earlier we mentioned the typical velocities of cluster's member galaxies (see section 1.1). Another idea stated in [Bregman and David, 1989] is, that the drag heating of galaxies could reheat the cooling gas strong enough to serve our purpose. A reheating in general reduces the net cooling of the gas and therefore decreases  $\dot{M}$ . With a significantly lower mass deposition rate we could again get a match up with observed star formation rate of high mass stars.

For drag heating to have any effect we need highly supersonic galaxy motion (Mach number  $M \gg 1$ ). Since the ICM outside the cooling radius should still have a sound speed similar to the galaxy motion, there would hardly be any heat transfer in the outer regions of a cluster. This is a very good property, since the model then only tackles the regions, where we want to change our description due to inconsistencies without an effect on the surrounding material. The heating rate through supersonic galaxies can be roughly described through

$$H = \underbrace{n_{gal} v_{gal} \sigma}_{galaxy} \cdot \overbrace{n_{gas}}^{gas} \cdot \underbrace{k_B \Delta T}_{energy} \quad (1.3.1)$$

with the gas and the galaxy density  $n$ , the velocity of the galaxy  $v$ , the cross section of the galaxy  $\sigma$  and the temperature increase  $\Delta T$  which is given by the

Rankine-Hugoniot jump condition

$$\frac{\Delta T}{T} = \frac{(5M^2 + 3) \cdot (M^2 - 1)}{16M^2} \quad (1.3.2)$$

This formulation is consistent with the fact, that  $H$  should be very small for  $M \ll 1$ .

Simulations including this kind of model have been performed, however with moderate success. The results seem to vary strongly dependent on the value of the galactic heating parameter  $\Phi = n_{gal}v_{gal}\sigma$ . Unfortunately the mass deposition rate has not been decreased much for most of the typical values of  $\Phi$ , which basically rules out the idea (or at least the presented model for the idea).

Another more straight forward approach for a heating source, which has not been considered in the standard cooling flow model are supernova explosions. So far we just let the cooling gas form stars. But an increased star formation rate will also lead to an increased rate of supernova explosions, which reheat the surrounding medium. Therefore if the heating by supernovae is strong enough this could balance the cooling and therefore the star formation. Considerations regarding the following description are again taken from [Bregman and David, 1989].

At first we have to distinguish between the different supernova types:

- Type Ia
- Type Ib and II, which cover about 2/3 of all supernovae in normal star forming regions

The latter type of supernovae are commonly associated with the explosions of massive stars. Since these massive stars are nowadays very rare observed in galaxy clusters, we can assume these supernovae to occur mainly during the time of star and galaxy formation. Type Ia supernovae however are the product of binary star systems and therefore their feedback can be seen as a more continuous sort of heating.[Sarazin, 2008]

By balancing the energy difference of the cold gas and the cooling ICM with the energy released by supernovae one can estimate the fraction of cold gas  $f$  which is reheated as

$$\frac{1}{f} = 1.2 \cdot \frac{1 \text{ SN}/100 M_{\odot}}{v} \frac{10^{51} \text{ erg}}{E_{SN}} \frac{T_{eff}}{3 \cdot 10^7 K} + 1 \quad (1.3.3)$$

A reduction of  $\dot{M}$  by one order of magnitude would correspond to  $f = 0.9$  and requires due to this relation one supernovae per  $9 M_{\odot}$  of star forming gas. Since known values for typical supernova rates are more like one per  $100 - 300 M_{\odot}$ , the reduction of  $\dot{M}$  due to supernovae heating according to this model is minimal. Furthermore one can derive the required supernova rate as at least

$$SN \text{ rate} = 1.1 \cdot \frac{\dot{M}}{100 M_{\odot} \text{ yr}} \frac{T}{3 \cdot 10^7 \text{ K}} \frac{SN}{\text{yr}} \quad (1.3.4)$$

which leads for example in the **Perseus** cluster for  $f = 0.9$  to a value of  $300 - 600 SN/yr$ . However observations do not show supernovae rates nearly as high. Only for elliptical galaxies, where the temperatures are significantly lower, supernovae heating can play a role but not for galaxy clusters.

The next idea we want to discuss was proposed by [Soker et al., 2001]. They state, that a cooling flow is disturbed and partially disrupted by a powerful radio jet on a timescale of several  $10^9 \text{ yr}$ . This jet can either be produced by the outburst of active galactic nuclei (AGN) of inner **cD** galaxies<sup>7</sup> triggered by accretion of cooled gas or a cluster submerger- The jet is assumed to output an energy of  $10^{47} \text{ erg/s}$  over a time of  $10^7 \text{ yr}$ . Since most of the observed cooling flow clusters contain strong radio activity in the inner regions these assumptions could be reasonable. An example for a cluster with ongoing merger event is the Centaurus cluster.

The jet will propagate through the ICM with velocities of several  $10^3 - 10^4 \text{ km/s}$ . [Soker et al., 2001] claim, that the jet frequently disrupts the cooling flow but only in the outer regions while it remains stable in the inner parts. The ICM up to  $30 \text{ kpc}$  is very robust to destruction and thusly long lived. This is why all the properties of cooling flows are found in these inner regions. Another result of this is, that clusters which do not show a cooling flow now will probably never form one.

This disruption of the flow reduces the effective age of the cooling flow way below the cluster age which therefore decreases the amount of expected cold gas by more than one order of magnitude. It is additionally reduced by the amount of gas accreted to the central black hole.

---

<sup>7</sup>A subtype of type **d** giant elliptical galaxies, often called supergiant elliptical.

Summing up, this idea could solve the cooling flow problem for clusters which show the assumed jets. It is however unlikely that this applies to all cooling flow clusters and can therefore be not a complete and universal answer to the mystery of the missing cooled gas.

Thinking a bit easier the radio emission of AGNs (or other sources like relativistic electrons) simply have a heating effect onto the ICM. However the argument still applies, that not every cooling flow cluster hosts necessarily a strong radio source. For those which do, the question arises if there is enough energy in the outflow and if enough of it can be transferred to the ICM to balance the cooling flow. Most likely it is only the kinetic energy of the jet or of the relativistic particles which is the relevant energy source. Additionally radio galaxies and radio quasar most likely deposit energy in the ICM. [Sarazin, 2008]

It is also important that the transported head is distributed evenly even through thermally unstable regions, which could be difficult. A model describing this process certainly needs a lot of fine tuning, since it needs to be self regulating according to the mass accretion rate. [Peterson et al., 2003]

Last but not least we want to consider one more effect which shall be in the main focus of the rest of this thesis. We have already shown earlier, that the temperature in the outer regions of cooling flow clusters are much hotter then the already cooled (and still cooling) inner parts. Therefore energy should be transported inwards via thermal conduction. The question how much this process can influence a cooling flow and how magnetic fields come into play will be discussed and evaluated in this thesis. The next two subsections go into details of micro-physics and explain how conduction works (without and also with a magnetic field). In subsection 2.3 we discuss the implications on clusters and compare our thoughts to observations.



## 2 Thermal conduction and magnetic fields

### 2.1 Isotropic thermal conduction

So let us start with the very basics of thermal conductivity. According to [Spitzer, 1956] the effect of heat conduction can be written as the heat flux

$$\vec{Q} = -\kappa \nabla T \quad (2.1.1)$$

which consists of the temperature gradient and the conduction coefficient  $\kappa$ . We assume a Lorentz gas, which means according to [McGraw-Hill Companies, 2013], that we keep the ions fixed ( $m_{ion} \gg m_e$ ) and neglect interactions between electrons. For this assumption we can calculate the conduction coefficient for so called Spitzer conductivity:

$$\kappa_{Sp} = 20 \left(\frac{2}{\pi}\right)^{3/2} \frac{(k_B T_e)^{5/2} k_B}{m_e^{1/2} e^4 Z \ln \Lambda} \quad (2.1.2)$$

With  $Z$  the average proton number of the plasma and the Coulomb logarithm  $\ln \Lambda$ . It is very important, that the conductivity depends strongly on the electron temperature. Therefore we can assume a reasonable effect for example in the cores of big clusters, where the plasma reaches temperatures up to about  $10^8 K$ .

For a real gas, the conductivity will be a factor times this conductivity:

$$\kappa = \delta \cdot \kappa_{Sp} \quad (2.1.3)$$

This factor has been calculated by [Spitzer and Härm, 1953] and is highly dependent on the average proton number of the plasma.  $\delta = 0.225$  for a pure proton electron plasma and rises up close to 1 for very big  $Z$ .

In the literature one can find various ways how to calculate a mean nucleus count, however there seems not to be one clear definition. Since we only need an estimate it is not important to really distinguish between different methods. Anyway we will need the mean molecular weight, so let us mention two ways to estimate a mean value for  $Z$ .

For plasmas of our interest we assume full ionization. We can easily derive the mean molecular weight and infer an approximate nucleus count from it. Let  $X$  be the hydrogen mass fraction and  $Y$  the helium mass fraction. We assume the contribution of heavier elements is negligible, so we have

$$X + Y = 1 \quad (2.1.4)$$

For fully ionized hydrogen we get 2 particles per proton mass and 3/4 particles per proton mass for helium (1 nucleus and 2 electrons)<sup>8</sup>. Therefore the number density of hydrogen / helium in our plasma is

$$n_H = \frac{2}{m_p} X \rho \quad n_{He} = \frac{3}{4m_p} Y \rho \quad (2.1.5)$$

So in total we have the number density of

$$n = \frac{\rho}{4m_p} \cdot (8X + 3Y) \quad (2.1.6)$$

Plugging in  $Y$  from eq. 2.1.4 we get

$$n = \frac{\rho}{4m_p} \cdot (5X + 3) \quad (2.1.7)$$

Defining the mean molecular weight through  $\rho = n \cdot \mu$  and assuming the hydrogen mass fraction being  $X = 0.76$ , we get in total

$$\mu = m_p \cdot \frac{4m_p}{(5X + 3)} = m_p \cdot 0.588 \quad (2.1.8)$$

Therefore we can estimate a mean nuclear count as

$$Z \sim \frac{1}{0.588} \approx 1.7 \quad (2.1.9)$$

---

<sup>8</sup>We assume  $m_H = m_p = m_n$

Another possibility is to use the approach described in [Spitzer and Härm, 1953]:

$$Z = \frac{\sum_i n_i Z_i^2}{n_e} \quad (2.1.10)$$

where we sum over all contributing ions in the plasma. Since we need ion number densities now, we have to redefine them like

$$n_{H^+} = \frac{1}{m_p} X \rho \quad n_{He^{2+}} = \frac{1}{4m_p} Y \rho \quad (2.1.11)$$

Furthermore we get electrons from both types of atoms. We can then write the electron number density as

$$n_e = \left( \frac{1}{m_p} X + \frac{2}{4m_p} Y \right) \rho \quad (2.1.12)$$

Plugging these values into equation 2.1.10 we get

$$Z \approx 1.136 \quad (2.1.13)$$

From the order of magnitude we gain from these two approaches, we get  $\delta \approx 0.3$  by taking the tabulated values from [Spitzer, 1956].

When used for cosmological simulations one often assumes a pure hydrogen plasma. A typical used value for  $\kappa$  is then e.g. given by [Sarazin, 1986]

$$\begin{aligned} \kappa &= 1.31 \cdot n_e \lambda_e k_B \left( \frac{k_B T_e}{m_e} \right)^{1/2} \\ &= 4.6 \cdot 10^{13} \left( \frac{T_e}{10^8 K} \right)^{5/2} \frac{40}{\ln \Lambda} \frac{erg}{s \text{ cm } K} \end{aligned} \quad (2.1.14)$$

with the electron number density  $n_e$  and the mean free path of the electrons  $\lambda_e$ . Since the particles mass enters in the denominator, we can infer, that electrons give a much bigger contribution to heat conduction than protons. This makes totally sense, since lighter particles have higher velocities at the same temperature and can be accelerated much easier. This increases the amount of collisions in an given time drastically. Consequently only the values for electrons are considered

in the formula. Therefore we will from now on omit the index  $e$  in our equations. We neglect any dependency of the Coulomb logarithm on temperature and electron density and plug in  $\ln \Lambda = 37.8$  for typical plasmas of our concern, which is a fairly good approximation. More precise calculations for different collision types (e.g. electron-electron or electron-proton) can be found in [Huba, 2011]. What remains is the strong dependence on temperature to the power of  $5/2$ .

Furthermore we need to apply an important correction to equation 2.1.14. So far we assumed, that the typical length scale of the temperature gradient  $l_T = T/|\nabla T|$  would be always much bigger than the mean free path. However for very low density plasmas one cannot expect a good conductivity even if the temperature rises very much. [Cowie and McKee, 1977] have calculated the saturated heat flux for this case as

$$Q_{sat} = 0.4n_e k_B T \left( \frac{2k_B T}{\pi m} \right)^{1/2} \quad (2.1.15)$$

Interpolating between these findings and the common Spitzer conduction coefficient we get the corrected heat flux as

$$Q_{tot} = \frac{\kappa \cdot T}{l_T + 4.2\lambda} \frac{\nabla T}{|\nabla T|} \quad (2.1.16)$$

Alternatively we can just redefine the conduction coefficient as

$$\kappa = \frac{\kappa_{Sp}}{1 + 4.2\lambda/l_T} \quad (2.1.17)$$

A discussion about this saturation effect and why Spitzer conduction is applicable can be also found in [Rosner and Tucker, 1989].

## 2.2 Anisotropic thermal conduction

Now that we have seen the equations for general heat conduction, we add magnetic fields to the picture. As already mentioned in the last subsection, thermal conduction is basically due to Coulomb collisions of charged particles. Except these collisions, particles were so far allowed to move freely in the plasma. However in the presence of a magnetic field, the movement perpendicular to the field lines is restricted: The electrons will move in spirals around the field lines. The frequency of the circular motion is called larmor- or gyrofrequency:

$$\omega_g = \frac{eB}{m_e c} \quad (2.2.1)$$

To see, how this affects the capability of the electrons to transport energy we will present some phenomenological ideas and scaling relations following [[Frank-Kamenezki, 1967](#)].

At first we will present some thoughts, how general diffusion is affected by magnetic fields. Due to the similar microscopic origin we can then infer the same relations to hold also for thermal conduction. We will show the exact relation between diffusion- and conduction coefficients later in this section.

At first we need the connection between mean free path and collision time via the particle's velocity:

$$\lambda \approx v\tau \quad (2.2.2)$$

A typical diffusion coefficient of units  $cm^2 s^{-1}$  can be defined as

$$D \approx \lambda v \approx v^2 \tau \approx \frac{\lambda^2}{\tau} \quad (2.2.3)$$

Since the movement parallel to the magnetic field are not affected, the diffusion along the field lines should not be affected:

$$D_{\parallel} = D \quad (2.2.4)$$

We assume that movement of particles perpendicular to magnetic field lines can only be done by jumps between cyclotron trajectories, which gives us a diffusion

coefficient like

$$D_{\perp} \approx \frac{v^2}{\omega_g^2 \tau} \approx \frac{lv}{w_g^2 \tau^2} \quad (2.2.5)$$

Therefore the relation between the two coefficients is about

$$\frac{D_{\perp}}{D_{\parallel}} \approx \frac{1}{\omega_g^2 \tau^2} \propto B^{-2} \quad (2.2.6)$$

This is however only valid if  $\omega_g \tau \gg 1$ , which we will check soon for a typical intra cluster medium. In other words, the gyroradius has to be much smaller than the mean free path. Which makes totally sense, if we want the magnetic field to impose a real restriction onto the electrons movement. If we get in the regime of  $\omega_g \tau \sim 1$  we have to change the relation in order to ensure  $D_{\perp} \leq D_{\parallel}$ :

$$\frac{D_{\perp}}{D_{\parallel}} \approx \frac{1}{1 + \omega_g^2 \tau^2} \quad (2.2.7)$$

To evaluate this relation we need the collision time or the corresponding frequency

$$\frac{1}{\tau} = \nu = \frac{\omega_{pl}}{n \lambda_D^3} \quad (2.2.8)$$

with the plasma frequency

$$\omega_{pl} = \sqrt{\frac{4\pi n_e e^2}{m_e}} \quad (2.2.9)$$

and the Debye length

$$\lambda_D = \sqrt{\frac{k_B T}{4\pi n_e e^2}} \quad (2.2.10)$$

Plugging these relations into eq. 2.2.8, we get

$$\nu = \frac{16\pi^2 c e^3 \sqrt{m_e} n_e^2}{(k_B T)^{3/2} B} \approx 171.4 \frac{n_e^2}{T^{3/2}} \frac{cm^6 K^{3/2}}{s} \quad (2.2.11)$$

To check the order of magnitude of the relation between perpendicular and parallel diffusion coefficient, we plug in typical values of the following variables (for galaxy clusters):

- $B = 10^{-6} G$
- $T = 10^7 K$
- $n = 10^{-3} cm^{-3}$

Equation 2.2.6 gives us then a factor of  $\frac{D_{\perp}}{D_{\parallel}} \approx 10^{-28}$  which means, that conduction perpendicular to the magnetic field will be extremely suppressed.

Additionally [Rosner and Tucker, 1989] derive a criterion for the minimum magnetic field which is needed for anisotropic conduction:

$$\begin{aligned}
 B \gtrsim B_{crit} &= 1.6 \cdot 10^{-11} \left( \frac{n}{10^{-4} cm^{-3}} \right)^{2/3} \left( \frac{T}{10^8 K} \right)^{-1/6} \left( \frac{\ln \Lambda}{20} \right)^{1/3} G \\
 &\approx 9.2 \cdot 10^{-11} \left( \frac{n}{10^{-3} cm^{-3}} \right)^{2/3} \left( \frac{T}{10^8 K} \right)^{-1/6} G
 \end{aligned}
 \tag{2.2.12}$$

As we will see later in our cluster simulations (please see section 5), this condition is in general fulfilled in all of the ICM.

These relations are however only a rough estimate. From experiments the empirical knowledge was gained, that perpendicular diffusion is additionally overlaid with some kind of turbulence which is extremely difficult to describe.<sup>9</sup> However their experiments show, that the scaling with the magnetic field effectively changes from  $B^{-2}$  to  $B^{-1}$ , which leads us to so called Bohm diffusion. Without going into detail here, we just try to construct a scaling relation for this kind of behaviour, similar to the calculations above:

$$D_{\perp} \approx \frac{v^2}{\omega_g} \approx \frac{k_B T c}{e B}
 \tag{2.2.13}$$

Assuming that the electrons move with their thermal speed  $v \approx \sqrt{k_B T / m}$ . This is again only a very rough estimate since plasma instabilities will also play a role

---

<sup>9</sup>One example where this plays an important role are Tokamak fusion reactors.

here. Neglecting any further influence, we get in total

$$\frac{D_{\perp}}{D_{\parallel}} \approx \frac{1}{\omega_g \tau} \quad (2.2.14)$$

which allows a much stronger diffusion orthogonal to the magnetic field lines.

As already mentioned, the conduction coefficients should scale similar to the diffusion coefficients we just discussed. We can prove this through some easy scaling relations starting with the ideal gas law

$$pV = Nk_B T \quad (2.2.15)$$

Assuming a more or less constant density we can infer

$$\nabla p = nk_B \nabla T \quad (2.2.16)$$

Knowing that the source of a heat flux corresponds to the time evolution of pressure we can write using equation [2.1.1](#)

$$\frac{\partial p}{\partial t} \sim \nabla \cdot Q \rightarrow nk_B \frac{\partial T}{\partial t} \sim \nabla \cdot (\kappa \nabla T) \quad (2.2.17)$$

Taking the typical length and timescales instead the derivatives we get

$$\kappa \sim \frac{l^2}{\tau} \cdot nk_B \sim D \cdot nk_B \quad (2.2.18)$$

where we can identify the diffusion coefficient  $D$ . According to this relation, the two coefficients scale similarly and we can therefore use the derived equations for an implementation of anisotropic thermal conduction.

A more detailed analysis of anisotropic diffusion and therefore conduction can be found for example in [Golant et al., 1980]. Since we have already seen from simple scaling relations, that conduction perpendicular to magnetic fields will be extremely suppressed, we are not dependent on the exact relation to the parallel component. It is however important, that Golant et al. come to similar results in terms of proportionality:

- Eq. (9.17):  $D_{\perp}/D_{\parallel} \propto B^{-2}$  like our equation 2.2.6
- Eq. (9.37):  $\kappa_{\perp} \propto D_{\perp} \cdot n$  is exactly our equation 2.2.18, since they pull the  $k_B$  out of the definition of  $D$

For highly tangled magnetic fields [Pistinner and Shaviv, 1996] discussed, if the coherence length should take over for the mean free path instead of the gyroradius. However they come to the conclusion, that this assumption is wrong. This matches the considerations of [Rosner and Tucker, 1989], who come to the conclusion, that tangled magnetic fields do not suppress thermal conduction very strongly, despite general belief. Their results state a reduction factor of  $\langle \cos \delta\theta \rangle^2$  which is an averaging over the local angles between magnetic field lines and the temperature gradient. We will briefly analyse this behaviour for totally random magnetic field configurations in section 4.3.1.

Summing up, we can in general say, that thermal conduction perpendicular to magnetic fields lines with reasonable field strengths is nearly totally suppressed. If we come into a regime, where we need to apply scaling relations regarding the magnetic fields, we have seen that  $\kappa_{\perp}/\kappa_{\parallel}$  can scale like something between  $B^{-2}$  and  $B^{-1}$ .

## 2.3 Implications on cluster cooling flows

Having learned about the details of thermal conduction as an isolated process, the question is now, how does this influence our picture of cooling flows in galaxy clusters.

In figure 1 we have seen, that the temperature profiles of clusters show strong temperature gradients, especially near their center. Since basic (isotropic) thermal conduction only requires the existence of such gradients, it will definitely occur. That aside, it is important to determine if the process is strong enough to play a role in the whole picture!

Let us have a look back at equation 2.1.14. If thermal conduction behaves like ideal Spitzer conduction, we see, that it is proportional to the electron density as well as on temperature. Although it is true, that the ICM has in general fairly low densities, we have already seen, that the temperatures in the ICM can be quite high. Since  $\kappa$  is proportional to  $T^{5/2}$  we can expect thermal conduction to be important at least in hotter regions of a cluster.

Since Spitzer conduction is calculated for an idealised plasma, conduction in reality will probably be a bit less effective than in the Spitzer case. Additionally we have argued in the last subsection, that magnetic fields suppress the transport of energy perpendicular to the field lines. Overall, this results in a certain suppression factor, which we have to apply onto Spitzer conductivity.

A derivation of a typical suppression factor can be found in [Narayan and Medvedev, 2001]. For details see also [Rechester and Rosenbluth, 1978] and [Chandran and Cowley, 1998]. At first they derive, that the effective conduction should be at least a factor 100 less than Spitzer conduction, even for chaotic magnetic fields for which a slightly higher effect is claimed. If this were the case, we could immediately forget about thermal conduction with magnetic fields having any effects on gas dynamics in galaxy clusters. However [Narayan and Medvedev, 2001] argue further, that in presence of very strong turbulence the picture changes again, but this time in favour of conductivity. They claim, that the effective conduction

coefficient can be nearly as strong as Spitzer conduction. As a final value they give

$$\kappa = \frac{\kappa_{sp}}{3} \tag{2.3.1}$$

which can be seen as conduction being effective only in one of three spatial dimensions due to the magnetic field.

Considering these calculations there exists no final answer yet. [Loeb, 2002] for example claims, that conduction must be suppressed by  $\kappa \leq 0.15 \cdot \kappa_{sp}$ .

We already stated, that if strong enough, thermal conduction could be the heating mechanism which helps us to stabilize cooling flows and solve the observational problems. Since conduction has to be added to the energy equation of whatever cooling flow model one assumes, it is hard to determine if this is really possible. Therefore we will dedicate the rest of this thesis to discuss a numerical implementation of anisotropic thermal conduction and the analysis of cosmological simulations with the new code.

But before we come to that, we want to show one prominent example for suppressed conduction by magnetic fields: We have already shown, that magnetic fields in clusters exists and that they are usually strong enough to strongly suppress thermal conduction. We want to further motivate this statement through observational evidence:

Observers often find so called *cold fronts* in galaxy clusters, for example in **Abell 2142** (for details please see [Owers et al., 2009] and [Owers et al., 2011]). There are different characteristics of cold fronts which hold evidence for anisotropic thermal conduction. Basically they are regions with continuous pressure ( $\rightarrow \nabla p = 0$ ) where the temperature suddenly drops typically by a factor of 2 ( $\rightarrow \nabla T \neq 0$ ). This surface brightness discontinuity is observed very well.

At first one thought of the cold front as a merger shock. Temperature measurements however lead to the believe of a contact discontinuity between hot, diffuse and colder, denser gas. The front presents itself as a very sharp feature, which is in general narrower than 2 *kpc*. This is less than the typical mean free path of an

electron in these regions.

For this feature to be stable enough to be common in many galaxy clusters, thermal conduction has to be strongly suppressed across the cold front. Otherwise it would wipe out the temperature gradient pretty fast. Since the two separated regions intrinsically have a constant temperature, thermal conduction is indeed working along the front smoothing the temperature profile inside each part. This is exactly the kind of anisotropy which can be explained by magnetic fields as we argued before.

The two different regions of a cold front probably consist out of gas of different subclusters with a different magnetic structure, which does not mix (or at least very slow). Gas motion then tends to even increase the temperature gradients and align the magnetic field lines more along the cold front. Also tangled magnetic field lines can lead to a similar result. [Fabian, 2002, Sarazin, 2008, Komarov et al., 2013]

Many groups have already considered thermal conduction as possible heating mechanism and the outcomes cover the full range of possibilities. For further reading we want to give some short examples for different opinions:

- [Binney and Cowie, 1981]: Thermal conduction is important and has to be suppressed below 1% of the Spitzer value.
- [Bregman and David, 1989]: Thermal conduction does not solve the problems we have.
- [Rosner and Tucker, 1989]: Tangled magnetic fields do not suppress thermal conduction so much, that it can be ignored. It plays an important role to when it comes to cooling flows but thermal conduction alone is not sufficient to solve the cold gas problem.
- [Fabian, 2002], [Peterson et al., 2003]: Thermal conduction plays a role but needs to be combined with other processes for a sufficiently big effect.

- [Zakamska and Narayan, 2003]: Thermal conduction can be assumed to be suppressed to a value of about 30% of Spitzer conduction. It is essential for thermal stability in clusters. Some clusters need an additional source of heat, but thermal conduction is always an important factor and a sufficient component to match models and observations for several galaxy clusters.
- [Voigt and Fabian, 2004]: Conduction of the order of the Spitzer value can offset cooling in regions with  $T \geq 5 \text{ keV}$ . However mass deposition rates from spectral information does not match expectations from radiative cooling, therefore another process is additionally needed. For example turbulent heat diffusion could be the key.
- [Fabian et al., 2006]: Conduction needs to be suppressed by at least a factor 100 to allow filaments observed in the soft X-ray to be long lived.

Before we come to a description of our numerical schemes, we finish this section with a short excursion on magnetic fields themselves and their detection, since their structure and order of magnitude will play a crucial role in our cosmological simulations.

## 2.4 Short excursion: Detection of magnetic fields

Now that we have talked about magnetic fields, we want to give a brief overview on detection techniques of magnetic fields. For more detailed information see for example [Soker and Sarazin, 1990], [Kronberg, 1994], [Soker, 1997] and [Soker, 2010].

The existence of magnetic fields can be easily proved by radio observations. As already mentioned, identifying synchrotron radiation is a sufficiently strong evidence for magnetic fields and relativistic electrons. However we can not determine the small scale structure of the field lines by these observations for cosmological applications.<sup>10</sup> Furthermore a lot of galaxies and galaxy clusters are radio silent with respect to synchrotron radiation and we need other methods to determine the properties of magnetic fields, which are pretty complicated. Therefore we will only shortly present two possibilities in the following:

1. Observing the Zeeman splitting of emission lines
2. Using the Faraday rotation measure

The first method is not very successful for galaxy cluster observations since the observed lines are smeared out by a lot of other processes, dominated by the Doppler effect. Therefore Zeeman splitting is usually not visible any more and we can neglect this method here.<sup>11</sup>

The Faraday effect describes the interaction between a magnetic field and light in a medium: An electromagnetic wave enters a plasma, which leads to a change of the polarization plane due to interaction of free charged particles with the wave. The so called rotation measure  $RM$  is then defined as the rotation of the light's polarization plane over the observed wavelength squared. It is related to the magnetic field via an integral over the line of sight:<sup>12</sup>

$$\frac{\chi}{\lambda^2} = RM = 8.1 \cdot 10^5 \int n_e \vec{B} \cdot \vec{dl} \frac{rad}{m^2} \quad (2.4.1)$$

<sup>10</sup>For example the magnetic field of the sun can be studied pretty well using synchrotron radiation, because we get a much higher resolution for such a small distance.

<sup>11</sup>Zeeman splitting can be used for example to determine magnetic fields of nearby molecular clouds.

<sup>12</sup>So  $RM$  is proportional to the magnetic field component along the propagation direction of the observed light.

Typical values measured are  $RM = 10^2 - 10^4 \text{ rad}/m^2$ .

This approach has again two important limitations: We can determine only the integral over the line of sight, therefore we get only some kind of mean magnetic field where anti-parallel parts cancel each other out. Therefore the result can be seen as a lower limit. Furthermore the integral is not just over  $B$ , but involves also the electron number density. Therefore we need additional measurements to get information about the densities to infer proper results for the magnetic fields.

For **NGC 1275** [Taylor et al., 2006] even find values for the rotation measure between 6500 and 7500  $\text{rad}/m^2$ . They estimate the electron number density as  $n_e \approx 0.31/cm^3$  and assume a relevant path length for the magnetic region of  $2kpc$ . Applying an additional factor of  $\sqrt{3}$  to account for the one-dimensionality of the method, this leads to magnetic fields of about  $25\mu G$ .

Therefore the magnetic pressure can be comparable or even bigger than thermal pressure in some regions of clusters. One example where this is confirmed is **Hydra A** ([Kronberg, 1994], [Soker, 2010]; for a radio map see figure 10). This happens typically in regions  $r \lesssim 10 \text{ kpc}$ . Therefore magnetic fields are not only important for conduction but also influence hydrodynamics strongly as a pressure source. Farther out from the center the gas pressure dominates again on large scales. At the cooling radius one can estimate the pressure fraction as

$$\frac{P_B}{P_{gas}} = 5.9 \cdot 10^{-4} \left( \frac{B}{1\mu G} \right)^2 \left( \frac{n}{3 \cdot 10^3 cm^{-3}} \right)^{-1} \left( \frac{T}{7 \cdot 10^7 K} \right)^{-1} \quad (2.4.2)$$

Inside this region reconnection of magnetic field lines is efficient. Equipartition of magnetic and gas pressure at  $r = r_B$  leads to a typical energy output of  $10^{42} - 10^{43} \text{ erg}/s$  in a region of at least  $1 \text{ kpc}$ . This depends on the temperature of the gas as well as on the net accretion rate  $\dot{M}$  of the cooling flow:

$$\dot{E}_{rec} \approx 1 \cdot 10^{43} \left( \frac{T(r_B)}{1 \cdot 10^7 K} \right) \left( \frac{\dot{M}(r_g)}{100 M_\odot yr^{-1}} \right) \text{ erg}/s \quad (2.4.3)$$

The energy output goes mostly into heating and ionization of the surrounding gas and also accelerates the non thermal particles which leads to the diffuse radio emis-

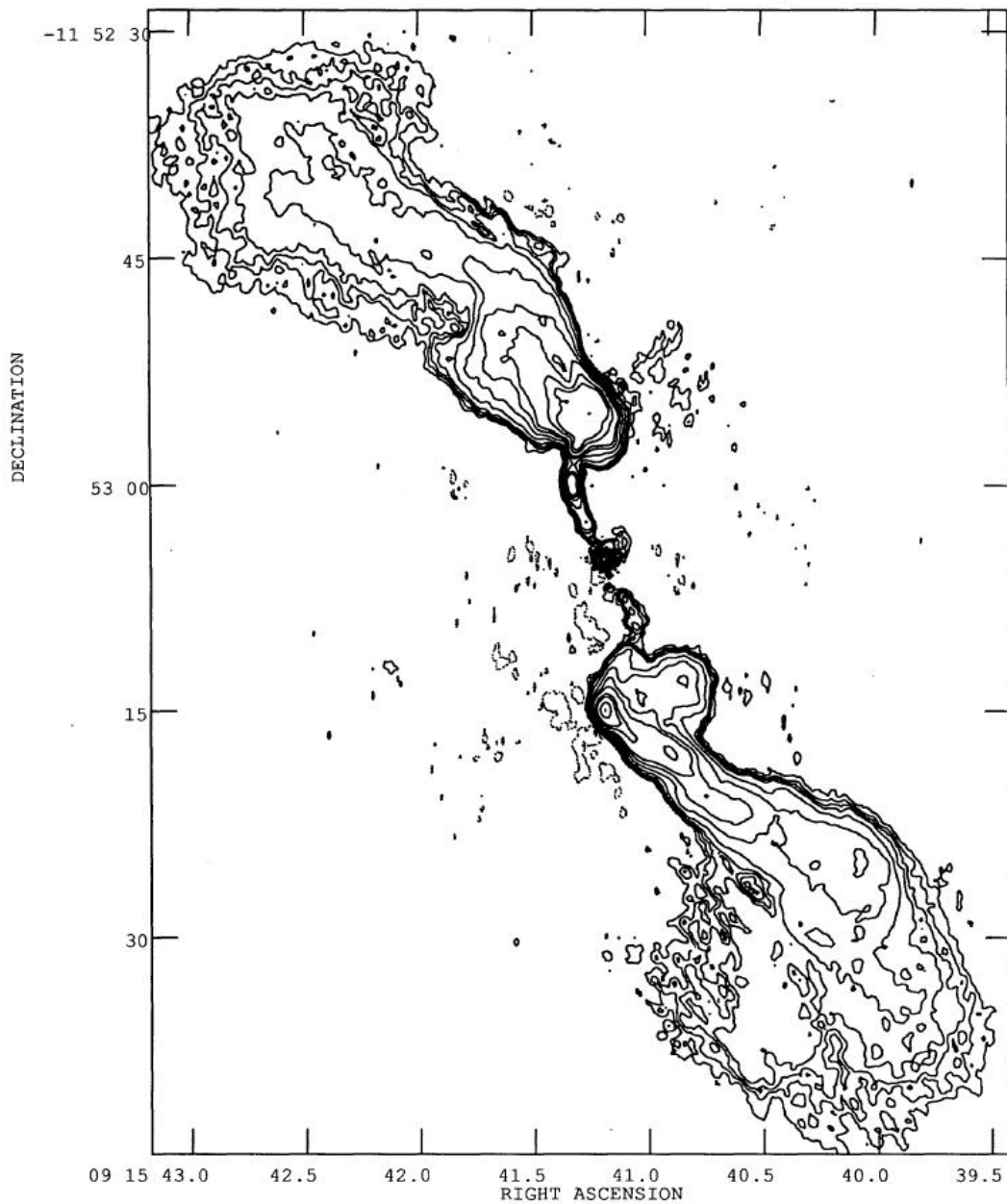


Figure 10: Total intensity distribution of radio observations of **Hydra A** (**3C 218**). One can very well see the two radio lobes and the outflowing jets of the object. For the rotation measure values between  $-1000$  and  $+3300$   $\text{radians}/m^2$  are measured for the northern lobe, while the southern lobe seems to have stronger values. The plot is taken from [Taylor et al., 1990].

sion observers find for example in **NGC 1275** in the **Perseus** cluster (see section 1.2 for details). However the output energy is still much less, than is cooled away in X-ray. Therefore this can not work as a single balancing process, as we have already stated earlier.

Since the infall of gas will provide a mostly radial magnetic field on large scales, it is the radial component which will be probably reduced at most. Therefore the magnetic field becomes more isotropic within  $r_B$ . However this does not tell us anything about the small scale structure of a typical cluster magnetic field. It is still very difficult to get reliable results about small scale properties.

One proposition are for example the so called flux loops which would suppress buoyancy and stabilize clouds against gravitational collapse as well as moving cool, high density blobs against disruption.

A typical geometry is shown in figure 11. As one can see, there would be hardly any connection from the outer to the inner parts of the cluster, since the loops are too short to connect gas over the whole cooling region and beyond. Therefore inward thermal conduction would be totally suppressed without reconnection of magnetic field lines. This presents the problem, that it is very hard to construct a self consistent magnetic field which suffices all our requirements.

On the other hand [Pistinner and Shaviv, 1996] argue, that flux loops would be stretched by the inward flow and break at some point. This would allow reconnection and prevent suppression of thermal conduction.

Additionally [Rosner and Tucker, 1989] argue, that besides the mentioned stability issues magnetic bubbles are unlikely because of the lack of a convincing generation mechanism. Furthermore they pose the question, how the observed homogeneous temperature distributions could be formed with such a magnetic field configuration.

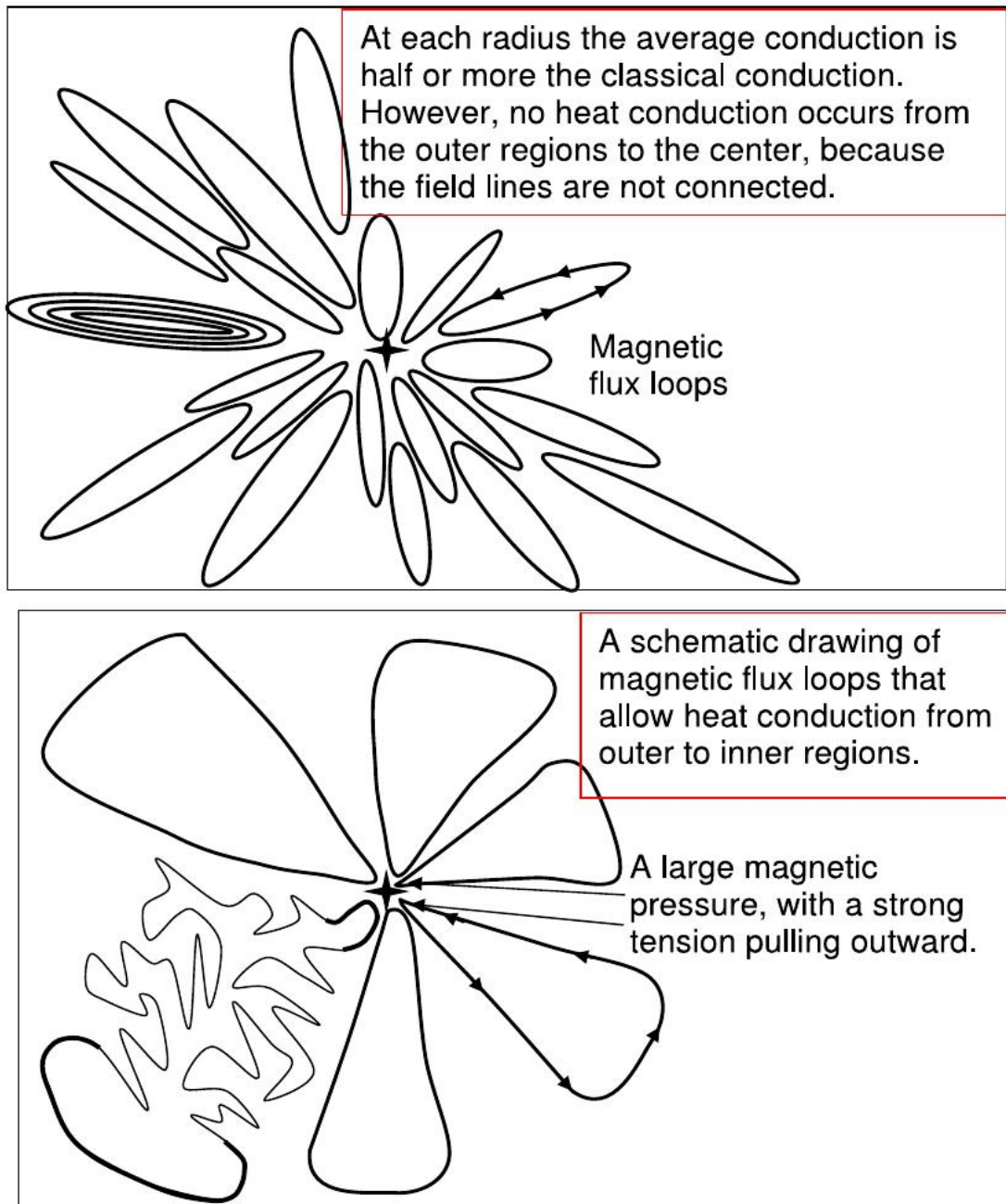


Figure 11:

*Upper Panel:* Magnetic flux loops with magnetic fields inside each loop (like drawn on the left for clarity). There is no conduction from outer to inner regions.

*Lower Panel:* A magnetic structure which allows radial conduction. Magnetic fields are very strong in near the center, even for strongly tangled field structures (lower left). [Soker, 2010]

The last thing we want to mention because we will test for it later, is the inferred total structure of the magnetic field lines in many models. [Soker, 1997] state that, due to conservation of magnetic flux, the radial and the tangential components should scale like

$$B_r \propto r^{-2} \tag{2.4.4}$$

$$B_t \propto (r \cdot v_{in})^{-1} \tag{2.4.5}$$

with the infall velocity of the gas  $v_{in}$ . Our results regarding these relations will be shown in section 5.2.

But for now let us come back to the problem we want to solve: We want to extensively test the implications of thermal conduction onto cluster dynamics, including the influence of magnetic fields. Since we can not do this analytically we have to consider a numerical code including all the physical processes and models we need. For this we want to implement anisotropic conduction into the SPH code GADGET-3. In the next section we review the basics about SPH and afterwards discuss in detail the numerical formulation of thermal conduction, tests and finally the analysis of some cluster simulations.



### 3 Smoothed Particle Hydrodynamics

In the following section we will present one of the common numerical schemes to perform hydrodynamic simulations, which is called *Smoothed Particle Hydrodynamics*.

In this brief overview of the basics we will follow the review articles of [Monaghan, 1992], [Dolag et al., 2008a][Springel, 2010] and mainly [Price, 2012]. The purpose is, to give the reader a basic understanding how SPH codes and discretizing equations in SPH work. For our simulations we are using the latest version of GADGET-3. Details about the last publicly available version (GADGET-2) can be found for example in [Springel, 2005a], [Springel, 2005b]. Regarding the implementation of MHD please see [Dolag and Stasyszyn, 2009].

In this and all following sections we will use always the following nomenclature:

- $\mathbf{i}$  will denote the index of the particle for which we are calculating a quantity
- $\mathbf{j}$  and  $\mathbf{k}$  will always stand for summation indices over other particles (usually neighbouring to  $\mathbf{i}$ , but we will indicate that in the upper summation boundary with a  $N_{ngb}$ )
- $\alpha$  and  $\beta$  will be used to indicate components of vectors or matrices. We will in some parts use the Einstein sum convention for these indices<sup>13</sup>

#### 3.1 Lagrangian derivation of SPH equations

SPH uses fictive particles to model fluid dynamics. Let us start with the computation of a very basic quantity of fluids: the density. In figure 12 one can see different approaches, how to calculate density. Overlaying the particles with a fixed grid, one could simply divide the total mass of particles in a cell by the cell volume. The next step to improve the result could be, not to take a grid but a local volume around each particle. Further improving the latter by weighting the neighbouring particles by their distance, one arrives at the SPH approach.

---

<sup>13</sup>I.e. summing over all twice occurring indices

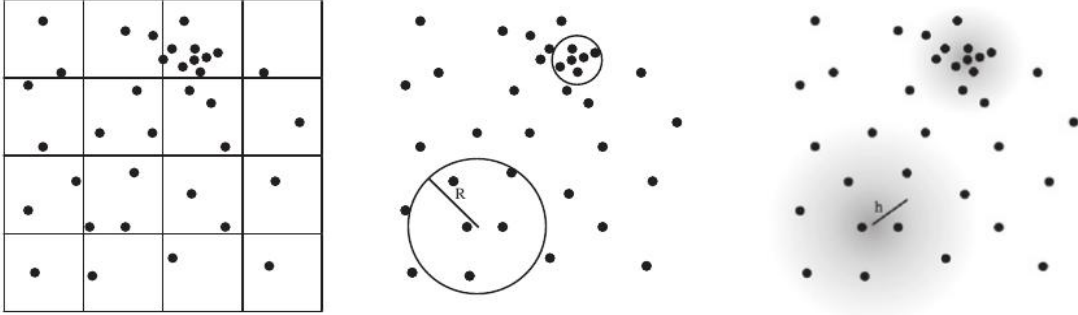


Figure 12: Different ways to estimate the density: Count mass in a volume around each particles via a fixed grid, a local volume or a smoothed local volume. [Price, 2012]

Written in a formula, the third approach looks like

$$\rho(\vec{x}) = \sum_{j=1}^{N_{ngb}} m_j W(\vec{x} - \vec{x}_j, h) \quad (3.1.1)$$

where  $W$  is the function, with unit of an inverse volume, determining the weights applied to the neighbour particles. We call  $W$  the *kernel*.  $h$  is a parameter which determines the support radius of  $W$ , further called *smoothing length*. Additionally the particle spacing plays a role here.

Conservation of total mass gives us one basic condition on the choice of  $W$ :

$$\int_V d\vec{x}' W(\vec{x}' - \vec{x}_j, h) = 1 \quad (3.1.2)$$

Obviously the density estimate depends strongly on a good choice of the kernel, therefore we can define some more conditions how a suitable kernel function should look like:

- The kernel should be positive and monotonically decreasing, so that nearby particles have the biggest effect in the calculation.
- At least the first two derivatives of  $W$  should be smooth.
- The kernel should be symmetric with respect to particle spacing, i.e. it should only depend on the absolute value of the distance vector  $|\vec{x}_i - \vec{x}_j|$ .

- It should contain a central flat plateau to be insensitive to distance fluctuations of nearby particles.
- To save computation time the kernel should only involve a certain number of neighbours and be smoothly truncated at some point (i.e. it should have a finite support radius and therefore not involve all other particles but only the nearest neighbours).

A natural and easy choice which fulfils the first four conditions is the Gaussian function. The fifth condition is however strongly violated, because the Gaussian has an infinite domain. Since particles far away would not give big contributions (as requested by the first condition), one could simply truncate a Gaussian at some point, which would however destroy the smoothness. This makes a Gaussian a good choice by the strictly needed conditions, however not a very clever one. We will later in section 3.3 go into more detail about possible choices for the kernel function and their quality. Let us for the moment assume we have found a function which suits our needs and see, how we can proceed.

We still have to define the smoothing length appropriately. There are several strategies for this. A natural choice would be to relate the smoothing length to the number density of particles:

$$h(\vec{x}) \propto n(\vec{x})^{-1/d} \quad (3.1.3)$$

with  $d$  the amount of spatial dimensions we consider. Since  $n$  itself is related to the density which depends on  $h$ , we have to calculate  $h$  and  $\rho$  iteratively at the same time. Assigning individual smoothing lengths to each particle, this gives us two equations of the form

$$\rho_i = \sum_{j=1}^{N_{ngb}} m_j W(\vec{x}_i - \vec{x}_j, h_i) \quad (3.1.4)$$

$$h_i = \eta \left( \frac{m_i}{\rho_i} \right)^{1/d} \quad (3.1.5)$$

The next step is to build a fully conservative scheme for (magneto-)hydrodynamics

equations with this formalism.<sup>14</sup> We start with the the Lagrangian of the system, which is dependent on particle velocities and specific internal energies:

$$L = T - V = \sum_j m_j \left( \frac{1}{2} v_j^2 - u_j \right) \quad (3.1.6)$$

By applying the principle of the least action we directly get the Euler-Lagrange equations for each particle  $i$ :

$$\frac{d}{dt} \left( \frac{\partial L}{\partial \vec{v}_i} \right) - \frac{\partial L}{\partial \vec{x}_i} = \frac{d}{dt} (m_i \vec{v}_i) + \sum_j m_j \left. \frac{\partial u_j}{\partial \rho_j} \right|_s \frac{\partial \rho_j}{\partial \vec{x}_i} = 0 \quad (3.1.7)$$

assuming a constant entropy  $s$ .<sup>15</sup> To calculate the derivative of the specific internal energy we have to consider basic thermodynamics. Transforming the first law to specific quantities,<sup>16</sup> we get:

$$du = \left. \frac{\partial u}{\partial s} \right|_\rho ds + \left. \frac{\partial u}{\partial \rho} \right|_s d\rho = T ds + \frac{p}{\rho^2} d\rho \quad (3.1.8)$$

We get the density gradient by differentiating equation 3.1.4:

$$\frac{\partial \rho_j}{\partial \vec{x}_i} = \frac{1}{\Omega_j} \sum_{k=1}^{N_{ngb}} m_k \frac{\partial W_{jk}}{\partial \vec{x}_i} (\delta_{ij} - \delta_{ik}) \quad (3.1.9)$$

with  $\Omega_j$  accounting for the density dependence of the smoothing length  $h$ . For simplicity we will from here on neglect this and simply set  $\Omega = 1$ . Here we introduced the short notation for the kernel  $W_{ij} = W(|\vec{x}_{ij}|, h_i) = W_{ji}$ .

Plugging these relations together into equation 3.1.7 and canceling one sum with the Dirac  $\delta$  functions, we get the equation of motion

$$\frac{d\vec{v}_i}{dt} = - \sum_{j=1}^{N_{ngb}} m_j \left( \frac{p_i}{\rho_i^2} - \frac{p_j}{\rho_j^2} \right) \nabla_i W_{ij} \quad (3.1.10)$$

<sup>14</sup>In this subsection we will restrict ourselves to pure hydrodynamics. We will come to MHD in subsection 3.4.

<sup>15</sup>Constant entropy equals no dissipation.

<sup>16</sup>Therefore dividing by mass.

The energy equation in absence of dissipation can be derived using again the density estimate (eq. 3.1.4) and the first law of thermodynamics (eq. 3.1.8):

$$\frac{du_i}{dt} = \frac{p_i}{\rho_i^2} \frac{d\rho_i}{dt} = \frac{p_i}{\rho_i^2} \sum_{j=1}^{N_{ngb}} m_j (\vec{v}_j - \vec{v}_i) \cdot \nabla_i W_{ij} \quad (3.1.11)$$

Before we go more into technical details about SPH discretizations, we want to briefly discuss the conservation properties of the formulation we just derived.

### Total linear momentum conservation

$$\frac{d}{dt} \sum_i m_i \vec{v}_i = - \sum_i m_i \sum_j m_j \left( \frac{p_i}{\rho_i^2} - \frac{p_j}{\rho_j^2} \right) \nabla_i W_{ij} = 0 \quad (3.1.12)$$

because of the antisymmetry of the kernel gradient: Since the kernel by construction depends only on the distance of two particles and the smoothing length, it is symmetric under particle exchange for constant smoothing lengths. Therefore we have an antisymmetric gradient of the kernel. For individual smoothing lengths we get a more complicated picture. Without proving this in detail we state, that the equation mentioned above still holds in this case. Additionally one often uses symmetrized kernel derivatives in SPH equations to use both smoothing lengths, which simplifies these kind of considerations.

### Total angular momentum conservation

$$\frac{d}{dt} \sum_i \vec{x}_i \times m_i \vec{v}_i = - \sum_i m_i \sum_j m_j \left( \frac{p_i}{\rho_i^2} - \frac{p_j}{\rho_j^2} \right) \vec{x}_i \times \nabla_i W_{ij} = 0 \quad (3.1.13)$$

using

$$\vec{x}_i \times \nabla_i W_{ij} = \vec{x}_i \times (\vec{x}_i - \vec{x}_j) W'_{ij} = -(\vec{x}_i \times \vec{x}_j) W'_{ij} = (\vec{x}_j \times \vec{x}_i) W'_{ij} \quad (3.1.14)$$

with  $W'_{ij}$  being the derivative of  $W_{ij}$  by it's argument  $\vec{x}_{ij}$ .

### Total energy conservation

Since the Lagrangian does not depend explicitly on time, the total energy is simply given by the Hamiltonian

$$H = \sum_i \vec{v}_i \cdot \frac{\partial L}{\partial \vec{v}_i} - L = \sum_i m_i \left( \frac{1}{2} v_i^2 + u_i \right) \quad (3.1.15)$$

which equals the kinetic plus the internal energy. Plugging in the equation of motion and the energy equation we derived earlier, we can easily show energy conservation with the same antisymmetry arguments as before.

$$\begin{aligned} \frac{dE}{dt} &= \sum_i m_i \left( \vec{v}_i \cdot \frac{d\vec{v}_i}{dt} + \frac{du_i}{dt} \right) \\ &= - \sum_i m_i \sum_j m_j \left[ \frac{p_i}{\rho_i^2} \vec{v}_j + \frac{p_j}{\rho_j^2} \vec{v}_i \right] \cdot \nabla_i W_{ij} \\ &= 0 \end{aligned} \quad (3.1.16)$$

For further applications we want to define the entropy function  $A$  through the equation of state for an ideal gas:

$$A(s) = \frac{p}{\rho^\gamma} \quad (3.1.17)$$

Many SPH codes use this quantity as the central evolved variable in addition to density. This is called *Density-Entropy SPH*. The evolution of  $A$  is related to the dissipation of internal energy through

$$\frac{dA}{dt} = \frac{\gamma - 1}{\rho^{\gamma-1}} \left( \frac{du}{dt} - \frac{p}{\rho^2} \frac{d\rho}{dt} \right) = \frac{\gamma - 1}{\rho^{\gamma-1}} \frac{du}{dt} \Big|_{diss} \quad (3.1.18)$$

The thermal energy can be calculated via  $A$  as

$$u = \frac{A}{\gamma - 1} \rho^{\gamma-1} \quad (3.1.19)$$

So much for a derivation via the Lagrangian. The next step is, to show how we can in general write equations as SPH discretizations. Furthermore we will see, that a formal derivation will lead to the same results as the Lagrangian approach.

### 3.2 Interpolation formulas

A formal SPH derivation usually starts with the identity

$$A(\vec{x}) = \int d\vec{x}' A(\vec{x}') \delta(\vec{x} - \vec{x}') \quad (3.2.1)$$

for a general variable  $A$ . Approximating the delta function by the kernel and neglecting terms of order  $h^2$  and higher, we get

$$\begin{aligned} A(\vec{x}) &\approx \int d\vec{x}' \rho(\vec{x}') \frac{A(\vec{x}')}{\rho(\vec{x}')} W(\vec{x} - \vec{x}', h) \\ &\approx \sum_{j=1}^{N_{ngb}} m_j \frac{A_j}{\rho_j} W(\vec{x} - \vec{x}_j, h) \end{aligned} \quad (3.2.2)$$

Plugging in for example the density, this reproduces exactly our heuristic approximation from equation 3.1.4. An estimation for the derivative can be simply made, by taking the derivative of the integral formula before going to the discrete formulation:

$$\nabla A_i = \sum_{j=1}^{N_{ngb}} m_j \frac{A_j}{\rho_j} \nabla W_{ij} \quad (3.2.3)$$

If  $A$  is a vector quantity all vector derivatives can be taken analogously by pulling the operator into the sum and applying it onto the kernel.

Using these estimation formulas onto the equations we derived in the last section, we can reproduce the usual equations of hydrodynamics which proves the quality of the estimates. Taking for example the time derivative of the density estimate 3.1.4 we get the continuity equation:

$$\begin{aligned} \frac{d\rho_i}{dt} &= \sum_{j=1}^{N_{ngb}} m_b (\vec{v}_i - \vec{v}_j) \cdot \nabla_i W_{ij} \\ &= \vec{v}_i \cdot \sum_{j=1}^{N_{ngb}} \frac{m_j}{\rho_j} \rho_j \nabla_i W_{ij} - \sum_{j=1}^{N_{ngb}} \frac{m_j}{\rho_j} (\rho_j \vec{v}_j) \cdot \nabla_i W_{ij} \\ &\approx \vec{v}_i \cdot \nabla \rho - \nabla \cdot (\rho \vec{v})_i = -\rho_i (\nabla \cdot \vec{v})_i \end{aligned} \quad (3.2.4)$$

From equation 3.1.11 we get directly

$$\frac{du}{dt} = -\frac{p}{\rho} \nabla \cdot \vec{v} \quad (3.2.5)$$

Coming from kernel interpolation theory it is clear, that these interpolation formulas are not unique. Performing a more detailed Taylor expansion for some generic value  $A$ , we see directly that we can improve the estimation by subtracting the first error term:

$$\nabla A \approx \sum_{j=1}^{N_{ngb}} m_j \frac{A_j - A_i}{\rho_j} \nabla_i W_{ij} \approx \nabla A - A \nabla 1 \quad (3.2.6)$$

Another approach is to use an inverse product rule before discretizing:

$$\nabla A = \frac{1}{\rho} [\nabla (\rho A) - A \nabla \rho] \approx \frac{1}{\rho_i} \sum_{j=1}^{N_{ngb}} m_j (A_j - A_i) \nabla_i W_{ij} \quad (3.2.7)$$

which can be further improved by using for example:

$$\nabla A = \rho \left[ \frac{A}{\rho^2} \nabla \rho + \nabla \frac{A}{\rho} \right] \approx \rho_i \sum_{j=1}^{N_{ngb}} m_j \left( \frac{A_i}{\rho_i^2} + \frac{A_j}{\rho_j^2} \right) \nabla_i W_{ij} \quad (3.2.8)$$

Please note, that the last two estimates have totally different symmetry properties with respect to exchange of particles  $i$  and  $j$  in each summand. Which interpolation formula has to be taken for the best outcome therefore differs in each case.

These formulas can be further generalized by replacing  $\rho$  with a general variable  $\Phi$ . Similar estimates can be derived again for vector quantities.

Without going more into detail, we want to finish this section with estimates for second derivatives. Here we can follow a similar approach by starting with a simple estimate and subtracting the first error term for improvement:

$$\Delta A \approx \sum_{j=1}^{N_{ngb}} m_j \frac{A_j}{\rho_j} \nabla_i^2 W_{ij} \quad (3.2.9)$$

$$\Delta A \approx \sum_{j=1}^{N_{ngb}} \frac{m_j}{\rho_j} (A_j - A_i) \nabla_i^2 W_{ij} \quad (3.2.10)$$

Similar formulas apply again for vector quantities.

Of course there is much more to say about SPH. However it is not the scope of this thesis, to give a complete overview but only provide the reader with basic knowledge to understand they way of SPH discretizations. This is necessary to understand our derivation of the conduction equation later in section 4 For further reading the interested reader may consult for example the review article of [Price, 2012].

Having all these tools we will now analyse the quality of these estimates for different choices of kernels in the next subsection. We will not show a full error estimate for different interpolation formulas but rather come back to the choice of a suitable kernel and discuss general errors coming from this choice. Detailed error estimations can be found for example in [Price, 2012].

### 3.3 Different kernels and their characteristics

At the beginning of section 3 we defined a kernel function and imposed several restrictions to the choice of this function. A first idea was to use a function similar to a Gaussian, but with a compact support.

One possible choice to fulfil these needs are the so called B-splines, which can be generated by the Fourier transform<sup>17</sup>

$$M_n(x, h) = \frac{1}{2\pi} \int_{-\infty}^{\infty} dk \left[ \frac{\sin(kh/2)}{kh/2} \right]^2 \cos(kx) \quad (3.3.1)$$

$M_n$  has the nice property, that it approximates the Gaussian with increasing accuracy for bigger  $n$ . Since it has continuous derivatives up to the order  $n - 2$  only choices with  $n \geq 4$  are interesting for a kernel function. The easiest choice for  $n = 4$  is called the cubic spline (since it is a polynomial of order 3). Using this function we can define the kernel as

$$W(|\vec{x}_{ij}|, h) = \frac{1}{h^d} w(q) \quad (3.3.2)$$

$$w(q) = \sigma \begin{cases} \frac{1}{4}(2-q)^3 - (1-q)^3 & 0 \leq q < 1 \\ \frac{1}{4}(2-q)^3 & 1 \leq q < 2 \\ 0 & q \geq 2 \end{cases} \quad (3.3.3)$$

with  $q := |\vec{x}_{ij}|/h$  and a normalisation constant  $\sigma$  which is defined (depending on the dimensionality of the problem) as

$$\sigma = \begin{cases} \frac{2}{3} & \text{in } 1D \\ \frac{10}{7\pi} & \text{in } 2D \\ \frac{1}{\pi} & \text{in } 3D \end{cases} \quad (3.3.4)$$

Although the cubic spline can be calculated very fast due to it's simply polynomial representation it is however only a crude approximation to the Gaussian and as we will show does not perform very good. Sticking to B-splines usually the

---

<sup>17</sup>Taken from [Price, 2012].

quintic spline is taken for more accurate, though computationally more expensive, estimates:

$$w(q) = \sigma \begin{cases} (3-q)^5 - 6(2-q)^5 + 15(1-q)^5 & 0 \leq q < 1 \\ (3-q)^5 - 6(2-q)^5 & 1 \leq q < 2 \\ (3-q)^5 & 2 \leq q < 3 \\ 0 & q \geq 3 \end{cases} \quad (3.3.5)$$

with

$$\sigma = \begin{cases} \frac{1}{24} & \text{in } 1D \\ \frac{96}{1199\pi} & \text{in } 2D \\ \frac{1}{20\pi} & \text{in } 3D \end{cases} \quad (3.3.6)$$

Before we come to more advanced kernel functions, let us at first show what we mean by more accurate results comparing those two splines. We start with computing an estimate (with the most basic formula we derived earlier) for a generic quantity of particle  $i$  and expand the interpolation formula into a Taylor series:

$$A_i \approx \sum_{j=1}^{N_{ngb}} \frac{m_j \cdot A_j}{\rho_j} W_{ij} \quad (3.3.7)$$

$$= A_i \sum_{j=1}^{N_{ngb}} \frac{m_j}{\rho_j} W_{ij} + \nabla A_i \cdot \sum_{j=1}^{N_{ngb}} \frac{m_j}{\rho_j} (\vec{x}_j - \vec{x}_i) W_{ij} + \mathcal{O}(h^2) \quad (3.3.8)$$

For this estimate to be exact up to second order in  $h$ , we get two conditions:

$$\sum_{j=1}^{N_{ngb}} \frac{m_j}{\rho_j} W_{ij} \approx 1 \quad (3.3.9)$$

$$\sum_{j=1}^{N_{ngb}} \frac{m_j}{\rho_j} (\vec{x}_j - \vec{x}_i) W_{ij} \approx 0 \quad (3.3.10)$$

The second conditions is relatively easy fulfilled for reasonably symmetric particle distributions while the first condition depends strongly on the ratio of the smooth-

ing length  $h$  to the particle spacing  $dx$ . For most of the possible values, already the cubic kernel gives a good agreement for this condition. For comparison see the black lines in figure 13 and 14, where we have plotted equation 3.3.9 for the cubic and quintic kernel for the one dimensional case.

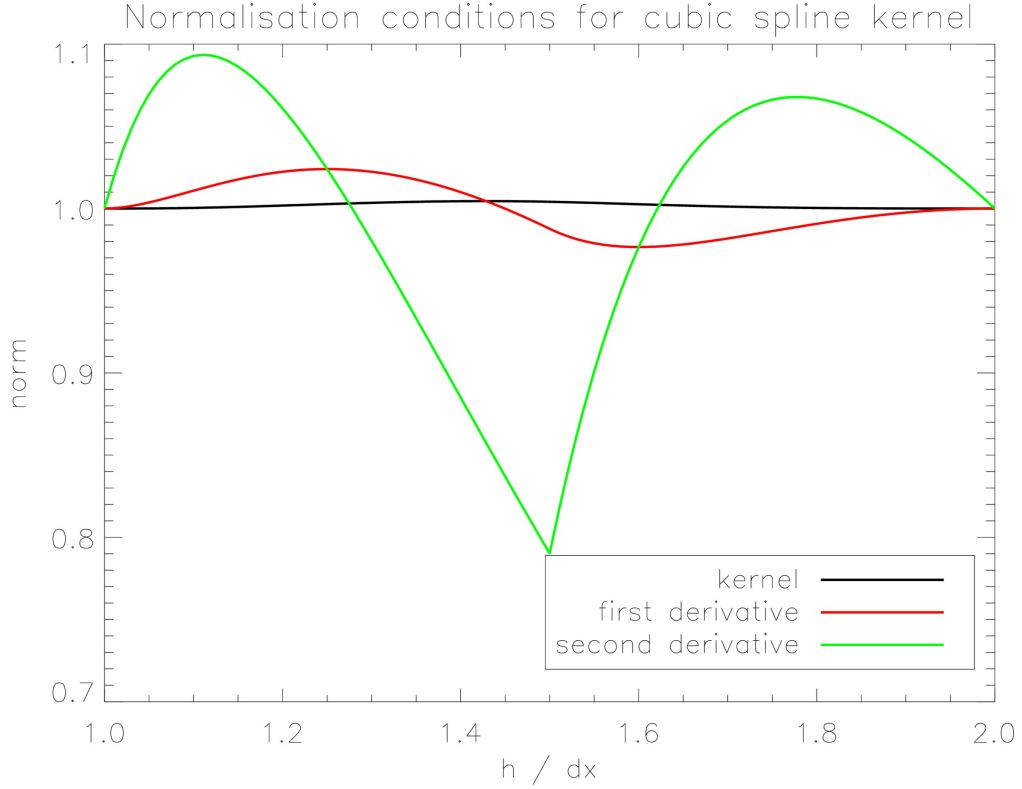


Figure 13: Plotted are the normalisation conditions for the cubic spline kernel in one dimension against the smoothing length over the particle spacing. The kernel normalisation (eq. 3.3.9) is very good fulfilled, the first derivative (eq. 3.3.11) is still ok, but the errors for the second derivative (eq. 3.3.12) are very high.

However we do not only have these kind of conditions for the kernel itself, but also for estimates of the first and second derivatives. For a full derivation see again [Price, 2012].

The red lines in the plots represent the normalisation condition for the first derivative:

$$\sum_{j=1}^{N_{ngb}} \frac{m_j}{\rho_j} (\vec{x}_j - \vec{x}_i)^\alpha \nabla_i^\beta W_{ij} \approx \delta^{\alpha\beta} \quad (3.3.11)$$

with  $\alpha$  and  $\beta$  being the components of the vectors. Here we can already see, that the quintic kernel performs in general much better for estimates of first derivatives. The errors on this condition are already roughly a factor 10 smaller, which makes the quintic kernel a way better choice for estimating derivatives.

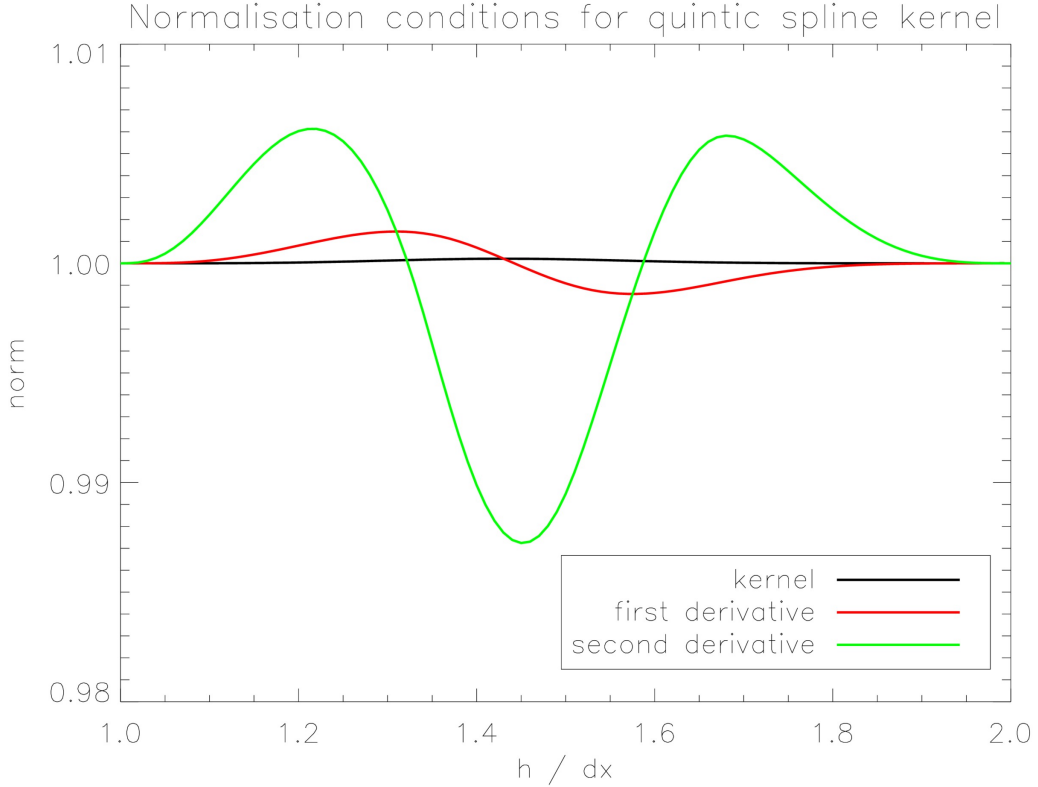


Figure 14: Plotted are the normalisation conditions for the quintic spline kernel in one dimension against the smoothing length over the particle spacing. The normalisation condition for the kernel itself (eq. 3.3.9) and its first derivative (eq. 3.3.11) are very good. The second derivative (eq. 3.3.12) still shows visible errors, but much less than for the cubic spline kernel.

We see a similar behaviour for the normalisation condition for second derivatives, however we still get quite big errors even for the quintic kernel here. The corresponding equation is given as

$$\frac{1}{2} \sum_{j=1}^{N_{ngb}} \frac{m_j}{\rho_j} (\vec{x}_j - \vec{x}_i)^\alpha (\vec{x}_j - \vec{x}_i)^\beta \Delta W_{ij} \approx \delta^{\alpha\beta} \quad (3.3.12)$$

Further analysis shows, that this large error comes basically from the second derivative of the kernel. Therefore we will need to be very careful, when writing down the conduction equation for SPH since it contains second derivatives!

As a choice for more advanced kernels we want to mention the Wendland functions. They exist also in different orders with varying computational cost and accuracy. Especially interesting is the Wendland c6 function which is defined as a kernel by [Dehnen and Aly, 2012] as

$$w(q) = \sigma \begin{cases} (1 - q)^7 \cdot (1 + 7q + 19q^2 + 21q^3) & 0 \leq q < 1 \\ 0 & q \geq 1 \end{cases} \quad (3.3.13)$$

with  $\sigma = 55/32$  for a 1D problem and

$$w(q) = \sigma \begin{cases} (1 - q)^8 \cdot (1 + 8q + 25q^2 + 32q^3) & 0 \leq q < 1 \\ 0 & q \geq 1 \end{cases} \quad (3.3.14)$$

with  $\sigma = 78/7\pi$  for 2D and  $\sigma = 1365/64\pi$  for 3D. Please note, that this definition is for a support radius of  $1h$ . The implementation in GADGET is however done for a support radius of  $3.3h$  to allow about 295 neighbours to be taken into account. For comparison the cubic kernel uses about 64 and the quintic 216 neighbours in GADGET. As one can see, this kernel is a polynomial of much higher order and therefore more expensive to calculate. We checked the same three criteria also for this Wendland c6 kernel (see figure 15) and see, that this function performs a bit worse than the quintic kernel for big particle spacings and a bit better for small ones. The results are in general comparable.

The real advantage of the Wendland functions lies in another property which we have not discussed so far. If one wants to increase the quality of an estimate one would probably intuitively just increase the amount of neighbours taken into account for each interpolation. With the spline kernels this will however result very fast in the clumping of particles. The Wendland kernels however can support much higher neighbour numbers without producing a paring instability. For a much more detailed view on this problem, kernel comparisons in general and further refinement we refer to [Dehnen and Aly, 2012].

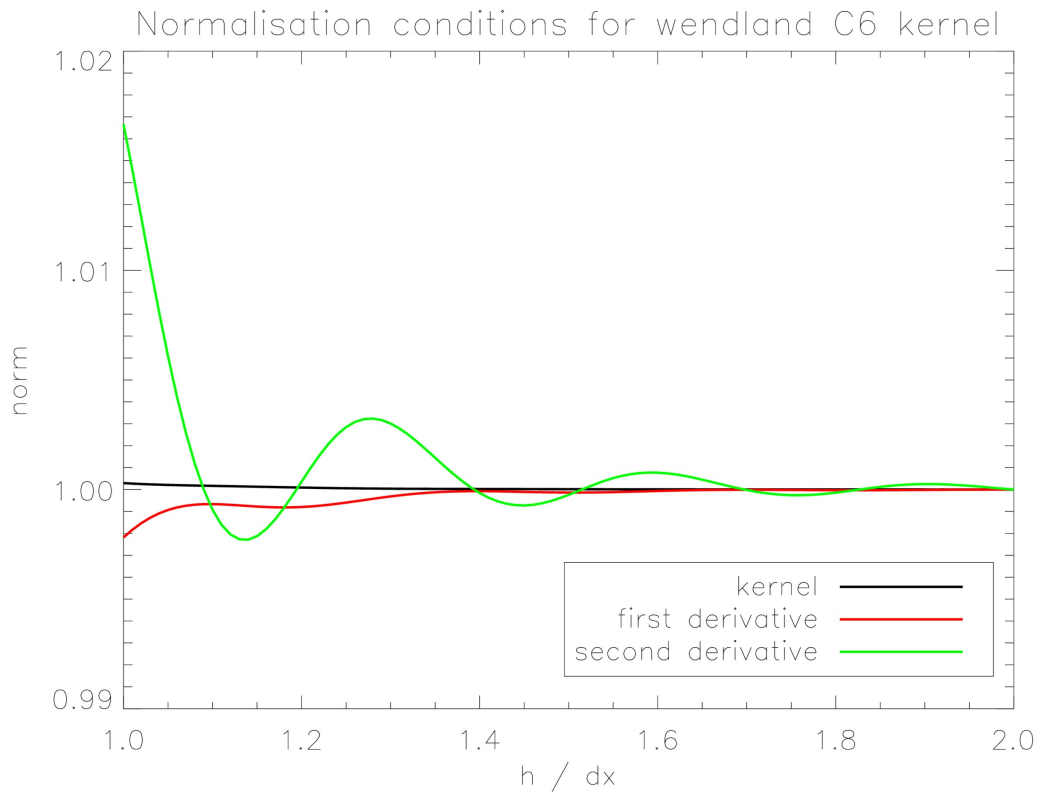


Figure 15: Plotted are the normalisation conditions for the Wendland c6 kernel in one dimension against the smoothing length over the particle spacing. The results are comparable to the quintic spline kernel (fig. 14). Only the errors for the second derivative change a lot depending on the value for  $h/dx$ .

### 3.4 MHD equations in SPH

After talking about basic hydrodynamics in SPH and basic kernel properties we still have to mention how to implement magnetic fields into the code in order to come to anisotropic thermal conduction later. Again we will just give a short motivation for the basic equations. Details can be found as general derivation in [Price, 2012] or specific for GADGET in [Dolag and Stasyszyn, 2009].

So let us start with one of the basic equations we have to consider: the induction equation, which tells us the evolution of a magnetic field. We combine Ampere's law, Faraday's law with the Lorentz force to get an equation which contains only the magnetic field and the velocity field:

$$\partial_t \vec{B} = \nabla \times \left[ \vec{v} \times \vec{B} - \eta \nabla \times \vec{B} \right] \quad (3.4.1)$$

with the electric resistance  $\eta$ . We will consider only ideal MHD, so the second term drops out. We can rewrite the first term and apply  $\nabla \cdot \vec{B} = 0$  to get

$$\partial_t \vec{B} = \left( \vec{B} \cdot \nabla \right) \vec{v} - \vec{B} (\nabla \cdot \vec{v}) - (\vec{v} \cdot \nabla) \vec{B} \quad (3.4.2)$$

Combining the left hand side with the last term of the right hand side we get the total time derivative of the magnetic field as

$$\frac{d}{dt} \vec{B} = \left( \vec{B} \cdot \nabla \right) \vec{v} - \vec{B} (\nabla \cdot \vec{v}) \quad (3.4.3)$$

Using the continuity equation we can write this in the even simpler form

$$\frac{d}{dt} \left( \frac{\vec{B}}{\rho} \right) = \left( \frac{\vec{B}}{\rho} \cdot \nabla \right) \vec{v} \quad (3.4.4)$$

Applying the discretization with subtraction of the first error term we get

$$\frac{d}{dt} \left( \frac{\vec{B}_i}{\rho_i} \right) = - \sum_{j=1}^{N_{ngb}} m_j (\vec{v}_i - \vec{v}_j) \frac{\vec{B}_i}{\rho_i^2} \cdot \nabla_i W_{ij} \quad (3.4.5)$$

In addition to this new equation we have to modify our Lagrangian and add a magnetic pressure term. Consequently equation 3.1.6 transforms to:

$$L = \sum_j m_j \left( \frac{1}{2} v_j^2 - u_j - \frac{1}{2\mu_0} \frac{B_j^2}{\rho_j} \right) \quad (3.4.6)$$

Unfortunately we can not write the magnetic field nor it's time derivative directly in terms of particle coordinates, so we can not simply write down the Euler Lagrange equations like we did before in the pure hydrodynamics case. So we have to take the more general approach of using the variational principle in order to derive the equation of motion. We will not present the calculations in full detail here and simply give the result:<sup>18</sup>

$$\frac{dv_i^\alpha}{dt} = \sum_{j=1}^{N_{ngb}} m_j \left[ \frac{S_i^{\alpha\beta}}{\rho_i^2} + \frac{S_j^{\alpha\beta}}{\rho_j^2} \right] \nabla_i^\beta W_{ij} \quad (3.4.7)$$

with the MHD stress tensor

$$S^{\alpha\beta} = - \left( p + \frac{1}{2\mu_0} B^2 \right) \delta^{\alpha\beta} + \frac{1}{\mu_0} B^\alpha B^\beta \quad (3.4.8)$$

which contains the hydrodynamical pressure as well as the magnetic pressure. More details on the derivation and further calculations can again been found in [Price, 2012].

Regarding conservation laws we see, that the total linear momentum is still conserved, however not the total angular momentum. Additional we can see, that the total energy is conserved when we write down the modified Hamiltonian and derive the energy evolution like we did before for the hydrodynamics case.

With these comments we want to finish our very brief overview concerning the derivation of the SPMHD<sup>19</sup> equations, which is certainly not complete. There is a lot more to say about MHD in particular and SPH in general and we refer again to the mentioned papers and further references for all the details.

---

<sup>18</sup>Written component wise and using the Einstein sum convention.

<sup>19</sup>Smoothed Particle MagnetoHydroDynamics

Now we have all the tools we need to approach the question, which will be the topic for the next section: How to implement thermal conduction in an SPH code like GADGET?

## 4 Thermal conduction in GADGET

Knowing the basics of how to transform physics into SPH equations, we can now start describing an implementation for thermal conduction. We will start with the original implementation of isotropic conduction in GADGET. After that, we present different approaches to treat anisotropic thermal conduction which we will evaluate using some test cases afterwards.

### 4.1 Isotropic implementation

To discretize the conduction equation for the isotropic case we follow [Cleary and Monaghan, 1999] and mostly [Jubelgas et al., 2004]. Using the heat flux we described earlier (equation 2.1.1), we infer a change of internal energy over time as

$$\frac{du}{dt} = -\frac{1}{\rho}\nabla \cdot \vec{Q} = \frac{1}{\rho}\nabla \cdot (\kappa\nabla T) \quad (4.1.1)$$

At first we rewrite the right hand side using the inverse product rule of differentiation:

$$\kappa\nabla T = \nabla(\kappa T) - T\nabla\kappa = \frac{1}{2}[\nabla(\kappa T) - T\nabla\kappa + \kappa\nabla T] \quad (4.1.2)$$

Applying the divergence onto this term, we get

$$\nabla \cdot (\kappa\nabla T) = \frac{1}{2}[\Delta(\kappa T) - T\Delta\kappa + \kappa\Delta T] \quad (4.1.3)$$

This formulation has the advantage, that we can directly discretize the laplacians for which we need only one SPH loop instead of two for gradient and then divergence. This increases not only the code's speed, but can also provide us with an opportunity to reduce errors in the estimation. As already mentioned in section 3.3, the estimates of second derivatives in SPH are not very exact. This is mostly due to the involved second derivatives of the kernel. To avoid that problem we use another estimate for the laplacian, which involves only first kernel derivatives. To derive this for some arbitrary variable  $Y$ , we start with the Taylor expansion around  $\vec{x}_i$  using  $\vec{x}_{ij} = \vec{x}_j - \vec{x}_i$ :

$$Y(\vec{x}_j) - Y(\vec{x}_i) = \nabla Y|_{\vec{x}_i} \cdot \vec{x}_{ij} + \frac{1}{2} \sum_{\alpha\beta} \frac{\partial^2 Y}{\partial x_\alpha \partial x_\beta} \Big|_{\vec{x}_i} \cdot (\vec{x}_{ij})_\alpha (\vec{x}_{ij})_\beta + \mathcal{O}((\vec{x}_{ij})^3) \quad (4.1.4)$$

We multiply both sides by  $\frac{\vec{x}_{ij} \cdot \nabla_i W_{ij}}{|\vec{x}_{ij}|^2}$  and integrate the equation over  $d^3 \vec{x}_j$ . Inspecting the different parts above individually, we can easily see, that the following holds for the first order error term:

$$\int \vec{x}_{ij} \frac{\vec{x}_{ij} \cdot \nabla_i W_{ij}}{|\vec{x}_{ij}|^2} d^3 \vec{x}_j = 0 \quad (4.1.5)$$

Since the kernel derivative is antisymmetric<sup>20</sup> the integrand in total is antisymmetric and the integration results in zero. Please note, that we are not talking about symmetry in exchange of particles  $i$  and  $j$  here, but rather about having an even integrand with the respect to the integration variable  $\vec{x}_j$ .

The second order error term on the right side results in

$$\int (\vec{x}_{ij})_\alpha (\vec{x}_{ij})_\beta \frac{\vec{x}_{ij} \cdot \nabla_i W_{ij}}{|\vec{x}_{ij}|^2} d^3 \vec{x}_j = \delta_{\alpha\beta} \quad (4.1.6)$$

For  $\alpha \neq \beta$  we get an expression similar to 4.1.5 and the integral vanishes.

However for  $\alpha = \beta$  we have a total symmetric integrand and therefore the integral is unequal to zero. Due to normalisation of the kernel, the integral will then simply give one.<sup>21</sup>

Combining these findings we get

$$\int (Y(\vec{x}_j) - Y(\vec{x}_i)) \frac{\vec{x}_{ij} \cdot \nabla_i W_{ij}}{|\vec{x}_{ij}|^2} d^3 \vec{x}_j = \frac{1}{2} \frac{\partial^2 Y}{\partial x_\alpha \partial x_\beta} \Big|_{\vec{x}_i} \delta_{\alpha\beta} \quad (4.1.7)$$

The right hand side is equal to  $2 \cdot \Delta Y|_{\vec{x}_i}$ . Therefore we can infer an estimate for the laplacian:

$$\Delta Y_i = 2 \sum_j \frac{m_j}{\rho_j} (Y_j - Y_i) \frac{\vec{x}_{ij} \cdot \nabla_i W_{ij}}{|\vec{x}_{ij}|^2} \quad (4.1.8)$$

Plugging this estimate in eq. 4.1.1 and using eq. 4.1.3, we get the energy change for the  $i$ -th particle as

$$\frac{du_i}{dt} = -\frac{1}{\rho_i} \sum_j \frac{m_j}{\rho_j} [\kappa_j T_j - \kappa_i T_i - T_i (\kappa_j - \kappa_i) + \kappa_i (T_j - T_i)] \frac{\vec{x}_{ij} \cdot \nabla_i W_{ij}}{|\vec{x}_{ij}|^2} \quad (4.1.9)$$

<sup>20</sup>The kernel itself is symmetric, for details see all the kernel properties in section 3.1.

<sup>21</sup>This can also be shown by partial integration. In section 4.2.3 we will present similar but slightly more complicated calculations which also contain such integrals. Detailed calculation for some of them can be found in appendix B.

The expression in brackets can be rewritten to  $(\kappa_i + \kappa_j)(T_j - T_i)$ . According to [Cleary and Monaghan, 1999] we further replace

$$\frac{\kappa_i + \kappa_j}{2} \rightarrow \kappa_{ij} = \frac{2\kappa_i\kappa_j}{\kappa_i + \kappa_j} \quad (4.1.10)$$

to ensure a correct behaviour of our implementation at discontinuities of  $\kappa$  between two particles due to symmetrization. Using the relation between entropy<sup>22</sup> and internal energy / temperature with an isochoric approximation:

$$A = \frac{\gamma - 1}{\rho^{\gamma-1}} \cdot u \quad (4.1.11)$$

$$T = \frac{\mu}{k_B} \cdot A \cdot \rho^{\gamma-1} \quad (4.1.12)$$

we get

$$\frac{dA_i}{dt} = \frac{2\mu}{k_B} \frac{\gamma - 1}{\rho_i^{\gamma-1}} \sum_j \frac{m_j \kappa_{ij}}{\rho_i \rho_j} (A_j \rho_j^{\gamma-1} - A_i \rho_i^{\gamma-1}) \frac{\vec{x}_{ij} \cdot \nabla_i W_{ij}}{|\vec{x}_{ij}|^2} \quad (4.1.13)$$

Since we use an entropy-density formulation of SPH it makes sense to write every equation here in terms of  $A$ . In the code we use the specific internal energy during the calculations and update the particles' entropies afterwards. We can do that, since thermal conduction is located in an isolated module which therefore only deals with internal energies.

To actually apply this equation for a given timestep we can use basically any arbitrary integrator. In the original paper, [Jubelgas et al., 2004] used a simple finite difference scheme:

$$m_i u'_i = m_i u_i + \Delta t_i \sum_j E_{ij} \quad (4.1.14)$$

with the pairwise energy exchange  $E_{ij}$  which is the right hand side of equation 4.1.13 times  $m_i$ . Since this formulation can violate energy conservation when indi-

---

<sup>22</sup>Please note that  $A$  is only a function of the entropy per unit mass  $s$  which we introduced in section 3.1

vidual timesteps for all particles are used, we need to rewrite this to for example:

$$m_i u'_i = m_i u_i + \frac{1}{2} \sum_{jk} \Delta t_j (\delta_{ij} - \delta_{jk}) E_{jk} \quad (4.1.15)$$

In practise one loops over the active particles and applies an energy change to both interacting particles, where the other is also active or not. This recovers energy conservation explicitly during each exchange.

Additionally it is useful, to take a symmetrized version of the kernel gradient, to combine the smoothing lengths of both particles,  $i$  and  $j$ .

[Jubelgas et al., 2004] further find, that the accuracy of their results for a basic test problem increases, if they use a smoothed version of the entropy instead of the entropy itself, calculated in a previous SPH loop. They get the best results with a mixed formulation, using a smoothed version of  $A_j$  and a non smoothed  $A_i$ .

This can however be avoided for a more complex integration scheme. In the current implementation of isotropic thermal conduction in GADGET we use the conjugate gradient method implemented by Springel et al. like it is described by [Petkova and Springel, 2009] for radiative transfer. Since the conjugate gradient is an implicit scheme, it needs internally an additional SPH loop, but in return we gain arbitrarily accurate results<sup>23</sup> depending on the iteration count without having to smooth the variables beforehand. A description of the conjugate gradient method and how to apply it to equation 4.1.13 can be found in appendix A.

We want to mention one more remark on this. In the iteration of the conjugate gradient we will evolve the internal energy. Depending on what we use to determine  $\kappa$ , a constant value (for test cases) or something proportional to Spitzer conduction, we need to write out the formula for the coefficient and perform the derivation of the conjugate gradient formalism in appendix A using this additional temperature dependence. In the current code this is however neglected,  $\kappa$  is assumed to be fixed during the iterations of one timestep. As we will see from the later test cases in section 4.3, this will not change the quality of the estimate visibly.

---

<sup>23</sup>Except of numerical noise and errors due to Taylor approximations of course.

## 4.2 Anisotropic implementation

The next step is, to implement our thoughts on anisotropic thermal conduction from section 2.2 into the existing SPH code. In table 1 we show an overview over the different methods, we discuss in the next three subsections.

Identifier	Description
<b>1a</b>	Change conduction coefficient. Precalculate energy gradient once.
<b>1b</b>	Change conduction coefficient. Recalculate energy gradient in each iteration step.
<b>2</b>	Distinguish between conduction along and perpendicular the magnetic field. Split up calculation of energy gradient and divergence.
<b>3a</b>	Distinguish between conduction along and perpendicular the magnetic field. Fully anisotropic approximation in one SPH loop.
<b>3b</b>	Distinguish between conduction along and perpendicular the magnetic field. Isotropised approximation in one SPH loop.

Table 1: Summing up the different implementation ideas with identifier numbers for further reference. The numbers are according to the subsection 4.2.X where we derive and discuss this approach.

### 4.2.1 An easy idea

As we discussed earlier, we want to have a (nearly) fully suppressed conduction perpendicular to magnetic field lines but an unchanged transport along the field. The simplest approach to embed these constraints (with full suppression) in an equation is, to weight the conduction coefficient in equation 4.1.1 with the angle between temperature gradient and magnetic field:

$$\kappa' = \kappa \cdot \frac{\nabla T \cdot \hat{B}}{|\nabla T|} = \kappa \cdot \cos \theta \quad (4.2.1)$$

with the normalized magnetic field vector  $\hat{B} = \frac{\vec{B}}{|\vec{B}|}$ .

This modification can be easily implemented into equation 4.1.13 by pre-calculating the temperature gradient in a different SPH loop and applying the corresponding

factors onto each  $\kappa$ . Instead of the temperature gradient we can also use the gradient of the specific internal energy, since we wanted to evolve  $u$  anyway. Using equation 4.1.11 we get the energy gradient by calculating

$$\nabla u_i = \frac{1}{(\gamma - 1) \rho_i} \sum_j m_j (A_j \rho_j^{\gamma-1} - A_i \rho_i^{\gamma-1}) \nabla_i W_{ij} \quad (4.2.2)$$

To be absolutely correct we need to recalculate  $\kappa$  in each iteration step of the solver. Since this would have a drastic impact on the simulation's performance,<sup>24</sup> we will compare the outcome with the one of calculating the gradient only once per timestep and particle.

As we have already argued in section 4.1 neglecting the temperature dependence of  $\kappa$  itself will not have any impact on our results. Since we do not expect the temperature gradient to change its direction drastically during the iterations, we will not get a bigger error in  $\kappa'$  than we already have in  $\kappa$  and can therefore neglect this recalculation. We will prove this expectation in our first test case in section 4.3.1.

#### 4.2.2 The split up approach

The second and more complicated approach we want to discuss, is, to take equation 4.2.1 and also change the direction of the heat flux to be along the magnetic field lines. One reason to consider this more complicated approach is, that this allows us to additionally implement, how strong we want to suppress the heat flow perpendicular to the magnetic field related to the field's strength.

So we distinguish between a  $\kappa$  parallel the magnetic field and one perpendicular to it. Writing the perpendicular part as the total flux minus the parallel part, the conduction equation looks like

$$\frac{du}{dt} = \frac{1}{\rho} \nabla \cdot \left[ \kappa_{\parallel} \left( \hat{B} \cdot \nabla T \right) \hat{B} + \kappa_{\perp} \left( \nabla T - \left( \hat{B} \cdot \nabla T \right) \hat{B} \right) \right] \quad (4.2.3)$$

<sup>24</sup>Because we would need always an additional loop in between.

If the two conduction constants were the same, we would consistently regain the isotropic implementation discussed in section 4.1.

As next step we reshuffle the terms and write the equation as one part parallel to the magnetic field lines and one part parallel to the temperature gradient:

$$\frac{du}{dt} = \frac{1}{\rho} \nabla \cdot \left[ (\kappa_{\parallel} - \kappa_{\perp}) \left( \hat{B} \cdot \nabla T \right) \hat{B} + \kappa_{\perp} \nabla T \right] \quad (4.2.4)$$

From section 2.2 we know that for cluster simulations  $\kappa_{\perp} \ll \kappa_{\parallel}$ . Therefore we can approximate the first part with  $\kappa_{\parallel} - \kappa_{\perp} \approx \kappa_{\parallel}$ .

However we can not simply neglect the second term along the temperature gradient. Comparing the absolute values of the two terms we see, that except of  $\kappa_{\perp} \ll \kappa_{\parallel}$  the first term contains a  $\cos\theta$  which can be arbitrarily small and make both terms comparable in magnitude. If the magnetic field and the energy gradient are almost totally perpendicular, the second term dominates the equation and can therefore not be neglected. It has to be seen later, if this case is important for our cluster simulations or not.

Now we can transform equation 4.2.4 to SPH formalism. The second term can be handled similar to the isotropic implementation just with a different coefficient. For details how to handle this part we refer back to section 4.1. Here we discuss only on the first term.

We want to consider the case of splitting up the equation into two SPH loops: One for the temperature gradient and one for the divergence. [Jubelgas et al., 2004] already argued, that this resembles still an effective second derivative of the kernel which gives rise to a big error, as we have already shown earlier. However we have seen that we get much better results with modern kernels, even for second derivatives and therefore want to test, if this approach can lead now to good results.

To conserve energy explicitly we need a divergence estimate which is antisymmetric under exchange of  $i$  and  $j$ . We have already shown such interpolation formulas in section 3.2.

Consider a simplified version of our equation for some general value  $\vec{A}$ :  $\frac{\nabla \cdot \vec{A}}{\rho_i}$ . Then we can estimate

$$\frac{\nabla \cdot \vec{A}}{\rho_i} = \sum_j m_j \left( \frac{\vec{A}_i}{\rho_i^2} + \frac{\vec{A}_j}{\rho_j^2} \right) \cdot \nabla_i W_{ij} \quad (4.2.5)$$

To check the explicit conservation we have a look at the impact of particle  $j$  on particle  $i$  and vice versa. Please note, that we need to multiply eq. 4.2.5 with  $m_i$ , since we need to conserve the real internal energy and not specific internal energy.

$$\Delta_{j \rightarrow i} = m_i m_j \left( \frac{\vec{A}_i}{\rho_i^2} + \frac{\vec{A}_j}{\rho_j^2} \right) \cdot \nabla_i W_{ij} \quad (4.2.6)$$

Using  $\nabla_i W_{ij} = -\nabla_j W_{ij}$  we get<sup>25</sup>

$$\Delta_{j \rightarrow i} + \Delta_{i \rightarrow j} = 0 \quad (4.2.7)$$

Using this estimate for the divergence, the first part of equation 4.2.4 looks like the following:

$$\left. \frac{du_i}{dt} \right|_{1st} = \sum_j m_j \left[ \frac{\left( \kappa_B \cos \theta |\nabla T| \hat{B} \right)_j}{\rho_j^2} + \frac{\left( \kappa_B \cos \theta |\nabla T| \hat{B} \right)_i}{\rho_i^2} \right] \cdot \nabla_i W_{ij} \quad (4.2.8)$$

With equation 4.1.11 we can again rewrite the equation to internal energies instead of temperatures. Therefore we get

$$\left. \frac{du_i}{dt} \right|_{1st} = \sum_j m_j \left[ \kappa_{Bj} \hat{B}_j + \kappa_{Bi} \hat{B}_i \right] \cdot \nabla_i W_{ij} \quad (4.2.9)$$

With the coefficient

$$\kappa_B = (\kappa_{\parallel} - \kappa_{\perp}) \cdot \frac{\mu (\gamma - 1) \cos \theta |\nabla u|}{k_b \rho^2} \quad (4.2.10)$$

<sup>25</sup>For further details please review section 3.1.

Also substituting

$$\kappa_T = \kappa_{\perp} \cdot \frac{\mu(\gamma - 1)}{k_b} \quad (4.2.11)$$

we get in total

$$\frac{du_i}{dt} = \sum_j m_j \left[ \left( \kappa_{Bj} \hat{B}_j + \kappa_{Bi} \hat{B}_i \right) + \frac{2\kappa_{Tij}}{\rho_i \rho_j} (u_j - u_i) \frac{\vec{x}_{ij}}{|\vec{x}_{ij}|^2} \right] \cdot \nabla_i W_{ij} \quad (4.2.12)$$

At this point we can think again about the calculation of the energy gradient. Assuming the first term dominates, then the energy gradient has basically replaced the energy as variable of the integration algorithm. Therefore we need to recalculate it in each iteration step, for the algorithm to converge correctly. Since the recalculation needs fully updated energies (or rather entropies) for each particle, we need an additional SPH loop to calculate the energy gradient of each particle in each iteration step of the conjugate gradient solver. In contrast to the last subsection we do not have any choice here.

Additionally we want to ensure, that energy flows in the correct direction. From a thermodynamical point of view (2nd law of thermodynamics), this is a very crucial constraint. Considering our approach, we can easily see, that this will not always be fulfilled. So let us start with an easy example, just to check whether we have the correct overall sign in equation 4.2.12: We consider the effect of a particle  $\mathbf{j}$  on another particle  $\mathbf{i}$ . We choose

- $x_j > x_i, \quad y_j = y_i, \quad z_j = z_i$
- $u_j > u_i$  but overall  $\nabla u_j \approx \nabla u_i \propto \hat{e}_x$
- $\hat{B}_j = \hat{B}_i$  and such, that  $\nabla u \cdot \hat{B} > 0$
- $m_j = m_i$  and  $\rho_j = \rho_i$

A schematic drawing is shown in figure 16.

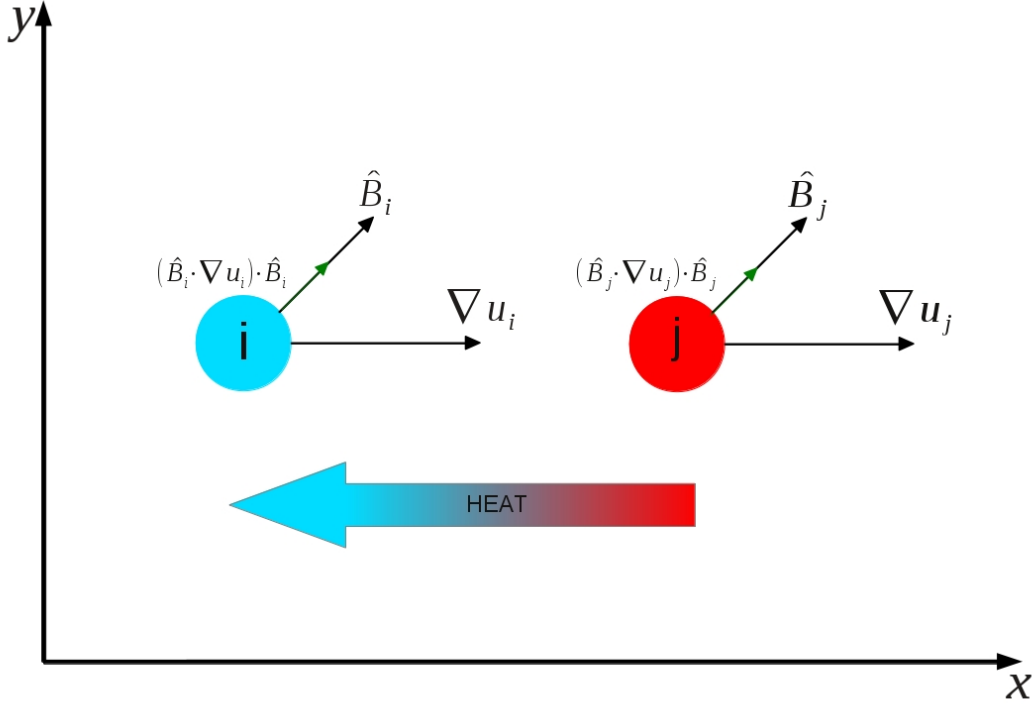


Figure 16: Schematic drawing to check, if heat flows in the right direction for a test setup.

With this setup we want heat to be flowing from particle **j** onto particle **i**. The brackets in equation 4.2.12 are in total positive. The first summand is positive as we can check by plugging in our preconditions. The second summand his also positive, since [Jubelgas et al., 2004] already checked that for the isotropic implementation. We can write the kernel derivative as

$$\nabla_i W_{ij} \propto -\frac{\partial w(r)}{\partial r} \hat{x}_{ij} \quad (4.2.13)$$

Which points in positive x-direction since the kernel as a function of distance  $r$  is per definition monotonically decreasing and  $\hat{x}_{ij} = \hat{e}_x$ . Therefore in total heat flows in the left direction in this case. This is consistent with energy transport from  $j$  to  $i$ .

One can however easily think of particle setups which will result in a non-physical heat flow. We want to provide two examples here:

- Consider a setup, where two particles have a similar temperature gradient (just not opposite ones!) but also have the same internal energy. One would expect a heat flow to occur in this scenario because of the existence of a gradient, but not between the two particles with same temperature. Nevertheless our implementation will exactly produce this kind of transport of energy. One can argue, that this effect won't be a problem, since this just mimics the transport of energy from the real heat source via all particles in between.
- Another setup is also interesting, not depending on the internal energy of two particles but simply on the component of conduction perpendicular to the temperature gradient. We naturally get such components, since we aligned the heat flow with the magnetic field. This heat flow is therefore per construction not correct from a macroscopic point of view. However, as we will see in our test in the next subsection, looking at the whole picture this should not be much of a problem.

Similar to what has been done in [Sharma and Hammett, 2007] we also thought about implementing an additional limiter, to preserve the monotonicity of our heat flux. The idea is basically to suppress any non physical transport similar to one of the above mentioned cases.

However this flux limiter only worsens (or even totally dismantles) our results in all of the test cases. Therefore we run all of our simulations without this kind of artificial limiter.

### 4.2.3 A fully consistent numerical scheme

We want to develop one further scheme which uses the same approach as the one before, but needs only one SPH loop for all calculations, just like isotropic conduction does. So we will start over with equation 4.2.4 and try to find a scheme which covers all the mixed derivatives we encounter in this formula. Please note that we will again neglect any temperature dependence of  $\kappa$ , as we did in the previous sections.

For the following derivation we will follow the example of [Petkova and Springel, 2009], who derived an SPH scheme for a similar diffusion equation regarding radiative transfer.

To avoid confusion we want to mention the following conventions again:

- Latin indices like  $i, j$  and  $k$  denote particles.
- Greek indices like  $\alpha, \beta$  denote components of tensors.
- Bold variables like  $\mathbf{A}$  are tensors.

Before we start discretizing the modified conduction equation, we have to find a better estimate for mixed second derivatives. The derivation will at first be similar to what we showed for isotropic conduction in section 4.1, but will get more complicated since we also need mixed derivatives now. For the sake of a better understanding we will repeat the necessary parts, even if we already provided parts of these calculations earlier.

At first we take an arbitrary quantity  $Q$  at  $\vec{x}_j$ , which we expand around  $\vec{x}_i$ :

$$Q(\vec{x}_j) \approx Q(\vec{x}_i) + \nabla Q|_{\vec{x}_i} \vec{x}_{ij} + \frac{1}{2} \sum_{\alpha\beta} \frac{\partial^2 Q}{\partial x_\alpha \partial x_\beta} \Big|_{\vec{x}_i} (\vec{x}_{ij})_\alpha (\vec{x}_{ij})_\beta + \mathcal{O}((\vec{x}_{ij})^3) \quad (4.2.14)$$

Then we multiply both sides by  $\frac{(\vec{x}_{ij})_\gamma}{|\vec{x}_{ij}|^2} \frac{\partial W_{ij}}{\partial (\vec{x}_i)_\delta}$  and integrate over  $\int d^3 \vec{x}_j$ .

We will further need the kernel derivative expressed as

$$\frac{\partial W_{ij}}{\partial (\vec{x}_i)_\delta} = -W'_{ij} \frac{(\vec{x}_{ij})_\delta}{|\vec{x}_{ij}|} \quad (4.2.15)$$

which we have used already before (see equation 3.1.14).

Let us at first have a look at the first order error term. We can immediately see, that we get

$$\int d^3 \vec{x}_j \frac{(\vec{x}_{ij})_\alpha (\vec{x}_{ij})_\gamma}{|\vec{x}_{ij}|^2} \cdot \left( -\frac{(\vec{x}_{ij})_\delta}{|\vec{x}_{ij}|} W'_{ij} \right) = 0 \quad (4.2.16)$$

since for all possibilities of  $\alpha, \gamma$  and  $\delta$  there will always be at least one component, where the integral vanishes because of an antisymmetric integrand. All these indices go from 1 to 3, so there will be always one component where we have an

odd amount of  $\vec{x}_{ij}$ . The denominator and  $W'_{ij}$  are even with respect to  $\vec{x}_j$ , so the integral in total will vanish.

The next step is to calculate the integrals of the second order error term which we substitute as

$$T_{\alpha\beta\gamma\delta} = \int d^3\vec{x}_j \frac{(\vec{x}_{ij})_\alpha (\vec{x}_{ij})_\beta (\vec{x}_{ij})_\gamma (\vec{x}_{ij})_\delta}{|\vec{x}_{ij}|^3} \cdot W'_{ij} \quad (4.2.17)$$

Here we have to distinguish between several cases. Calculations show that

$$T_{\alpha\beta\gamma\delta} = \begin{cases} -\frac{3}{5} & \text{if } \alpha = \beta = \gamma = \delta \\ -\frac{1}{5} & \text{if } \alpha = \beta \neq \gamma = \delta \\ -\frac{1}{5} & \text{if } \alpha = \gamma \neq \beta = \delta \\ -\frac{1}{5} & \text{if } \alpha = \delta \neq \beta = \gamma \\ 0 & \text{else} \end{cases} \quad (4.2.18)$$

So basically  $T$  is only non zero, if we have two pairs of indices. These calculations are shown in detail in appendix B.

Plugging all this back into the modified equation 4.2.14, we get:

$$2 \int d^3\vec{x}_j \frac{Q(\vec{x}_j) - Q(\vec{x}_i)}{|\vec{x}_{ij}|^2} (\vec{x}_{ij})_\gamma \frac{\partial W_{ij}}{\partial (\vec{x}_i)_\delta} = - \sum_{\alpha\beta} T_{\alpha\beta\gamma\delta} \frac{\partial^2 Q}{\partial x_\alpha \partial x_\beta} \Big|_{\vec{x}_i} \quad (4.2.19)$$

To infer a general behaviour we have a look at this equation for example with  $\gamma = \delta = 0$ :

$$Term_{0,0} = \frac{3}{5} \frac{\partial^2 Q}{\partial^2 x_0} \Big|_{\vec{x}_i} + \frac{1}{5} \frac{\partial^2 Q}{\partial^2 x_1} \Big|_{\vec{x}_i} + \frac{1}{5} \frac{\partial^2 Q}{\partial^2 x_2} \Big|_{\vec{x}_i} \quad (4.2.20)$$

Since we want to infer an approximation for second order mixed derivatives of  $Q$ , we will have to linearly combine terms for different choices of  $\alpha$  and  $\beta$ . We see, that we get

$$\frac{\partial^2 Q}{\partial x_0^2} = 2 \cdot Term_{0,0} - \frac{1}{2} \cdot Term_{1,1} - \frac{1}{2} \cdot Term_{2,2} \quad (4.2.21)$$

and cyclic permutation for other second derivatives. We can get a similar formula for mixed derivatives. Consider for example

$$Term_{0,1} = -\frac{1}{5} \frac{\partial^2 Q}{\partial x_0 \partial x_1} \Big|_{\vec{x}_i} - \frac{1}{5} \frac{\partial^2 Q}{\partial x_1 \partial x_0} \Big|_{\vec{x}_i} \quad (4.2.22)$$

We could of course put those two parts together, but it is better to keep them separated to explicitly indicate the symmetry. This makes things easier, when we try to reassemble everything.

From this example we get directly

$$\frac{\partial^2 Q}{\partial x_0 \partial x_1} = \frac{5}{4} \cdot Term_{0,1} + \frac{5}{4} \cdot Term_{1,0} \quad (4.2.23)$$

and cyclic permutations.

Now we have approximations for all types of second order differentiations. To make the following calculations easier, it is extremely required, that we find a formulation which contains all our results so far. Luckily we will never need isolated derivatives of some scalar  $Q$  but we will always have a double sum over tensor components and second derivatives (of the tensor or another scalar). We can then plug everything together for those two cases:

$$\sum_{\alpha,\beta} \frac{\partial^2 (Q_i)_{\alpha\beta}}{\partial x_\alpha \partial x_\beta} = 2 \int d^3 \vec{x}_j \frac{\vec{x}_{ij}^\top [\tilde{\mathbf{Q}}_j - \tilde{\mathbf{Q}}_i] \nabla_i W_{ij}}{|\vec{x}_{ij}|^2} \quad (4.2.24)$$

$$\sum_{\alpha,\beta} (Q_i)_{\alpha\beta} \frac{\partial^2 T_i}{\partial x_\alpha \partial x_\beta} = 2 \int d^3 \vec{x}_j \frac{\vec{x}_{ij}^\top \tilde{\mathbf{Q}}_i [T_j - T_i] \nabla_i W_{ij}}{|\vec{x}_{ij}|^2} \quad (4.2.25)$$

with the substituted tensor

$$\tilde{\mathbf{Q}} = \frac{5}{2} \mathbf{Q} - \frac{1}{2} \text{tr}(\mathbf{Q}) \mathbf{1} \quad (4.2.26)$$

This is a very compact and neat formulation. Since we already mentioned in the beginning, that parts of the derivation up to this point are similar to what has been done by [Jubelgas et al., 2004], we can use their outcome to check this formula for consistency.

Consider  $\mathbf{Q}$  to be a scalar, or better  $\mathbf{Q} = Q \cdot \mathbf{1}$ . Then we get

$$\tilde{\mathbf{Q}} = \frac{5}{2} \cdot Q \cdot \mathbf{1} - \frac{1}{2} \cdot Q \cdot 3 \cdot \mathbf{1} = Q \cdot \mathbf{1} \quad (4.2.27)$$

Plugging this into either of the estimates above, we get exactly the result we obtained earlier for the isotropic implementation, where we only needed non-mixed second derivatives: equation 4.1.7.

Before we further analyse the properties of these approximation formulas, let us at first review our basic equation and show, how we can apply them.

Similar to our last approach we consider only the part of equation 4.2.4 parallel to the magnetic field. The term conducting along the temperature gradient can be handled like in the isotropic case.

We start with writing the equation component wise:

$$\left. \frac{du}{dt} \right|_{1st} = \frac{1}{\rho} \nabla \cdot \left[ (\kappa_{\parallel} - \kappa_{\perp}) \left( \hat{B} \cdot \nabla T \right) \hat{B} \right] \quad (4.2.28)$$

$$= \frac{1}{\rho} \sum_{\alpha, \beta} \frac{\partial}{\partial x_{\alpha}} \left[ (\kappa_{\parallel} - \kappa_{\perp}) \hat{B}_{\alpha} \hat{B}_{\beta} \frac{\partial}{\partial x_{\beta}} T \right] \quad (4.2.29)$$

Furthermore we define the components of a tensor  $\mathbf{A}$  as

$$A_{\alpha\beta} := (\kappa_{\parallel} - \kappa_{\perp}) \hat{B}_{\alpha} \hat{B}_{\beta} \quad (4.2.30)$$

to make the following calculations easier understandable.

The next step is to write the equation only in terms of mixed second derivatives.

Again we have done something similar for the isotropic case.

$$\left. \frac{du}{dt} \right|_{1st} = \frac{1}{2\rho} \sum_{\alpha, \beta} \left( \frac{\partial^2 A_{\alpha\beta} T}{\partial x_{\alpha} \partial x_{\beta}} - T \frac{\partial^2 A_{\alpha\beta}}{\partial x_{\alpha} \partial x_{\beta}} + A_{\alpha\beta} \frac{\partial^2 T}{\partial x_{\alpha} \partial x_{\beta}} \right) \quad (4.2.31)$$

This equality can be shown most simply by a backwards calculation:

$$\frac{\partial^2 A_{\alpha\beta} T}{\partial x_{\alpha} \partial x_{\beta}} = T \frac{\partial^2 A_{\alpha\beta}}{\partial x_{\alpha} \partial x_{\beta}} + A_{\alpha\beta} \frac{\partial^2 T}{\partial x_{\alpha} \partial x_{\beta}} + \frac{\partial A_{\alpha\beta}}{\partial x_{\alpha}} \frac{\partial T}{\partial x_{\beta}} + \frac{\partial A_{\alpha\beta}}{\partial x_{\beta}} \frac{\partial T}{\partial x_{\alpha}} \quad (4.2.32)$$

Using

$$\sum_{\alpha,\beta} \frac{\partial A_{\alpha\beta}}{\partial x_\alpha} \frac{\partial T}{\partial x_\beta} + \frac{\partial A_{\alpha\beta}}{\partial x_\beta} \frac{\partial T}{\partial x_\alpha} = 2 \sum_{\alpha,\beta} \frac{\partial A_{\alpha\beta}}{\partial x_\alpha} \frac{\partial T}{\partial x_\beta} \quad (4.2.33)$$

and plugging all back in, we get

$$\left. \frac{du}{dt} \right|_{1st} = \frac{1}{2\rho} \sum_{\alpha,\beta} \left( 2A_{\alpha\beta} \frac{\partial^2 T}{\partial x_\alpha \partial x_\beta} + 2 \frac{\partial A_{\alpha\beta}}{\partial x_\alpha} \frac{\partial T}{\partial x_\beta} \right) \quad (4.2.34)$$

which is equal to equation 4.2.29.

Now we can use the equations 4.2.24 and 4.2.25 to estimate the second derivatives in equation 4.2.31. We get for particle  $i$ :

$$\left. \frac{du_i}{dt} \right|_{1st} = \frac{1}{\rho_i} \int d^3 \vec{x}_j \vec{x}_{ij}^\top \left[ \frac{\left( \tilde{\mathbf{A}}_j T_j - \tilde{\mathbf{A}}_i T_i \right) - T_i \left( \tilde{\mathbf{A}}_j - \tilde{\mathbf{A}}_i \right) + \tilde{\mathbf{A}}_i (T_j - T_i)}{|\vec{x}_{ij}|^2} \right] \nabla_i W_{ij} \quad (4.2.35)$$

Re factoring the terms leads us to a more compact expression:

$$\left. \frac{du_i}{dt} \right|_{1st} = \frac{1}{\rho_i} \int d^3 \vec{x}_j \vec{x}_{ij}^\top \left[ \frac{\left( \tilde{\mathbf{A}}_j + \tilde{\mathbf{A}}_i \right) (T_j - T_i)}{|\vec{x}_{ij}|^2} \right] \nabla_i W_{ij} \quad (4.2.36)$$

Now we discretize the integral and get

$$\left. \frac{du_i}{dt} \right|_{1st} = \frac{1}{\rho_i} \sum_{j=1}^{N_{ngb}} \frac{m_j}{\rho_j} \cdot \vec{x}_{ij}^\top \left[ \frac{\left( \tilde{\mathbf{A}}_j + \tilde{\mathbf{A}}_i \right) (T_j - T_i)}{|\vec{x}_{ij}|^2} \right] \nabla_i W_{ij} \quad (4.2.37)$$

Except of unit conversion we have now reached our goal, to write down one equation with one single SPH loop to discretize our anisotropic formulation of conduction. We can see one good property of this equation right away:

We managed to get again the term  $(T_j - T_i)$ , like we did in the isotropic conduction case. This ensures, that we have only conduction if the temperatures of two particles differ (not like with our last approach, where this was not clear at first sight). Furthermore we have seen, that this type of equation can be used well with

the conjugate gradient solver.

Still we could have a problem with this approximation formula. To ensure the correct flow of internal energy from hot to cold (according to the second law of thermodynamics) we need the tensor  $(\tilde{\mathbf{A}}_j + \tilde{\mathbf{A}}_i)$  to be positive definite. However from the definition of a variable with tilde (equation 4.2.26) we see immediately, that this tensor does not necessarily fulfil this condition. For a very anisotropic setup we can get heat flow in the wrong direction. Furthermore this could lead to numerical instabilities, which has to be further investigated later. To fix this we have basically two options, which are both artificial and therefore make the approximation overall slightly worse

1. Implement a limiter in the code, which checks for non physical heat flows and removes them, like already mentioned in subsection 4.2.2.
2. Change the tensor to a more isotropic version, which is always positive definite.

Since it is more straight forward and computationally way cheaper, we decided to further follow [Petkova and Springel, 2009] and go for the second option:

We want to add an isotropic component to the anisotropic tensor in order to prevent temperature flowing from cold to warm regions. We already have a pure isotropic component, which was however proportional to  $\kappa_{\perp}$  and it is not clear, if this is already sufficient to do the job. We will therefore not forget about this *fully anisotropic* formulation, but further investigate it's behaviour in our tests and cluster simulations in the next sections.

Adding another isotropic component we could replace the tensor  $\tilde{\mathbf{A}}$  by

$$\tilde{\mathbf{A}} \rightarrow \alpha \tilde{\mathbf{A}} + \frac{1}{3} (1 - \alpha) \text{tr}(\tilde{\mathbf{A}}) \mathbf{1} \quad (4.2.38)$$

Calculations show, that we need to set  $\alpha \geq \frac{2}{5}$ . We use the minimum value to hopefully prevent a big error in the estimate. This leads to  $\tilde{\mathbf{A}} \rightarrow \mathbf{A}$ , which is computationally very good, since we have to compute  $\mathbf{A}$  anyway for each particle. We call this formulation the *isotropised* discretization.

It can be easily seen, that  $\mathbf{A}$  itself is positive definite. Diagonalising leads to

$$\text{diag}(\mathbf{A}) \propto \text{diag}(\hat{B} \otimes \hat{B}) = \begin{pmatrix} 0 & 0 & 0 \\ 0 & 0 & 0 \\ 0 & 0 & 1 \end{pmatrix} \quad (4.2.39)$$

How to write these two equations in order to use the conjugate gradient solver can again be found in appendix A.

Now that we have calculated two more ways of discretizing anisotropic conduction, let us sum up our options in the next subsection before we come to test simulations of the different implementations.

#### 4.2.4 Summary and expectations for the different schemes

In the last few subsections we presented several approaches to implement anisotropic thermal conduction into the SPH code.

At first we had the idea to modify only the conduction coefficient and weight it with the projection of the temperature gradient onto the magnetic field. We have seen that it could make a difference to recalculate the temperature gradient in each iteration step, or just leave it fixed during the integration per timestep. With this easy approach we could only fully suppress conduction perpendicular to the magnetic field all the time, regardless of the magnetic field strength.

After that we argued, that perhaps this would not be sufficient, but that we had to perform conduction directly along the magnetic field lines. So we split up the conduction into parts parallel and perpendicular to the magnetic field and assigned different coefficients to both parts. Rewriting the equation we got one term along the magnetic field lines and one isotropic term along the temperature gradient. We mentioned, that usually only the part along the magnetic field lines should play a role, although we left the possibility open to include a suppressed perpendicular part.

Identifier	Description	Pros	Cons
<b>1a</b>	Change conduction coefficient. Precalculate energy gradient once.	Uses existing code without big changes.	Allows only full suppression.
<b>1b</b>	Change conduction coefficient. Recalculate energy gradient in each iteration step.	Uses existing code without big changes.	Allows only full suppression.
<b>2</b>	Distinguish between conduction along and perpendicular the magnetic field. Split up calculation of energy gradient and divergence.	Allows a suppression factor.	Computationally expensive and possibly wrong heatflux.
<b>3a</b>	Distinguish between conduction along and perpendicular the magnetic field. Fully anisotropic approximation in one SPH loop.	Allows a suppression factor.	Possibly wrong heatflux.
<b>3b</b>	Distinguish between conduction along and perpendicular the magnetic field. Isotropised approximation in one SPH loop.	Allows a suppression factor.	Slightly wrong solutions.

Table 2: Summing up the different implementation ideas with identifier numbers for further reference. The numbers are according to the subsection 4.2.X where we described this approach. Added advantages and disadvantages for each entry.

For this approach we presented two basic approximations: In the first one we split up the gradient and the divergence part and formulated the equations using two SPH loops.

Afterwards we derived a new formulation which needs only one loop and discussed the properties of the solution. We added a modified version which ensures heat flow in the right direction to the cost of estimation errors.

A short list including identifiers for each approach, which we will need for reference in the next section) can be found in table 2.

In section 4.1 we mentioned the modification account for a saturation effect when the density of the gas is very low. We should be able to combine this modification with all of our implementation types without running into problems. The modification combines the mean free path with the typical length scale of the temperature gradient. Perhaps we need to further combine this with the gyro radius, however this is not clear at the moment.

The next step is, to take the implementations of our various approaches in GADGET and try to judge, which ones are usable for cosmological simulations by performing several tests. Furthermore we use this opportunity to analyse and discuss the properties, advantages and disadvantages of each implementation type.

### 4.3 Tests for the code

As a next step we carry out several tests for the different implementations, we presented earlier. We use rather simple test cases, where we can verify the behaviour analytically, before we apply it to a real problem like galaxy clusters.

For all of the following tests we use initial conditions with "glass like" particle distributions<sup>26</sup> and therefore rule out any alignment effects which can arise by the definition of a grid. Even if the test setups could be done in one or two dimensions, we carry out the whole simulation in 3D to make sure everything works for our final cosmological simulations later on.

We always use the Wendland c6 kernel, for details please see section 3.3.

Furthermore we run the simulations with gas only and disable any accelerations on the SPH particles which would come from self-gravity or the hydrodynamics equation of motion. With this approach we ensure, that hydrodynamical properties like the density and the internal energy are computed correctly in their respective SPH loops, but we evolve only the conduction equation to thoroughly test the behaviour of our implementations.

In the next subsections we will always start by describing a test case and trying to derive an analytic solution. As we will point out later, we will only be able to derive an analytic solution for a constant conduction coefficient, which we will enforce in our code for the test problems.

Afterwards we show the behaviour of the existing code (i.e. isotropic conduction) with a reference run and further present our results with the new anisotropic approaches. We will indicate the different implementations by using the identifiers we defined in table 2. For each test we will always show the different results at the same simulation time, to be able to properly compare the outcomes.

#### 4.3.1 Temperature step problem

For the beginning we reproduce the first test from [Jubelgas et al., 2004] and modify it, so that we can apply it to the new anisotropic conduction implementation.

The basic idea is, to set up a temperature step and let the particles exchange heat energy. We fix the particle positions (and also the magnetic field, which we will

---

<sup>26</sup>A random field of particles but with a fixed density.

later add) and therefore only evolve the conduction equation.<sup>27</sup> Also considering a fixed conduction coefficient instead of Spitzer conduction we can pull the  $\kappa$  out of the divergence and get

$$\frac{du}{dt} = \frac{\kappa}{\rho} \Delta T \quad (4.3.1)$$

This simplified conduction equation can be solved analytically (depending on the initial conditions) and therefore we can then compare this analytical solution to the results of the code. We assume a gas with constant density and use

$$u = c_v \cdot T \quad (4.3.2)$$

with the specific heat capacity  $c_v$ . We can rewrite equation 4.3.1 to

$$\frac{du}{dt} = \alpha \cdot \Delta u \quad (4.3.3)$$

with the so called thermal diffusivity  $\alpha = \frac{\kappa}{c_v \rho} = \text{const.}$   $\alpha$  is simply a diffusion coefficient, as we have already discussed them in the analytic part before (section 2.2).

For this temperature step problem it is sufficient to solve the equation in only one dimension. The more general solution can be easily inferred later and basically differs only in some factors. We follow [Jubelgas et al., 2004] and [Landau and Lifschitz, 2007], to solve this equation through Fourier transformation:

$$u(t, x) = \int_{-\infty}^{\infty} u_k(t) e^{ikx} \frac{dk}{2\pi} \quad (4.3.4)$$

$$u_k(t) = \int_{-\infty}^{\infty} u(t, x) e^{-ikx} dx \quad (4.3.5)$$

Equation 4.3.3 expressed in Fourier space looks like

$$\frac{du_k(t)}{dt} = -\alpha k^2 u_k(t) \quad (4.3.6)$$

---

<sup>27</sup>For this we can use the NO\_ACCEL switch in GADGET.

with the simple solution

$$u_k(t) = u_{k0} e^{-\alpha k^2 t} \quad (4.3.7)$$

Using  $u(t = 0, x) = u_0(x)$  we can express the unknown coefficient in terms of the initial condition in real space:

$$u_{k0} = \int_{-\infty}^{\infty} u_0(x') e^{-ikx'} dx' \quad (4.3.8)$$

Now we plug this result back into the reverse Fourier transformation (eq. 4.3.4) and get

$$u(t, x) = \int_{-\infty}^{\infty} dx' \int_{-\infty}^{\infty} \frac{dk}{2\pi} u_0(x') e^{-\alpha k^2 t} e^{ik(x-x')} \quad (4.3.9)$$

At first we perform the integration over  $dk$ . For this we rewrite the exponentials completing the square to bring them into the typical gaussian form, which is easy to integrate. So we use:

$$-\alpha k^2 t - ik(x - x') = -\alpha t \left[ k - \frac{i(x - x')}{2\alpha t} \right]^2 - \frac{(x - x')^2}{4\alpha t} \quad (4.3.10)$$

and perform the Gaussian integral like

$$\int_{-\infty}^{\infty} dy e^{-\beta y^2} = \sqrt{\frac{\pi}{\beta}} \quad (4.3.11)$$

Therefore we get in total

$$u(t, x) = \frac{1}{2\sqrt{\pi\alpha t}} \int_{-\infty}^{\infty} dx' u_0(x') \exp\left(-\frac{(x - x')^2}{4\alpha t}\right) \quad (4.3.12)$$

So far concerning the general solution, at this point we need to plug in the specific initial conditions of our problem. For the temperature step they can be defined as

$$u_0(x') = \begin{cases} u_0 - \frac{\Delta u}{2} & \text{for } x' < x_m \\ u_0 + \frac{\Delta u}{2} & \text{for } x' > x_m \end{cases} \quad (4.3.13)$$

with  $x_m$  being the position of the temperature step.

Plugging this into equation 4.3.12 we get two integrals to perform:

$$u(t, x) = \frac{1}{2\sqrt{\alpha\pi t}} \left[ \int_{-\infty}^{x_m} dx' \left( u_0 - \frac{\Delta u}{2} \right) e^{-y^2} + \int_{x_m}^{\infty} dx' \left( u_0 + \frac{\Delta u}{2} \right) e^{-y^2} \right] \quad (4.3.14)$$

where we substituted  $y \equiv y(x') = \sqrt{\frac{(x-x')^2}{4\alpha t}}$ .

We split this expression into two parts: One which is multiplied by  $u_0$  and one which is multiplied by  $\Delta u/2$ . The  $u_0$  term can be simply integrated using again the formula for the Gaussian integral (equation 4.3.11), which results in  $2\sqrt{\alpha\pi t} \cdot u_0$ . For a little consistence check consider  $\Delta u = 0$  then we get  $u(t, x) = u_0$ , which is what we would expect for a isothermal region without any other effects than thermal conduction.

The second term, with  $\Delta u$ , is a bit more sophisticated to integrate. The first step is to extend the boundaries of second integral to the total space and plug in again the solution for the total integral:

$$\begin{aligned} \int_{x_m}^{\infty} dx' \frac{\Delta u}{2} e^{-y^2} &= \int_{-\infty}^{\infty} dx' \frac{\Delta u}{2} e^{-y^2} - \int_{-\infty}^{x_m} dx' \frac{\Delta u}{2} e^{-y^2} \\ &= \sqrt{\alpha\pi t} \Delta u - \int_{-\infty}^{x_m} dx' \frac{\Delta u}{2} e^{-y^2} \end{aligned} \quad (4.3.15)$$

The remaining integral is the same as in 4.3.14, therefore we get

$$u|_{2nd} = \frac{\Delta u}{2} \cdot \left[ 1 - \frac{1}{\sqrt{\alpha\pi t}} \int_{-\infty}^{x_m} dx' e^{-y^2} \right] \quad (4.3.16)$$

To be able to perform the final integration we again split the integral up into two integrals starting at zero and rewrite them to integrals over  $dy$ . We get

$$u|_{2nd} = \frac{\Delta u}{2} \left[ 1 - \frac{2}{\sqrt{\pi}} \left( \int_0^{\infty} dy e^{-y^2} - \int_0^{\frac{x-x_m}{2\sqrt{\alpha t}}} dy e^{-y^2} \right) \right] \quad (4.3.17)$$

Now the remaining integrals both fulfil exactly the definition for the error function<sup>28</sup> and we can write the expression as:

$$u|_{2nd} = \frac{\Delta u}{2} \left[ 1 - \left( \operatorname{erf}(\infty) - \operatorname{erf}\left(\frac{x - x_m}{2\sqrt{\alpha t}}\right) \right) \right] = \operatorname{erf}\left(\frac{x - x_m}{2\sqrt{\alpha t}}\right) \quad (4.3.18)$$

using  $\operatorname{erf}(\infty) = 1$ . Now we can plug this all back in into equation 4.3.14 and we get as result

$$u(t, x) = u_0 + \frac{\Delta u}{2} \cdot \operatorname{erf}\left(\frac{x - x_m}{2\sqrt{\alpha t}}\right) \quad (4.3.19)$$

Now we cross check our calculations with the existing code of isotropic conduction. The result is shown in fig. 17. The outcome from the SPH particles (black points) matches very well with the analytic solution we just derived (green line). Therefore we see, that the existing implementation works even for sudden temperature jumps.

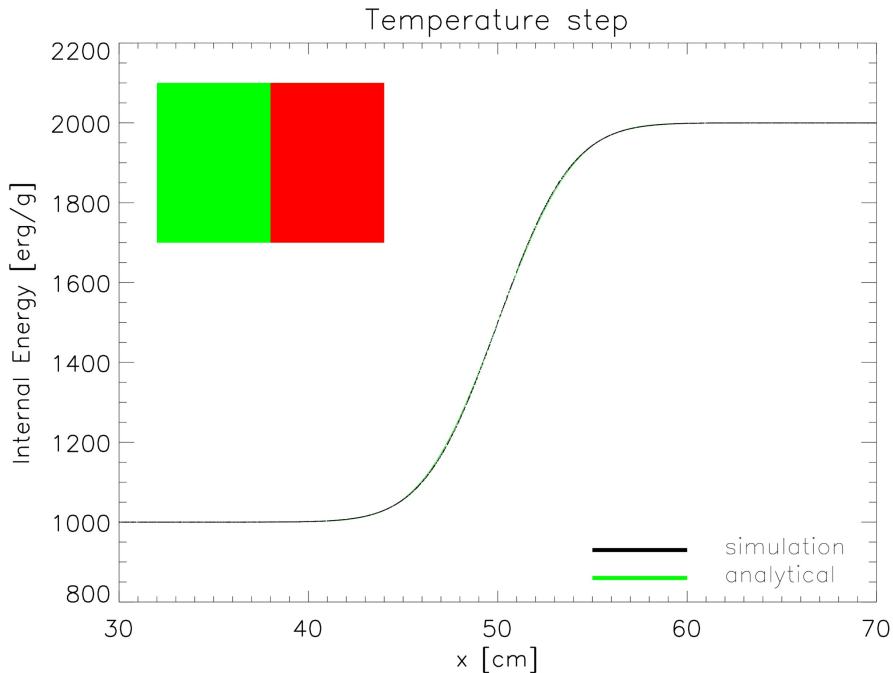


Figure 17: First conduction test: One dimensional temperature step without magnetic field. The green line is the analytical solution (eq. 4.3.19), the black dots are SPH particles. Both solutions match up very well.

<sup>28</sup>For details please see [Bronstein et al., 2008].

The next step is, to include a magnetic field into the test problem to check the new anisotropic implementation. For simplicity we keep the magnetic field fixed.<sup>29</sup> We introduce a homogeneous field in direction  $(x, y, z) = \left(\frac{1}{\sqrt{2}}, \frac{1}{\sqrt{2}}, 0\right)$ . Hence we get an angle of  $45^\circ$  between the  $\vec{B}$ -field and the energy gradient, which is in our setup parallel to the x-axis.

With this we can check each of the implementations we discussed in section 4.2. At first we start with the easiest approach, only modifying the conduction coefficient by a factor of  $\cos \angle \left(\vec{B}, \nabla T\right)$ . As can be seen in figure 18 the simulation reproduces very well the result we derived in analytically. This is not surprising, since the modified code is basically only the isotropic implementation plus the projection factor and we have already seen in figure 17, that the old code produces good results for this particular test problem. We get this result already for the implementation **1a**, so we can assume recalculating the energy gradient in each step produces the same result. Nevertheless we carried out this simulation, too, to successfully verify our expectations.

Now we test our second, more complex approach, where we split up the calculations into two SPH loops, as described in section 4.2.2. Now we can compare the simulation to the analytic solution with an effective  $\kappa' = \kappa \cdot \cos^2 \angle \left(\vec{B}, \nabla T\right)$ . One cosine comes from the scalar product in the construction of this approach, the other one is the de-projection from the magnetic field onto the temperature gradient. As can be seen in figure 19, this requires some more discussion.

We see immediately, that this implementation does not ideally reproduce the analytic solution. Especially near the discontinuity in the middle, the result is far off. Exactly in the middle of the plot we see, that the particles have still more or less their initial temperature, hence nearly no conduction was carried out. Or rather conduction was carried out, but all the energy transports cancelled each other out. At least the net energy transport follows the second law of thermodynamics everywhere. A bit away from the temperature step, we see that our simulations reproduce the solution again pretty well. Around  $x = 47$  and  $x = 53$  there are

---

<sup>29</sup>Otherwise we would not be able to write down an analytic solution so easily.

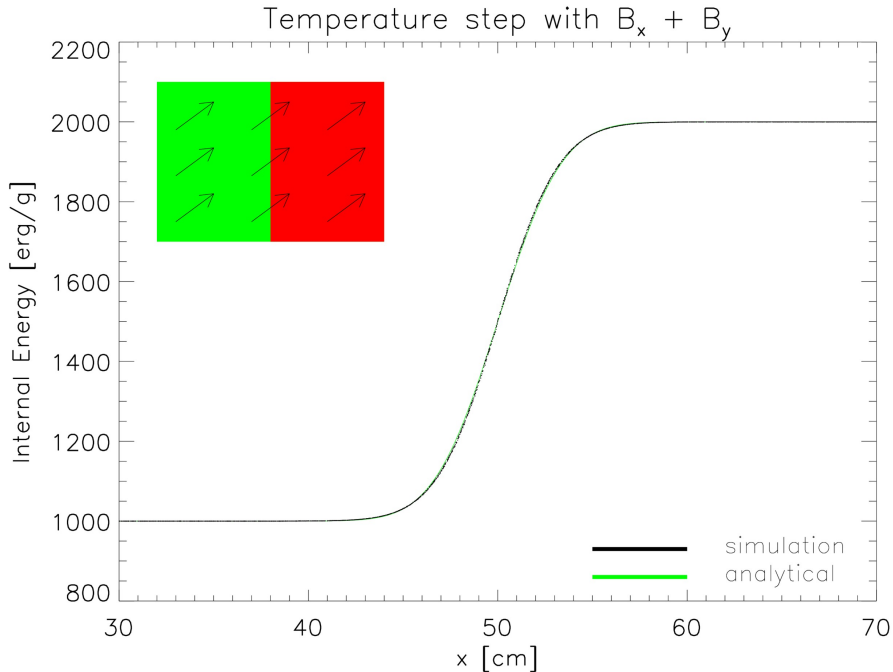


Figure 18: Temperature step with a homogeneous magnetic field. The magnetic field lines enclose an angle of  $45^\circ$  with the x-axis. Here we checked the implementation approach **1a** (see table 2). Type **1b** gives us exactly the same result. Plotted is again the analytic solution in green and the SPH particles in black. As before these match up very well.

little broad bumps in the result, which we unfortunately can not explain.

The whole result is symmetric, as the initial setup suggested. We get more scatter than in our previous runs, which is probably related to the wrong behaviour of the solution. Furthermore the quadratic kernel derivative can be a reason for this outcome.

At this point it is not yet clear, if the algorithm is simply wrong or just has problems with discontinuities in the temperature. Therefore we will have to further investigate it's behaviour with other tests.

To check for the convergence behaviour in this case, we let the simulation run for a much longer time. A plot for a 100 times later snapshot is shown in figure 20. As we see, the result converges more and more towards the analytic solution. The temperature values at the initial discontinuity do not stay unchanged and start to approach their final values. Induced through the initial error we see oscillations in

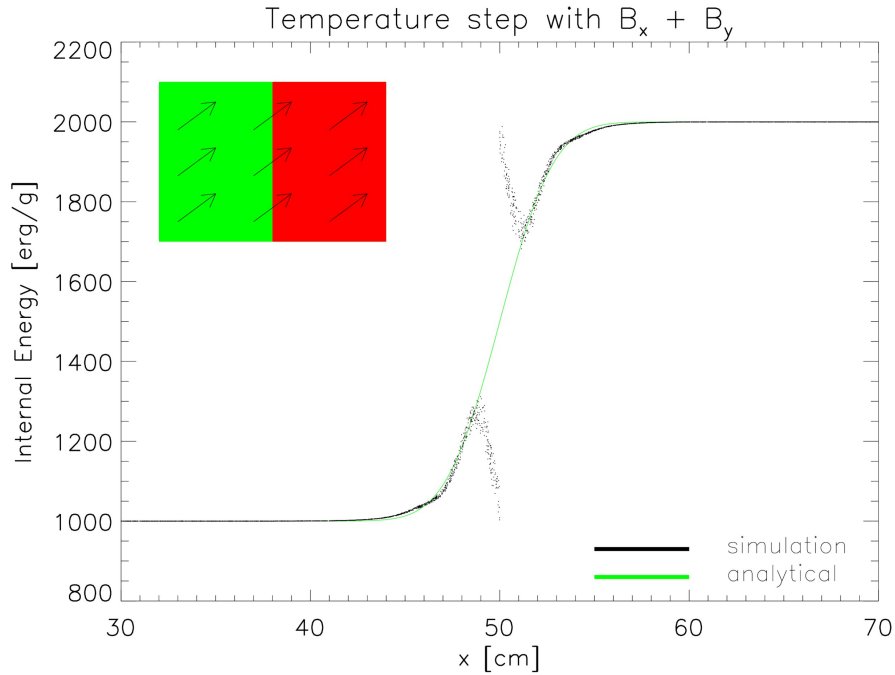


Figure 19: Temperature step with a homogeneous magnetic field. The magnetic field lines enclose an angle of  $45^\circ$  with the x-axis. Here we checked the implementation approach **2** (see table 2). Plotted is again the analytic solution in green and the SPH particles in black. We see, that the algorithm follows the analytic solution farther out from the step itself, however the discontinuity seems to be a big problem.

the temperature profile with decreasing amplitude the farther we go away from the center. The oscillations are expected to damp even more as the simulation progresses in time, so that the temperature will reach the final state of  $u = 1500 \text{ erg/g}$  at some point. Since the error function in the solution becomes rather flat for late times we expect the errors to be present for a rather long period, though. Still this is a rather good result, since the errors get damped away instead of being stable or even growing.

In section 4.2.2 we briefly mentioned the possibility of a flux limiter, which ensure energy transport in the correct direction. However we stated, that we would not further pursue this idea. The reason for this can be seen in figure 21: With the flux limiter we get even worse results, than without. There is more scatter all around

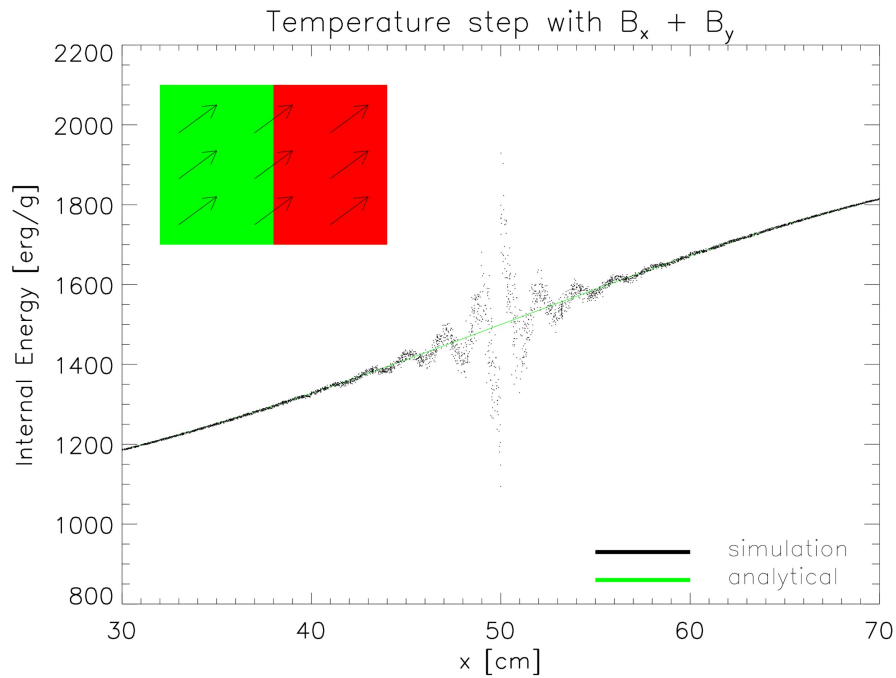


Figure 20: The same simulation as figure 19 at a hundred times later time. We see, that the solution further converges to the analytic result, however we get more and more oscillations due to the error at the initial temperature step.

the analytic solution and surprisingly we get particles from the warm region which heat up even more. But this is exactly the behaviour we wanted to prevent, by applying the flux limiter. This shows us, that it is not a very good decision to add such strong artificial constraints into a difficult numerical formula.

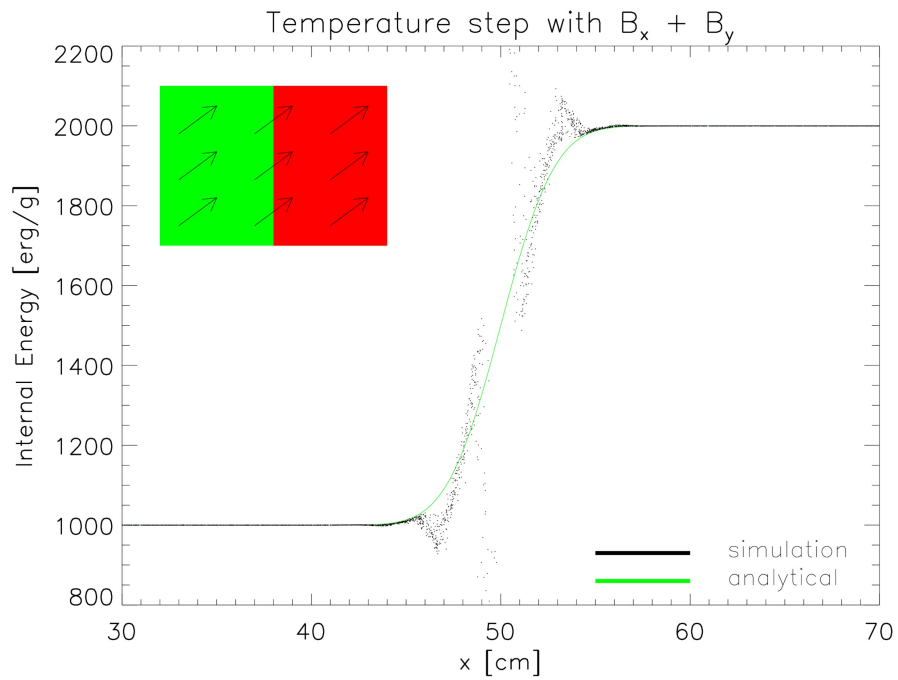


Figure 21: Simulation again with implementation type **2**, but now with a flux limiter to ensure energy transport only from warm to cold regions. Although we can still recognize the basic shape of the solution, this basically destroys the whole solution. Therefore we give up on the idea of such a limiter.

Let us now come to the third implementation we derived, or rather the two variations with a fully anisotropic setup and a more isotropised variation. We fit the results again to the same modified analytic solution as before.

The first possibility (**3a**) is plotted in figure 22. This implementation can reproduce the analytic solution quite well, however we get more scatter than in the previous runs. It is yet still not clear, what the origin for this noise exactly is, but for a cosmological simulation this won't matter too much since thermal conduction is not the dominating effect anyway. Probably it is due to the fact, that this formulation does not ensure a positive definite transport matrix, which induces errors into the conjugate gradient solver. However we see, that for a  $45^\circ$  magnetic field, we do not really need an artificial isotropisation.

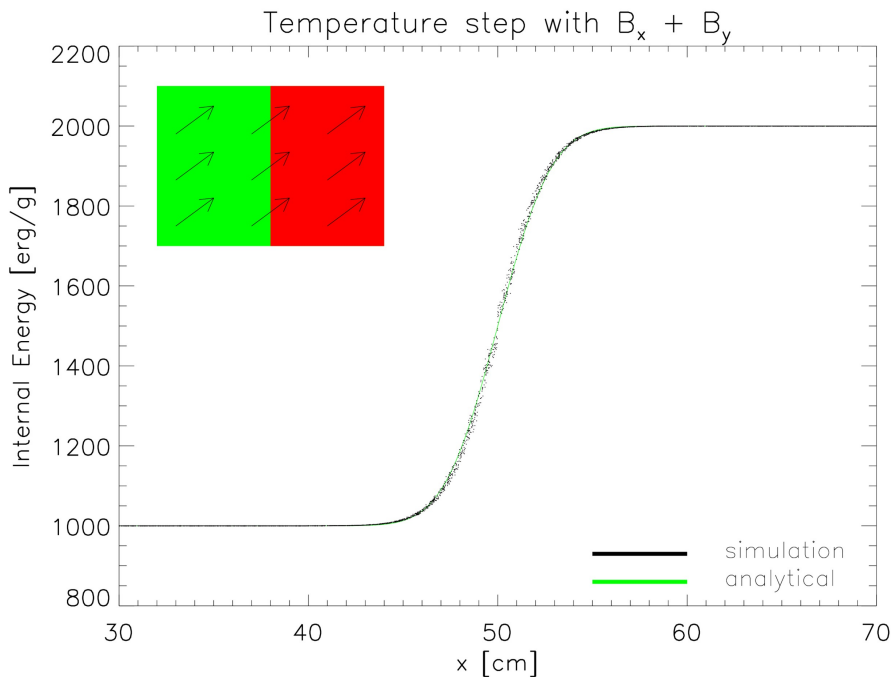


Figure 22: The temperature step problem, simulated with implementation type **3a**. We see quite some scatter, but the simulation reproduces the analytic solution well.

In figure 23 we show the latter case of a more isotropised formulation. It was clear from the beginning, that we would never get the exact analytic result, since the isotropisation was artificially added into the numerics. As we can see here, our result is not too far off the real solution. In contrast to the full anisotropic

formulation we get less scatter since the anisotropic part of the equation is mixed with an isotropic component and therefore has a weaker effect.

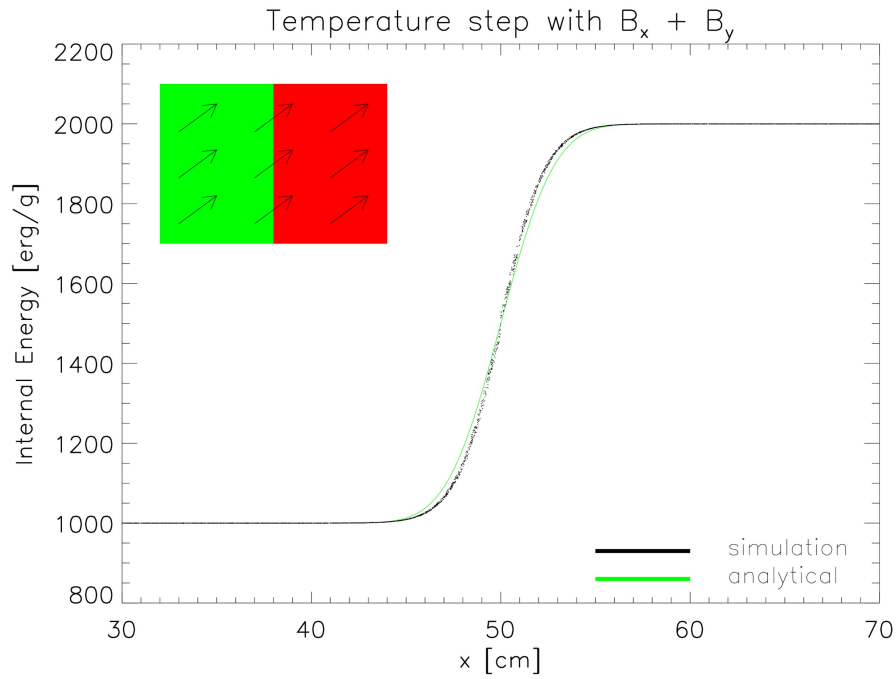


Figure 23: Same as the previous plots, now simulated with implementation type **3b**. As expected, the simulation produces a result which is a little off the analytic solution, although the general shape matches very well.

So far we have run all tests with a magnetic field  $45^\circ$  to the temperature gradient. To exclude the arbitrariness of this choice and to study some more properties of the different implementations, we want to carry out the tests also with two other setups:

- A magnetic field along the temperature gradient to check if the isotropic case can be recovered with the new code with sufficient accuracy.
- The other extreme case of a magnetic field perpendicular to the temperature gradient to see, if the different implementations really recover total suppression of heat flux as we demanded in the beginning.

To shorten this discussion and make comparisons easier we have always combined all four runs into one figure extended over two pages. In fig. 24 we show the results for a parallel magnetic field.

As expected the simple approach reproduces the result exactly, since we did not change the numerical approach. So it recovers exactly the isotropic case.

The split-up approach and the fully anisotropic case of the final implementation show exactly the same result: The analytic solution is recovered very good, however there is again noise in the plot. It is very good, that we do not see any strange behaviour for implementation type **2** here any more, like we did for the diagonal magnetic field setup. Therefore the error we see in figure 19 is at least not only due to the discontinuity, but is strongly induced by the conduction component perpendicular to the temperature gradient. We expect to see a error dominated picture for the perpendicular magnetic field.

The isotropised run shows again less scatter, however the result is again a bit off the analytic solution.

In total these results are all fairly good in recovering the isotropic case.

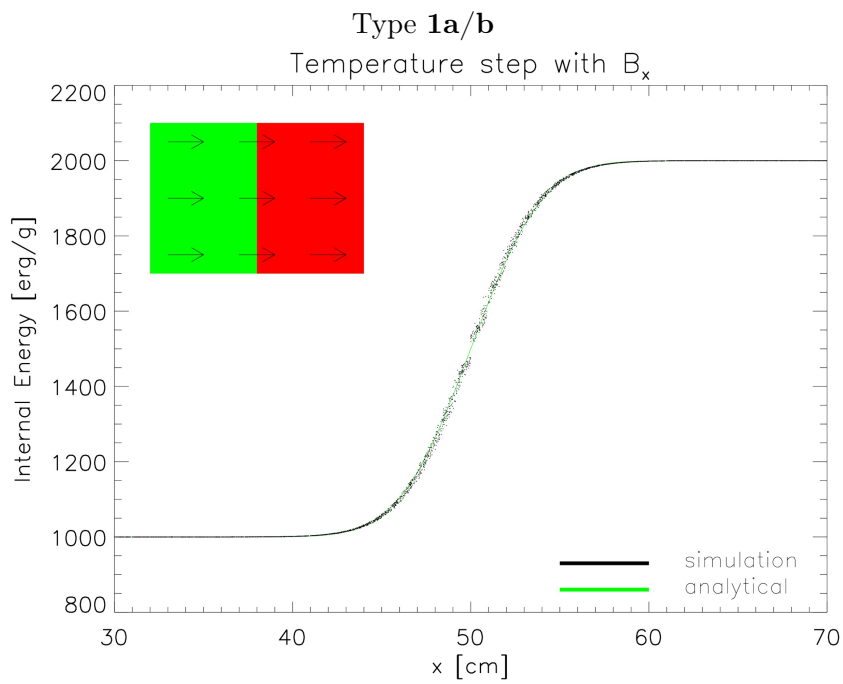
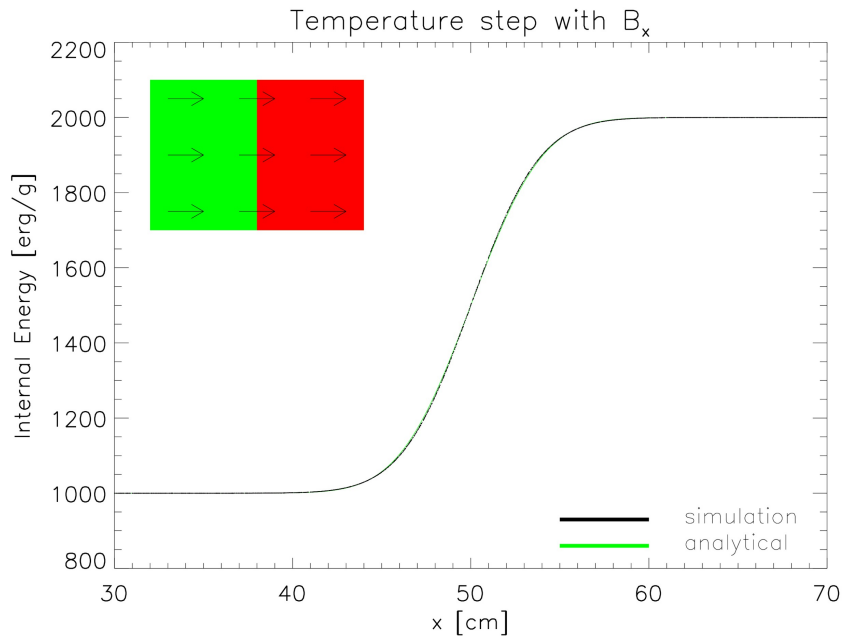
In figure 25 we show similar plots for a magnetic field perpendicular to the temperature gradient. From our preconditions we expect no conduction in this case, so the initial conditions should be stable except numerical noise.

The simplest implementation already shows some noise, which leads to conduction. But the state is not much evolved yet. Over time this error will progress more to outer parts and grow with increasing speed.

The split up approach shows less real progression of the initial state, however it presents more noise around. Warm particles get partially even hotter, which is not very good, even if it is just noise.

For the implementation type **3a** we see a rather stable solution as expected. We encounter again the regime, where the anisotropy is strong enough for heat to flow in the wrong direction. We expected that behaviour and this was why we implemented also the isotropised variation.

This approach can by construction not show a stable solution: The anisotropic part may be suppressed, but the isotropic part continues to work independent of the magnetic field. So we get in total less conduction, but still a clearly non vanishing component.



Type **2**

Figure 24: To be continued on the next page.

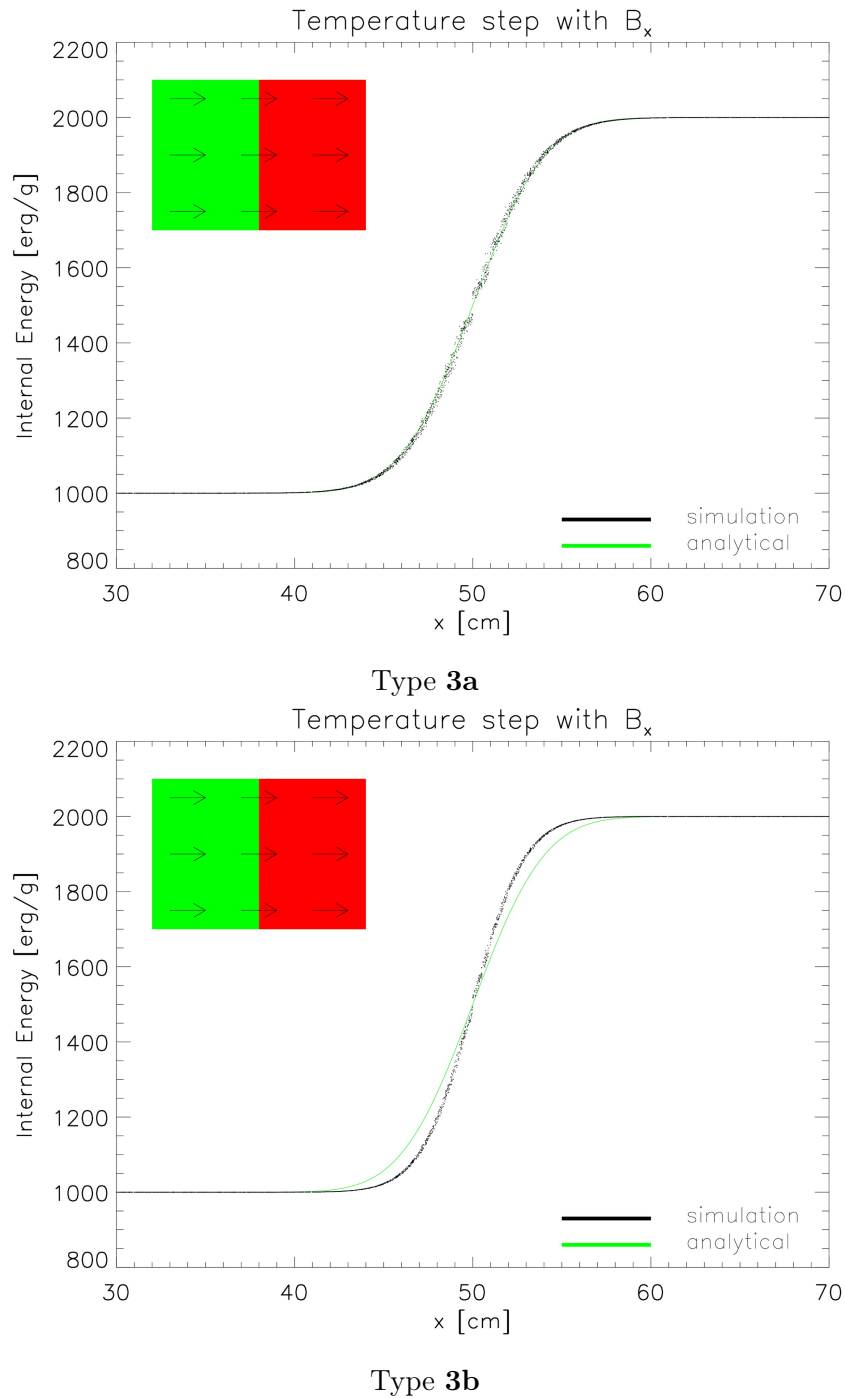
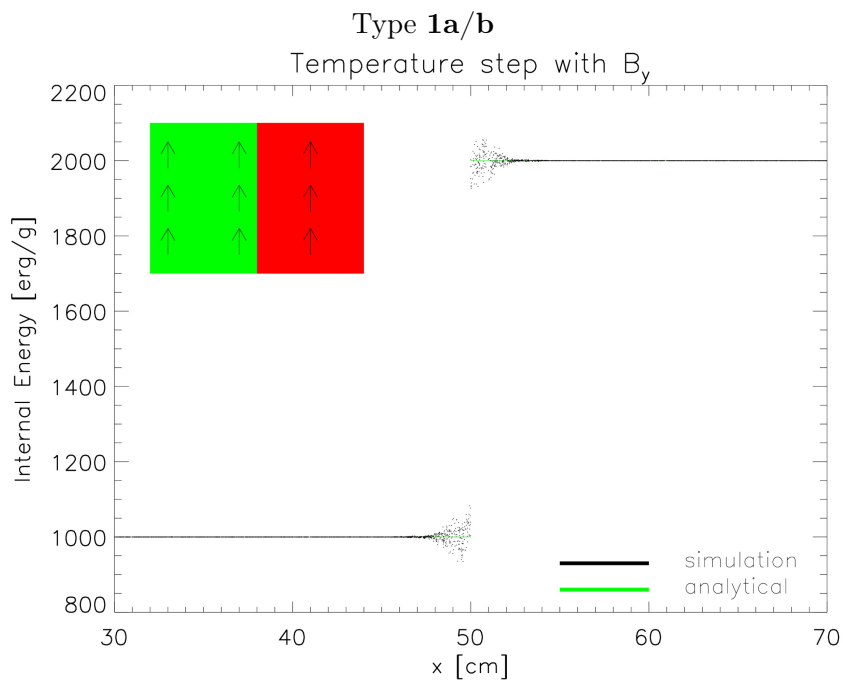
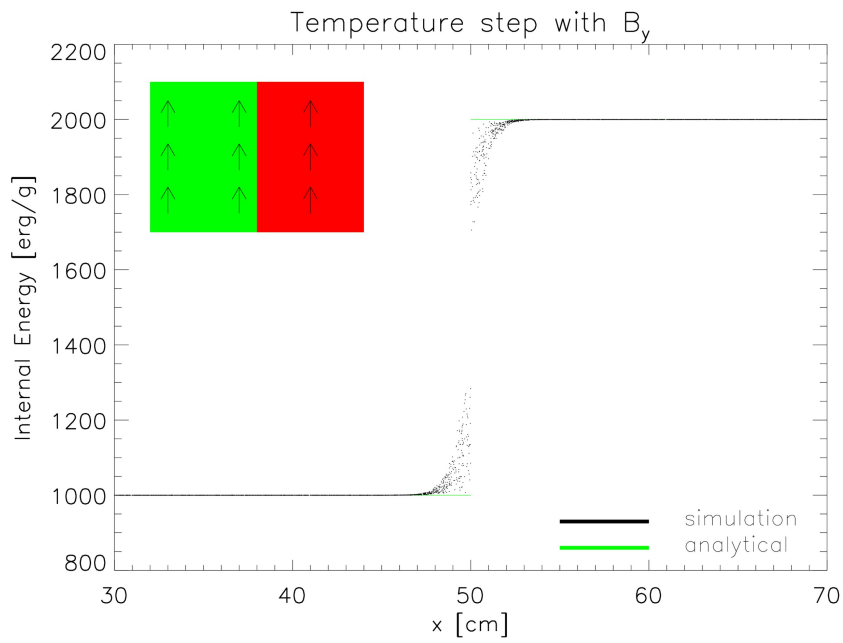


Figure 24: Temperature step problem with a magnetic field parallel to the temperature gradient. Comparison plots for all four implementations.



Type 2

Figure 25: To be continued on the next page.

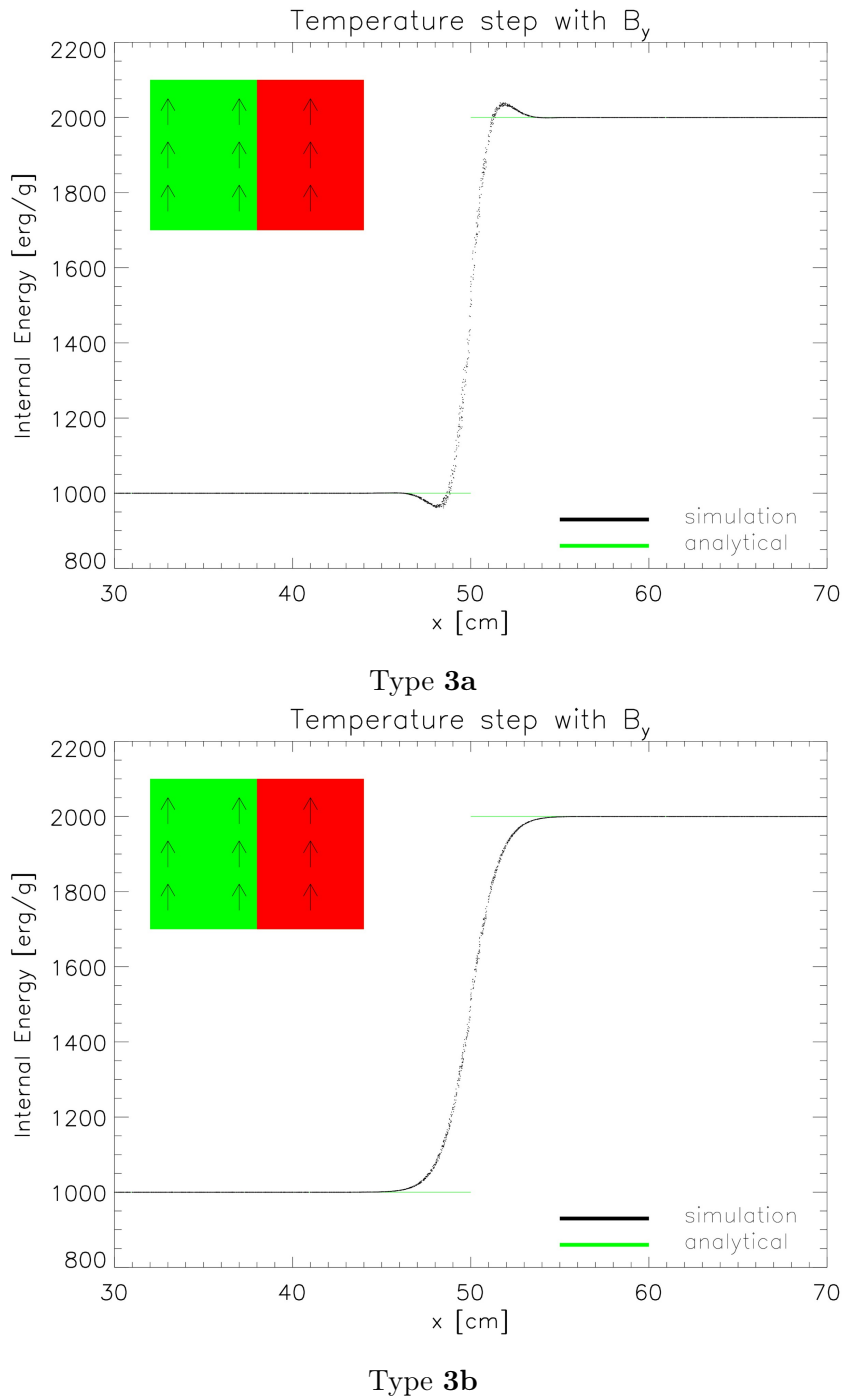


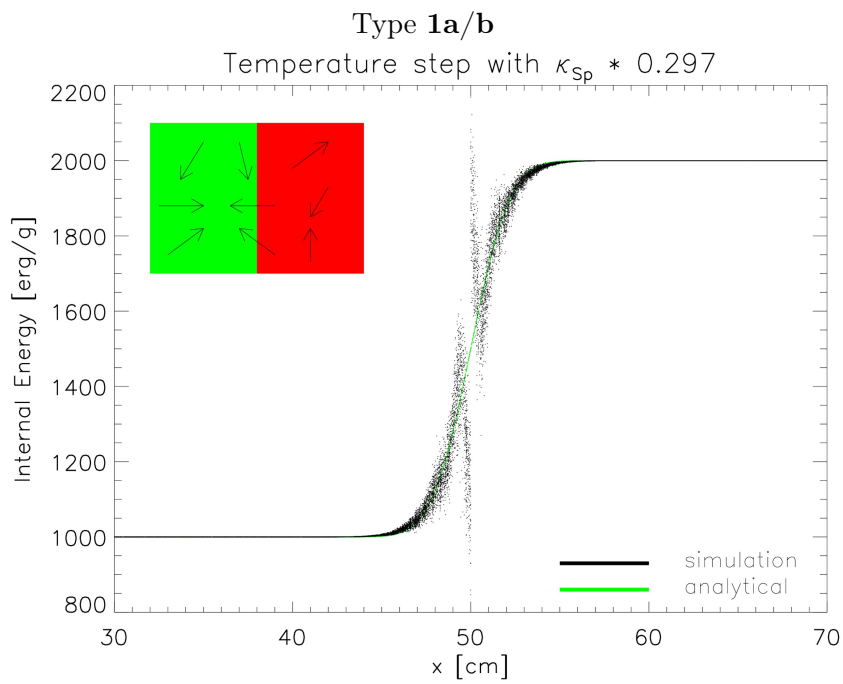
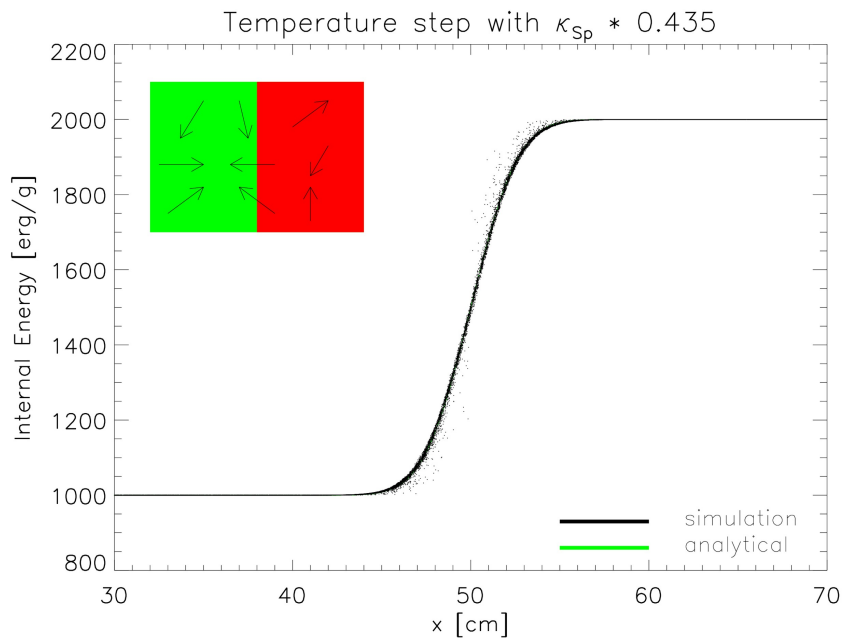
Figure 25: Temperature step problem with a magnetic field perpendicular to the temperature gradient. Comparison plots for all four implementations.

Finally we want to test what happens for a random chaotic magnetic field. In section 2.3 we have shown several opinions, how much a chaotic magnetic field should be overall suppress thermal conduction. Here we want to give an estimate for the suppression factor using our different implementations. We fit a factor of the conduction coefficient in the analytic solution to the SPH data points. Please note, that this result is not totally reliable, since we used a totally random magnetic field without ensuring  $\nabla \cdot \vec{B} = 0$ . Still we should get a fairly good estimate. Another comparison plot for this setup is shown in figure 26. We see the typical behaviour of the different implementations, as thoroughly discussed earlier. For the suppression factor due to the random magnetic field we get different results lying roughly between 0.3 and 0.44, depending which approach we trust most. An easy justification for these results can be given like in the following:

We set up a random distribution of values for the angle between the magnetic field and the temperature gradient. Assuming a temperature gradient for example in x-direction, we see that we are in fact interested in the distribution of  $\frac{|\vec{B} \cdot \nabla T|}{|\vec{B}| |\nabla T|}$ , since we should not care whether the magnetic field is either parallel or anti-parallel to the gradient. The mean vector for all magnetic fields is with respect to this variable is then (1; 1; 1), which leads to a factor of  $1/\sqrt{3}$  for the scalar product. In implementation type **1a/b** we have only this scalar product as a weighting factor, therefore we expect a mean conductivity of  $\kappa' \approx \kappa/\sqrt{3}$ , which is slightly higher than what the simulation shows us.

The other approaches contain effectively the scalar product squared, due to back projection onto the temperature gradient for comparison. This leads to a factor of  $1/3$ , which matches with the simulations' outcome. Furthermore one often assumes a suppression factor of about  $1/3$  (e.g. [Dolag et al., 2004], [Zakamska and Narayan, 2003] and references therein) to mimic anisotropic conduction with an isotropic code. This assumption is hereby justified by our results. Furthermore this matches the assumptions by [Rosner and Tucker, 1989], which we presented in section 2.4.





Type 2

Figure 26: To be continued on the next page.

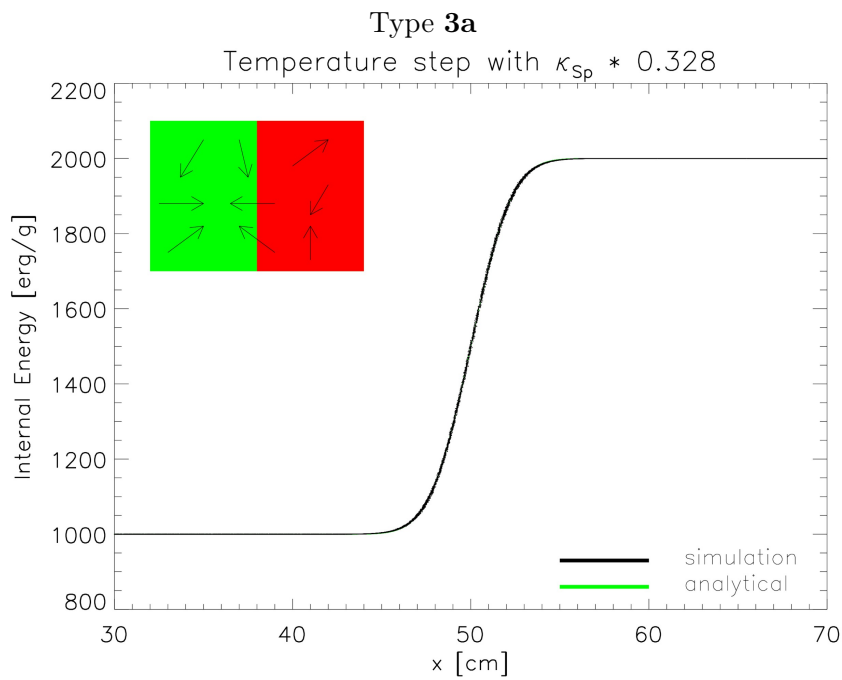
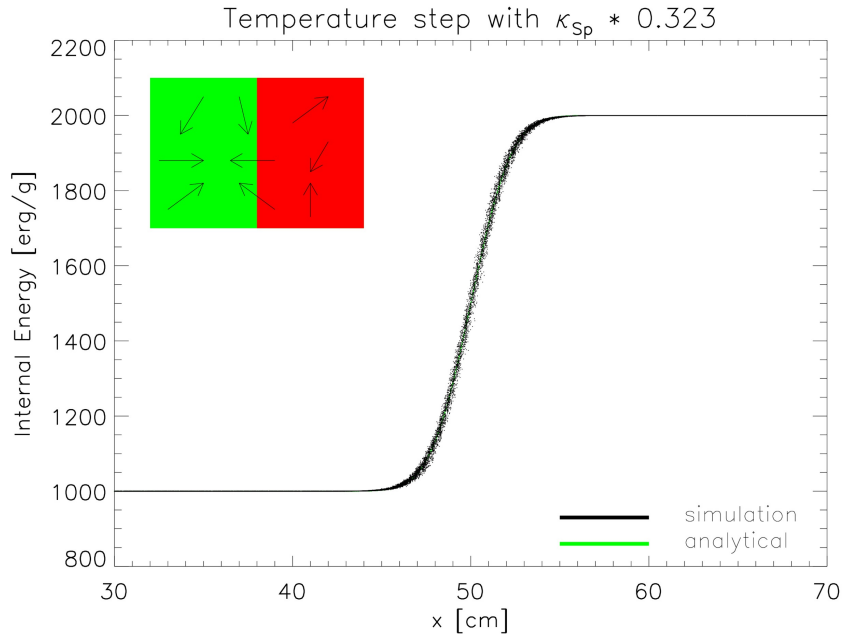


Figure 26: Temperature step problem with a totally random (not source free) magnetic field. Shown are comparison plots for all four implementations.

### 4.3.2 Sinusoidal temperature variation

Since the temperature step test contained an artificial discontinuity, we want to test the code also with a similar setup but taking a smooth temperature distribution. Like [Cleary and Monaghan, 1999] we decided to take a sinusoidal temperature distribution at  $t = 0$  which has one main advantage in comparison to other smooth setups: The analytic solution can be calculated without any numerics and is therefore well suited for comparison.

At first we derive the analytic solution for the initial conditions:

$$u_0(x') = u_0 \cdot \sin(kx) \quad (4.3.20)$$

with a generic wavenumber  $k$ . We plug this equation again into the last general step of the previous calculation, eq. 4.3.12 and get

$$u(t, x) = \frac{u_0}{2\sqrt{\pi\alpha t}} \int_{-\infty}^{\infty} dx' \sin(kx') \exp\left(-\frac{(x-x')^2}{4\alpha t}\right) \quad (4.3.21)$$

We use the Eulerian formula to express the sine as two exponentials:

$$\sin(kx') = \frac{1}{2i} \left( e^{ikx'} - e^{-ikx'} \right) \quad (4.3.22)$$

To solve the integral we will complete the square to be able to perform the standard Gaussian integration. The whole exponent can be written as

$$\begin{aligned} & \pm ikx' - \frac{(x-x')^2}{4\alpha t} \\ &= -\frac{1}{4\alpha t} \left[ x'^2 - 2(x \pm i2\alpha kt)x' + x^2 \right] \\ &= -\frac{1}{4\alpha t} \left[ (x' - x \mp i2\alpha kt)^2 \mp i4\alpha ktx + 4\alpha^2 k^2 t^2 \right] \\ &= -\frac{(x' - x \mp i2\alpha kt)^2}{4\alpha t} \pm ikx - \alpha k^2 t \end{aligned} \quad (4.3.23)$$

Therefore we get the two integrals, which differ only in some signs, (using eq. 4.3.11)

$$\begin{aligned} & \pm e^{\pm ikx} e^{-\alpha k^2 t} \int_{-\infty}^{\infty} dx' \exp\left(-\frac{(x' - x \mp i2\alpha kt)^2}{4\alpha t}\right) \\ & = \pm e^{\pm ikx} e^{-\alpha k^2 t} \sqrt{\pi \cdot 4\alpha t} \end{aligned} \quad (4.3.24)$$

Proof, that equation 4.3.11 is also valid for a complex exponent is presented in appendix C.

Summing up the two integrals and multiplying the result by the prefactor of equation 4.3.21 we get the final result:

$$u(t, x) = u_0 \sin(kx) e^{-\alpha k^2 t} \quad (4.3.25)$$

To cover a wide range of wave like initial conditions<sup>30</sup> we will specify two cases:

1. Half a wave inside a box with zero boundary conditions
2. A full wave (with constant offset to prevent negative energies) with periodic boundary conditions

For the first case we need to modify our calculations from above such, that the integral boundaries are be set to the box boundaries. So we can restart the calculations at eq. 4.3.24. We need again rules of complex integration to get to the following result<sup>31</sup>

$$\pm e^{\pm ikx} e^{-\alpha k^2 t} \sqrt{\pi\alpha t} \left[ \operatorname{erf}\left(\frac{L - x \mp i2\alpha kt}{\sqrt{4\alpha t}}\right) - \operatorname{erf}\left(\frac{-x \mp i2\alpha kt}{\sqrt{4\alpha t}}\right) \right] \quad (4.3.26)$$

Multiplying the prefactor we skipped and summing up the two terms we get in total

$$\begin{aligned} u(t, x) &= \frac{u_0}{4i} e^{-\alpha k^2 t} \\ & \cdot \sum_{\pm} \pm e^{\pm ikx} \left[ \operatorname{erf}\left(\frac{L - x \mp i2\alpha kt}{\sqrt{4\alpha t}}\right) - \operatorname{erf}\left(\frac{-x \mp i2\alpha kt}{\sqrt{4\alpha t}}\right) \right] \end{aligned} \quad (4.3.27)$$

<sup>30</sup>Without considering superpositions of different waves.

<sup>31</sup>As we prove in appendix C a simple integration, without special consideration of complex parts, like in section 4.3.1 is sufficient.

With the box size  $L$ . The integration details can be found in appendix C.

Despite the appearance of the remaining terms this expression is pure real for the domain of definition  $x \in [0, L]$ . Instead of showing this for the common case, we simply checked it for all of our example calculations. As we did with the previous test, we will at first run simulations with the existing isotropic implementation, to verify the code and our analytic derivation before we come to the second case. We set up a half sine wave with an initial amplitude of 1000 erg/g in our box and zero outside. The evolution of the temperature distribution taken at some arbitrary snapshot is plotted in figure 27.

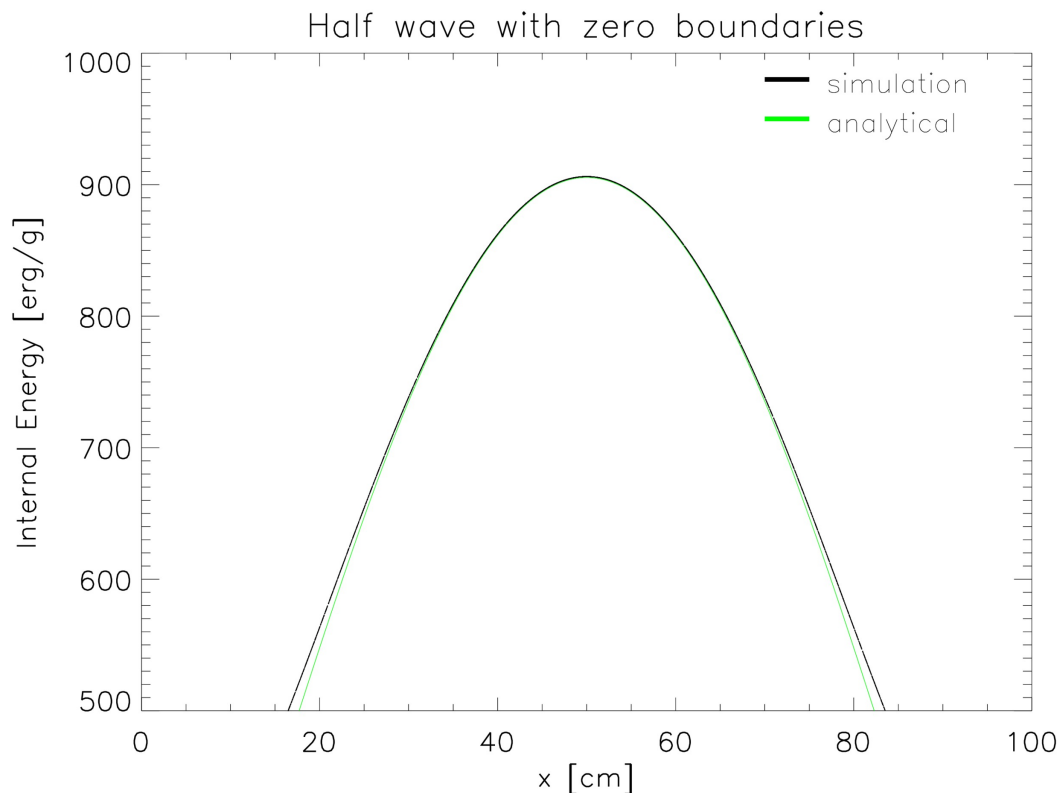


Figure 27: Test with half sinusoidal wave in temperature and zero boundary conditions without magnetic field. The green line is the analytical solution (eq. 4.3.28), the black dots are SPH particles. In the middle part the simulation agrees very well with the analytic solution. The outer part is not as reliable, since SPH estimates are not very exact at the boundaries.

The simulation and the analytical solution match up pretty well, except when it comes near to the box boundaries. Since there are no more particles outside the initial sine wave, the SPH approximations (for example for the density) break down and we get a result slightly off the real solution. This is expected and has nothing to do with the quality of the implementation, since it simply shows just an intrinsic property of SPH calculations themselves. Similar to the last section we used again a periodic setup in the  $y$  and  $z$  directions.<sup>32</sup>

For the second case we just need to add the effect of a constant offset to equation 4.3.25. This offset can be simply added to the result<sup>33</sup>, as we have seen by the calculations in section 4.3.1. Therefore we get the following result:

$$u(t, x) = u_1 + u_0 \sin\left(2\pi \frac{x}{L}\right) e^{-4\pi^2 \alpha t / L^2} \quad (4.3.28)$$

We chose  $u_1 = 1500$  erg/g and again  $u_0 = 1000$  erg/g. The resulting plot comparing simulation outcome and solution is shown in figure 28.

In comparison to the last setup we have no boundaries with missing particles, so we get a very good match up between the simulation and the analytic solution.

Now that we know, that the isotropic implementation reproduces the result of our calculations, we can redo the tests with magnetic fields included. We will however only carry on with the second test setup, to prevent confusion because of the errors we found in the first case. We compare the simulations to similar modified analytic solutions, as we did for the temperature step:

- $\kappa' = \kappa \cdot \cos \angle \left( \vec{B}, \nabla T \right)$  for implementation type **1a/b**
- $\kappa' = \kappa \cdot \cos^2 \angle \left( \vec{B}, \nabla T \right)$  for the others

At first we put in a magnetic field of arbitrary strength parallel to the x-axis. Since the magnetic field is then exactly parallel to the temperature gradient, we expect the anisotropic implementations to reproduce the same findings we just presented

<sup>32</sup>Actually we use periodicity in all three spatial directions and expand the numerical box in x-direction around the sine wave, to mimic non periodicity.

<sup>33</sup>Only for periodic boundary conditions!

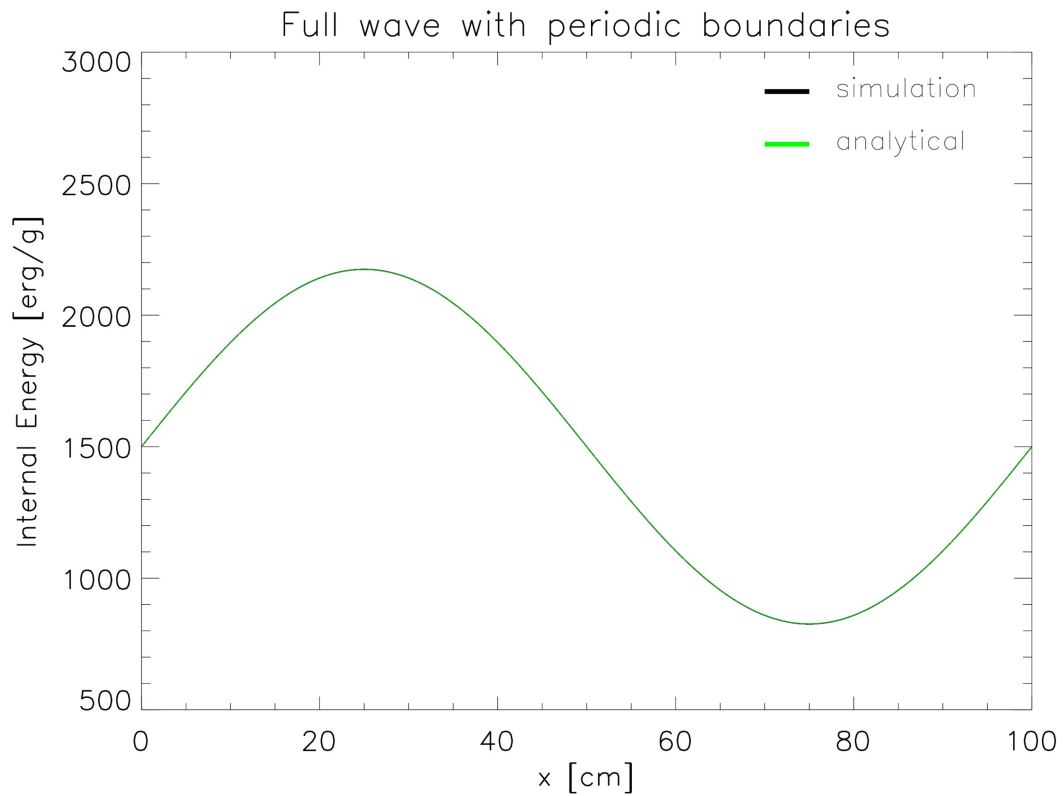


Figure 28: Test with full sinusoidal wave in temperature and periodic boundary conditions without magnetic field. The green line is the analytical solution (eq. 4.3.28), the black dots are SPH particles. We get even less scatter for this smooth setup as we had with the temperature step earlier. Both solutions match up so well, that one can hardly see the SPH particles plotted behind the analytic solution.

for the isotropic run. The results are shown in a combined plot in figure 29.

As previously with the temperature step distribution we get full agreement of the simulation outcomes to the analytic solution for all implementations except the isotropised run. It is expected to give a slightly wrong solution, like in previous runs.

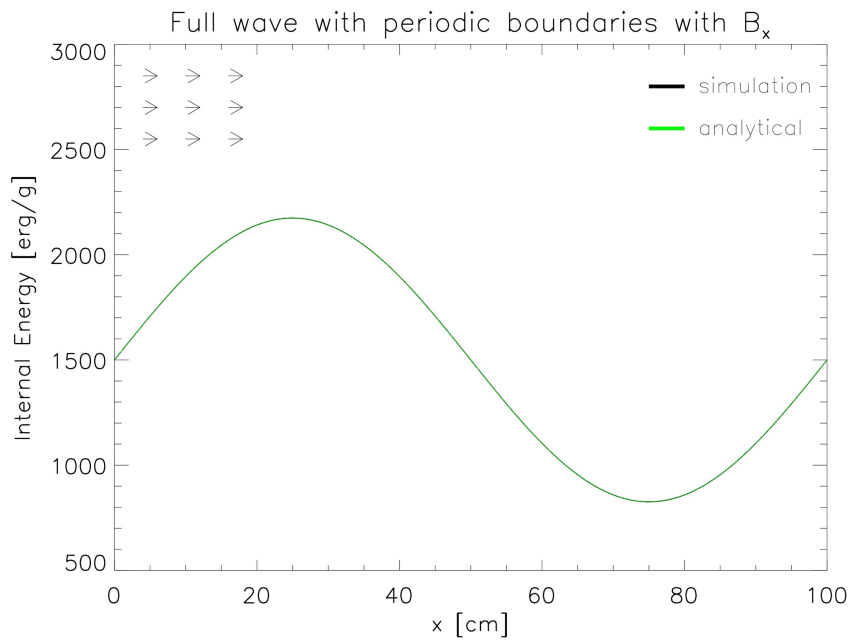
As we can see, when we compare figure 29 to the plots in fig. 24, we get much less scatter for a smooth initial setup in comparison to a discontinuity.

As a next step we include again a magnetic field parallel to  $(1; 1; 0)$ . As expected from the temperature step tests, we get again a good agreement for the simple approach of implementation type **1a** and **1b**.

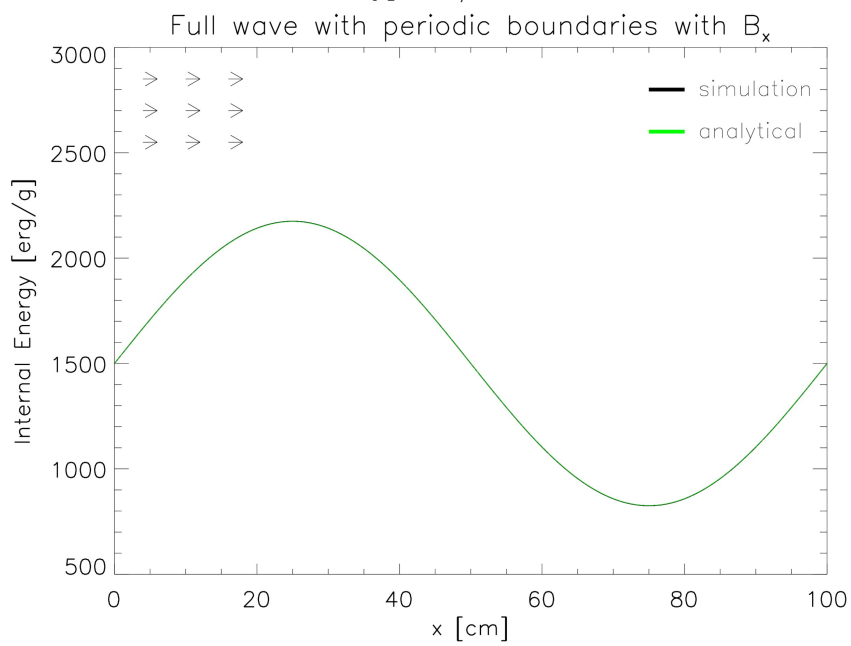
Before we had some problems with the split up approach, getting not such good matchups near a discontinuity. As predicted in section 4.3.1, we get perfectly good results for a smooth setup. We do not see any discrepancy nor is there much scatter. As further tests with much steeper gradients in the setup show, this behavior stays consistent, as long as there are enough particles to resolve the slope of the temperature distribution.

Similarly we do not get any noise for the remaining two runs. The fully anisotropic implementation **3a** fits the analytic solution perfectly while the isotropised run shows again the expected offset.

Finally we rerun the same test but with a magnetic field in  $y$ -direction, therefore we expect the temperature distribution to be more or less stable. In figure 31 we see nearly no noise in all of our four runs and except of the obvious error in the isotropised run (due to isotropic component, as before) we find very good matches with our predictions. It is interesting to see, that we do not see any heat being transported in the wrong direction with the implementation type **3a**, as we had it for the temperature step problem. Probably we just do not see any wrong conduction here since the temperature gradients are not as steep as for the discontinuity before.



Type 1a/b



Type 2

Figure 29: To be continued on the next page.

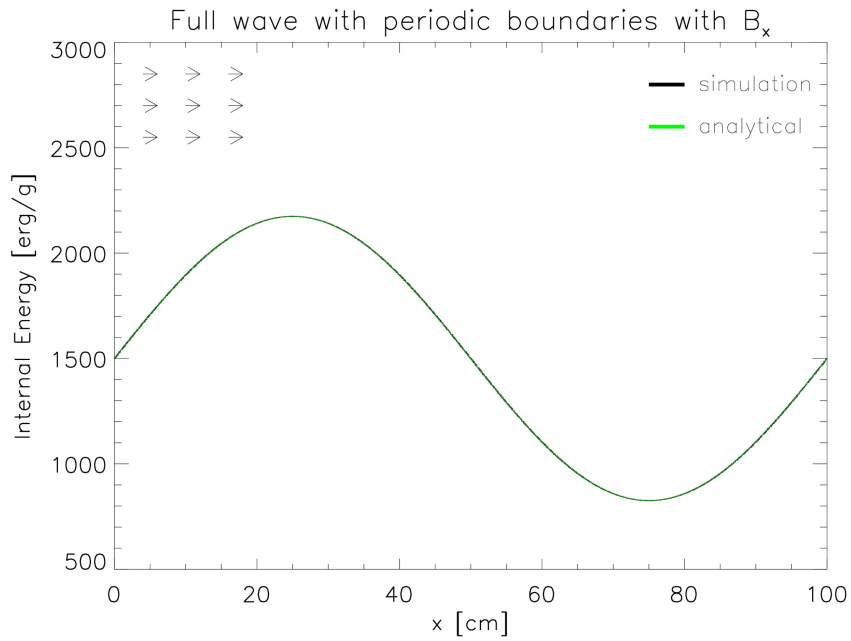
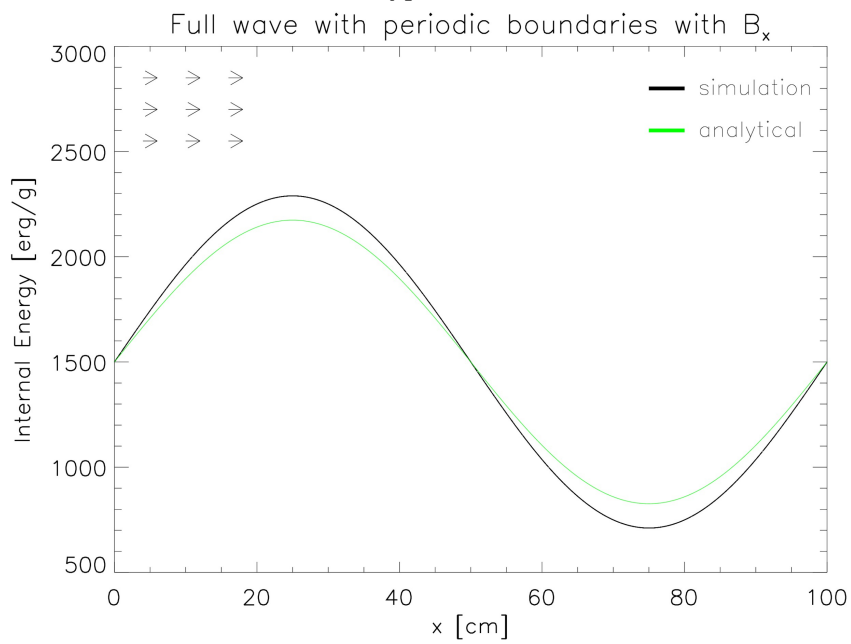
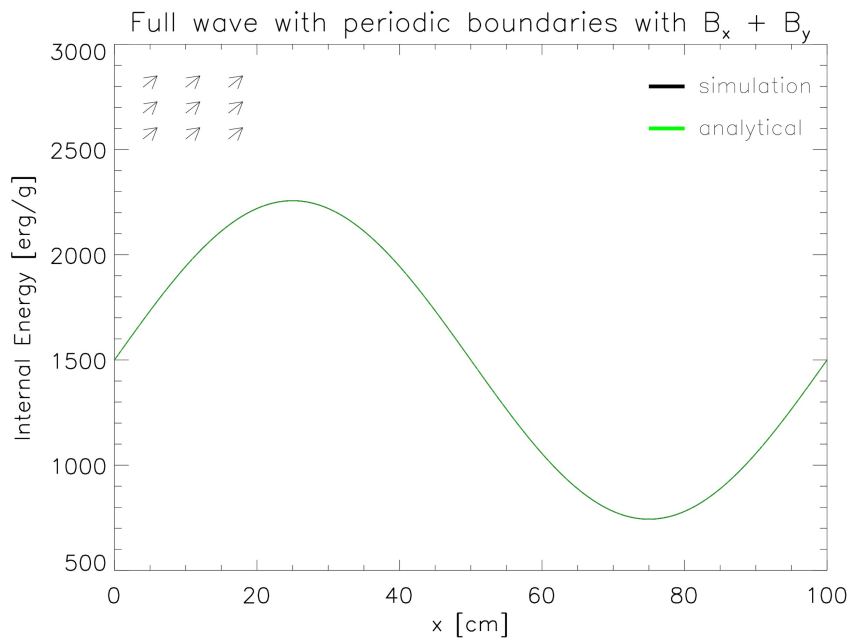
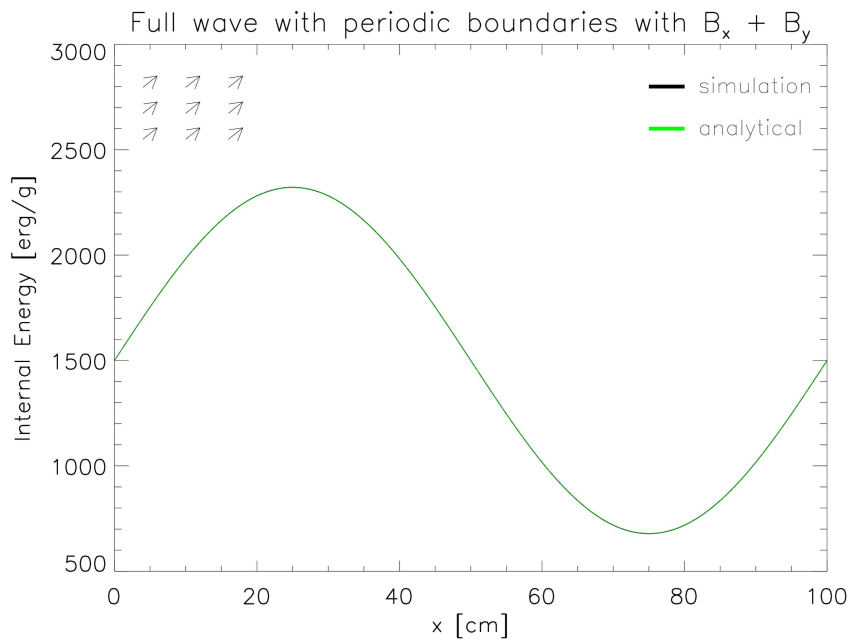
**Type 3a****Type 3b**

Figure 29: Test with full sinusoidal wave like temperature distribution and periodic boundary conditions with magnetic field parallel to the temperature gradient. Comparison plots for all four implementations.

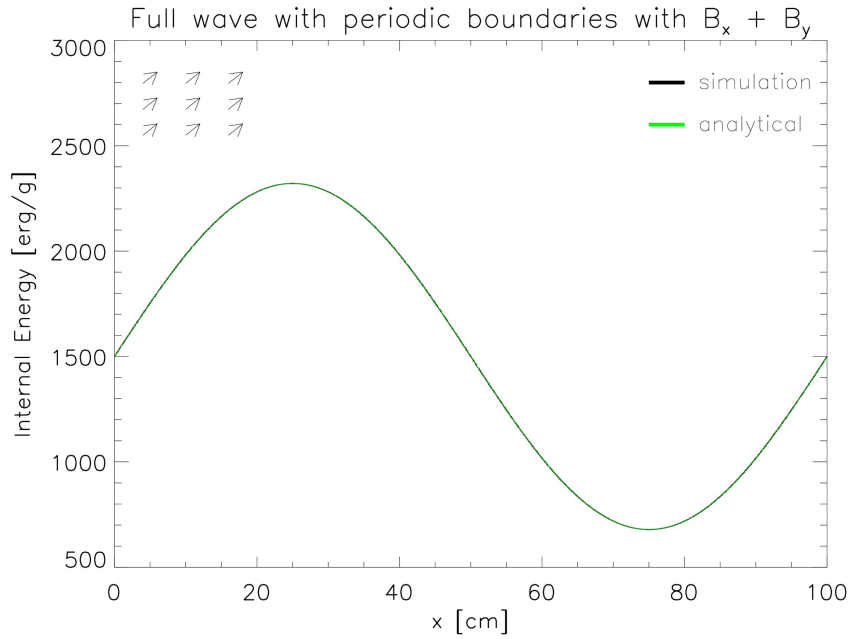


Type 1a/b

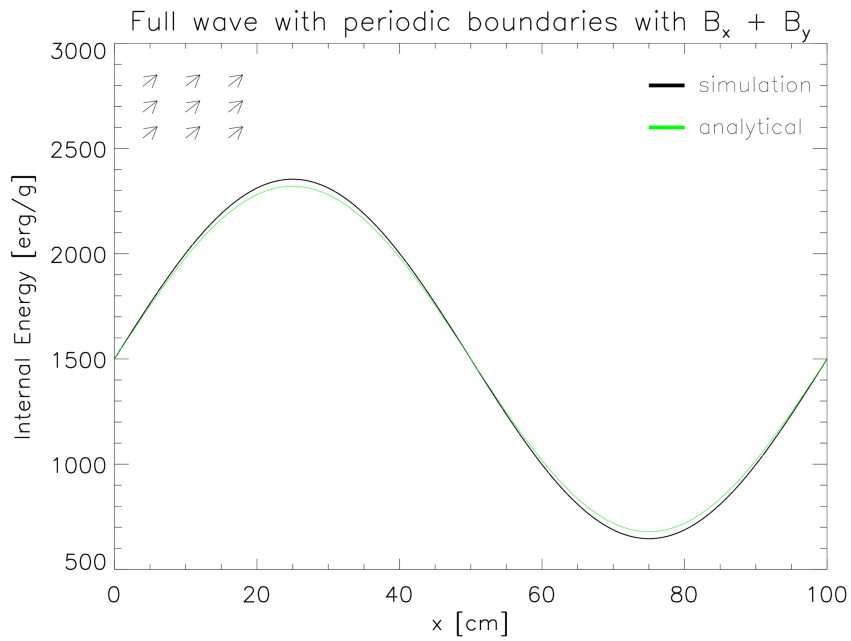


Type 2

Figure 30: To be continued on the next page.

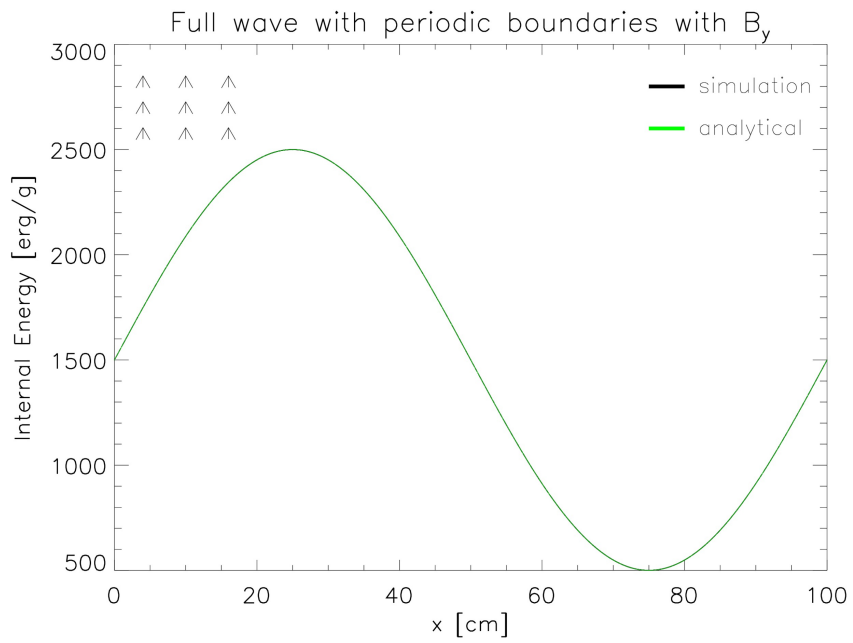


Type 3a

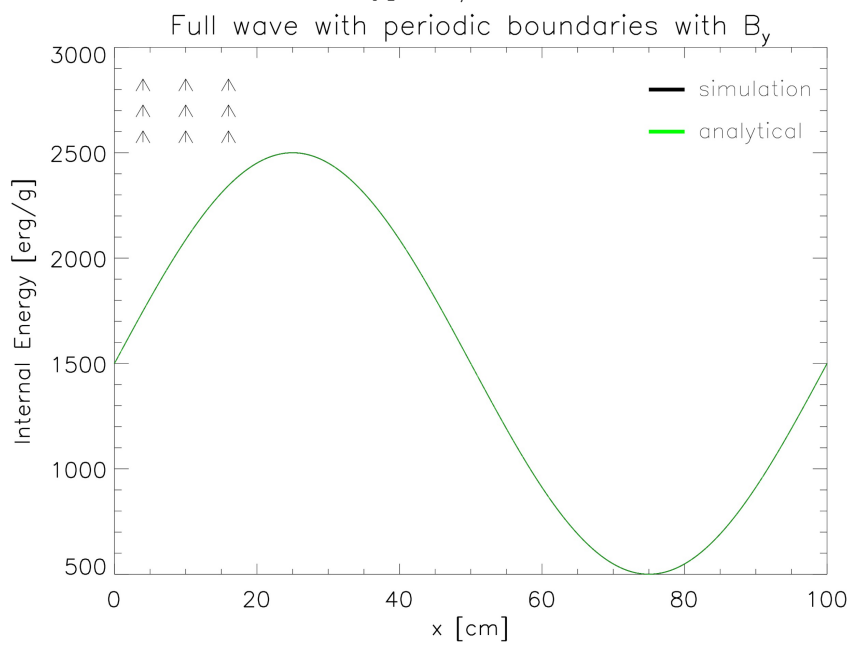


Type 3b

Figure 30: Test with full sinusoidal wave like temperature distribution and periodic boundary conditions with magnetic field  $45^\circ$  between x- and y-axis. Comparison plots for all four implementations.

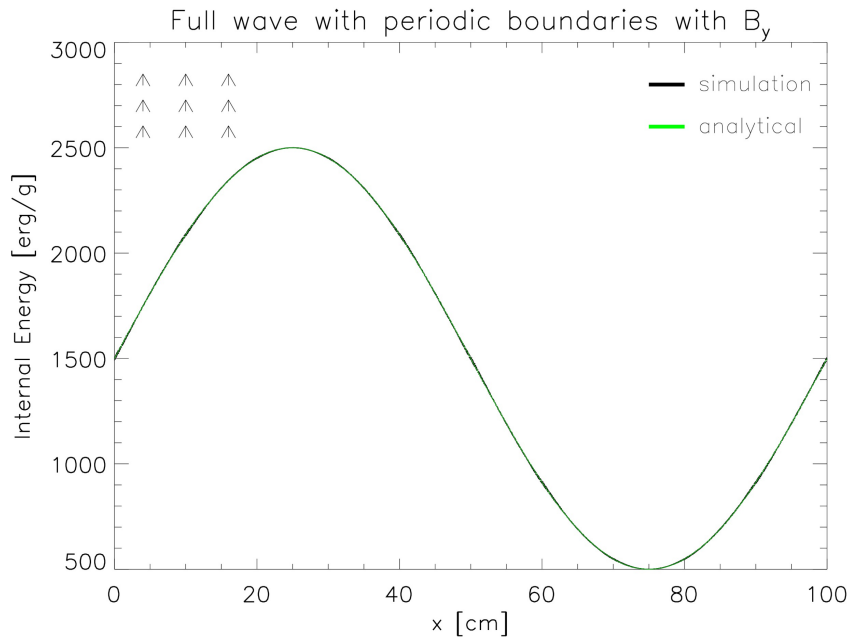


Type 1a/b

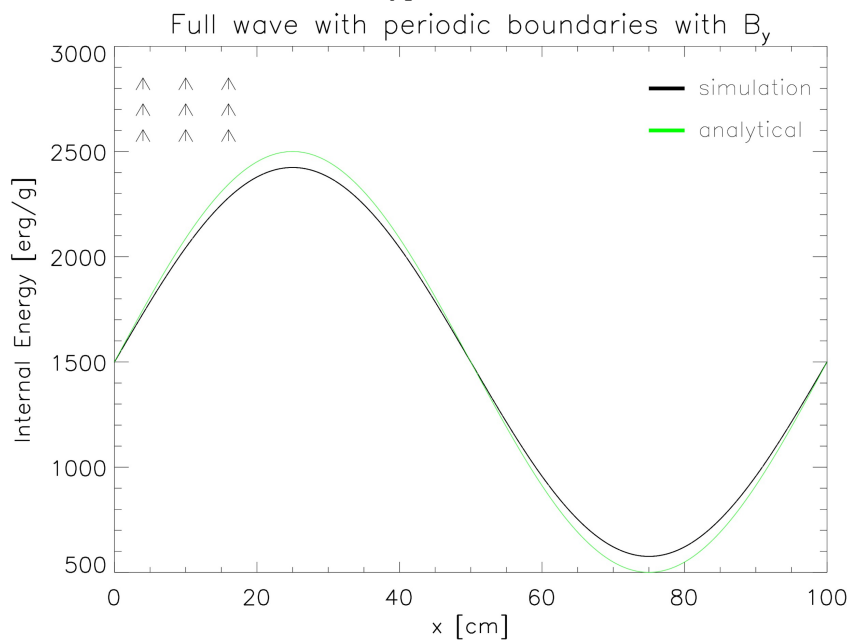


Type 2

Figure 31: To be continued on the next page.



Type 3a



Type 3b

Figure 31: For completeness the same sinusoidal setup with periodic boundaries. This time including a perpendicular magnetic field. Comparison plots for all four implementations.

### 4.3.3 Hot gas sphere

As next step we test how the code behaves for a more complex scenario. Similiar to the second test from [Jubelgas et al., 2004] we set up a sphere of hot gas. We use spherical symmetric initial conditions for the internal energy in the form of

$$u_0(r) = u_0 e^{-\beta r} \quad (4.3.29)$$

First we run the test again without any magnetic field. Similiar to the derivation of the solution of the 1D test, we start with the conduction equation with constant conduction coefficient and fixed particles. The calculations are except constants the same, so we can start with a modified version of equation 4.3.12:

$$u(t, x) = \frac{1}{(2\sqrt{\pi\alpha t})^3} \int_{-\infty}^{\infty} dx' \int_{-\infty}^{\infty} dy' \int_{-\infty}^{\infty} dz' u_0(\vec{x}') \exp\left(-\frac{(\vec{x} - \vec{x}')^2}{4\alpha t}\right) \quad (4.3.30)$$

Plugging in the initial conditions (eq. 4.3.29) we have a three dimensional integral over an exponentially damped gaussian. This integral is however not easy to solve so we have to rely on numerical integration methods. To preserve the quality of the solution and to be able to verify the simulation results with it, we will use an existing implementation for the numerical integrator. Since we utilise IDL for our plotting routines it is convenient to use the provided integration solver *int\_3d*.

To prove, that the code and the integrator produce the same results, we run the test at first again without any magnetic field, hence isotropic conduction. The results from the simulation as well as from the numerically integrated equation 4.3.30 are shown in figure 32. The simulation result and the analytical solution match up pretty well. Slight differences occur because of the numerical integration (especially the choice of integration boundaries) in the analytic solution as well as because of the resolution of the simulation. The bin sizes are strictly limited by the amount of particles in the simulation.

Now we include a homogeneous magnetic field pointing in x-direction. The calculation of a analytical solution is even more complicated as before. One would have to start the calculation from the beginning with the modified conduction equation and recalculate the Fourier transformations. Unfortunately a Cartesian approach

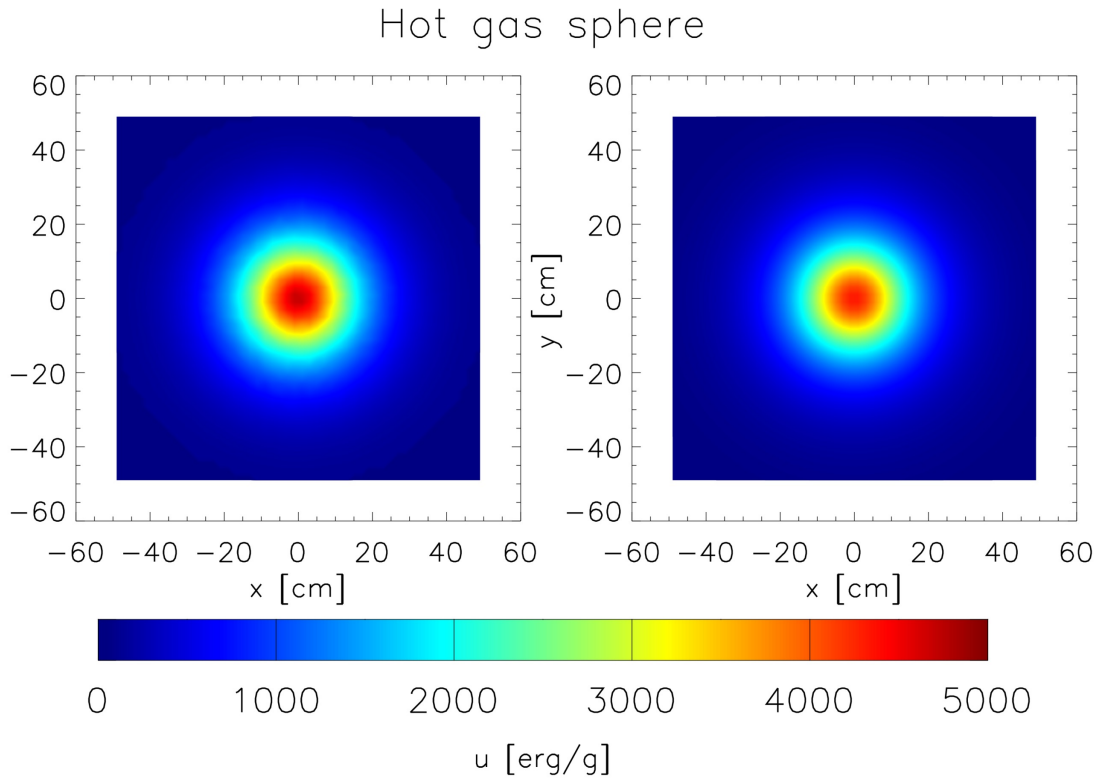


Figure 32: 3D conduction test: Temperature map of a hot gas bubble without a magnetic field. The plots show a slice through the middle of the bubble. The left image shows the simulation results while the right one displays the numerical integration of the analytic solution.

as well as using spherical coordinates leads to non converging integrals. Therefore we can only analyse our code's results qualitatively.

At first we run the code with implementation **1a**. The result at the same time as the last plot is shown in fig. 33.

Since the implementation should suppress energy transport perpendicular to the magnetic field, we would expect to have a higher transport and therefore smoothing in x-direction than in y- and z-direction. In the plot we see however a totally contradictory behavior. The implementation of type **1b** does not lead to any better results, therefore we can hereby rule out the approach of just reducing the conduction strength via the direction of the magnetic field.

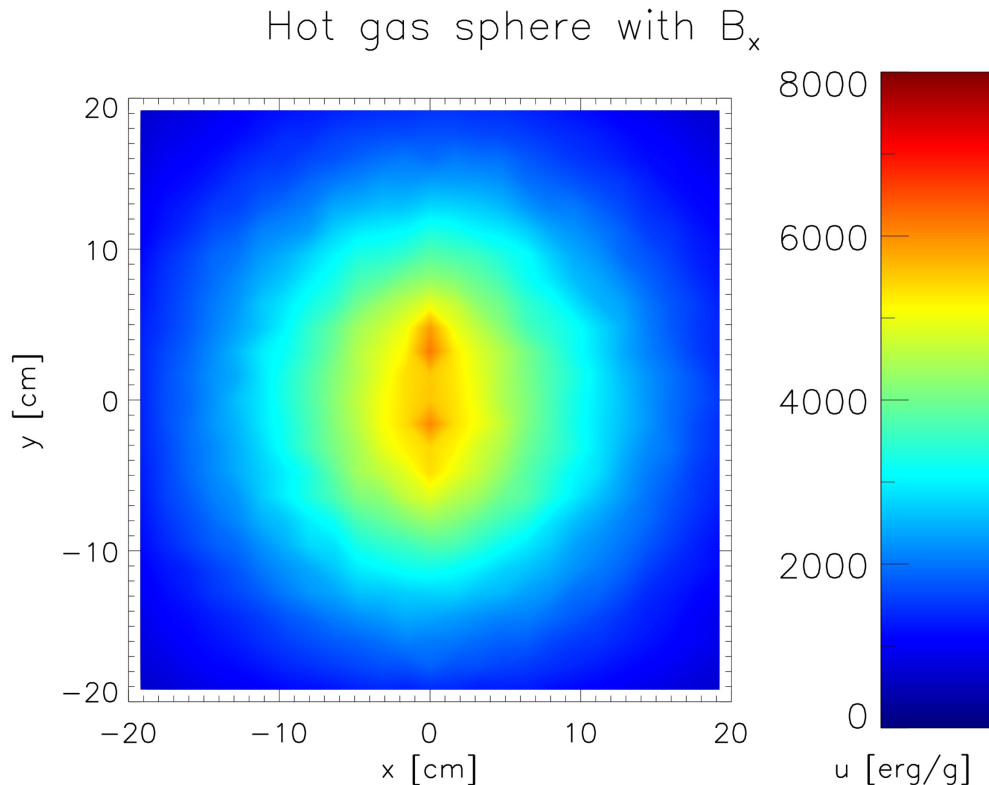


Figure 33: Hot gas bubble with a homogeneous magnetic field in positive  $x$ -direction using implementation type **1a**. Plotted is only the simulation result. The results are totally contradictory to our expectations and therefore rule out the approach.

The test using implementation type **2** (figure 34) leads qualitatively to the expected result. The range of temperatures is also consistent with our expectations. Since we do not only change the direction of the energy transport but also decrease the efficiency, the peak temperature should still be higher than in the run without magnetic field in figure 32. A comparison to figure 33 is not useful, since the total behavior of the implementation there is incorrect.

Running the same test with approach **3a** (figure 35) we get a similar result. The orientation of the ellipsoidal temperature distribution is correct, and we get similar values for  $|x| > 5\text{cm}$ . Only the central peak is much lower in this run, these

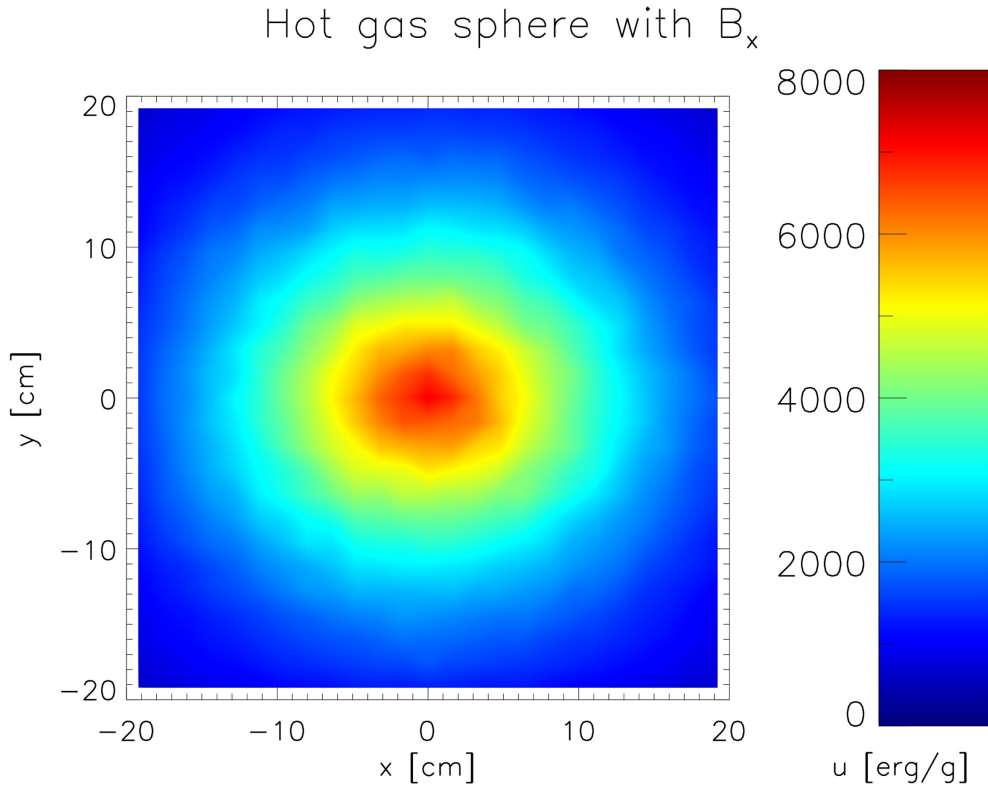


Figure 34: Hot gas bubble with a homogeneous magnetic field in positive  $x$ -direction using implementation type **2**. Plotted is only the simulation result. The overall behavior is as expected.

particles have given more energy away than before. It is not clear, which of these results is the better one.

For the isotropised run (figure 36) we get, overall lower temperature values and a much more circle like ellipsoidal structure in the central region. This matches our expectations, since we added an artificial isotropic component to the conduction.

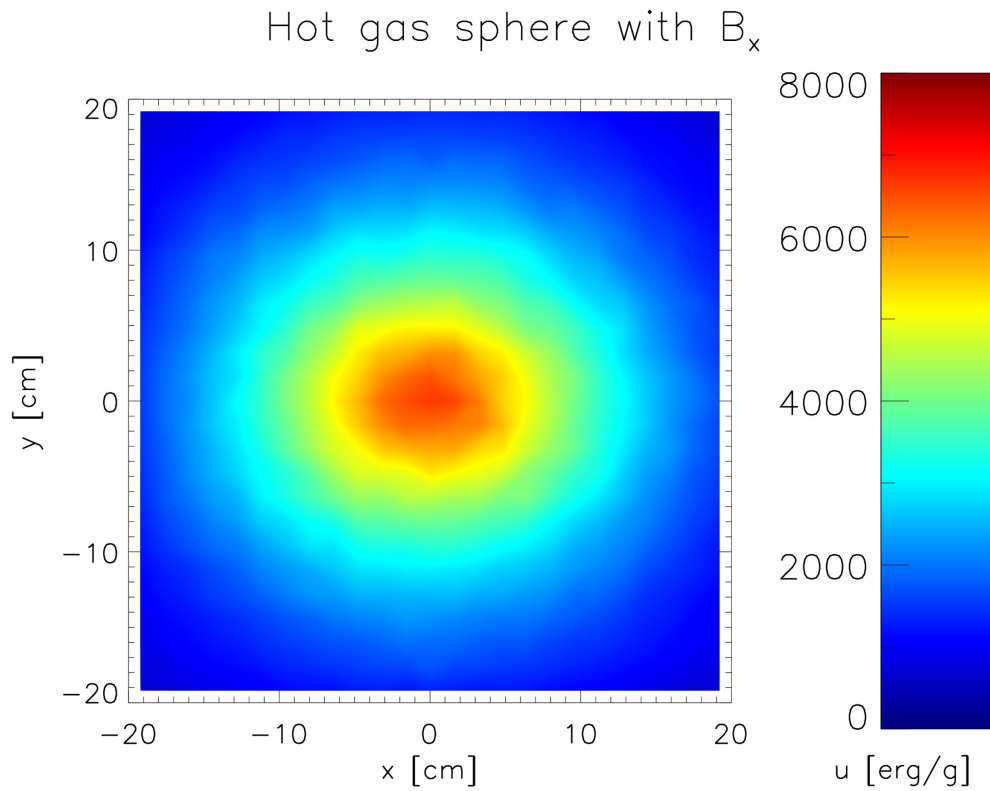


Figure 35: Hot gas bubble with a homogeneous magnetic field in positive  $x$ -direction using implementation type **3a**. Plotted is only the simulation result. The overall behavior is comparable to figure 34.

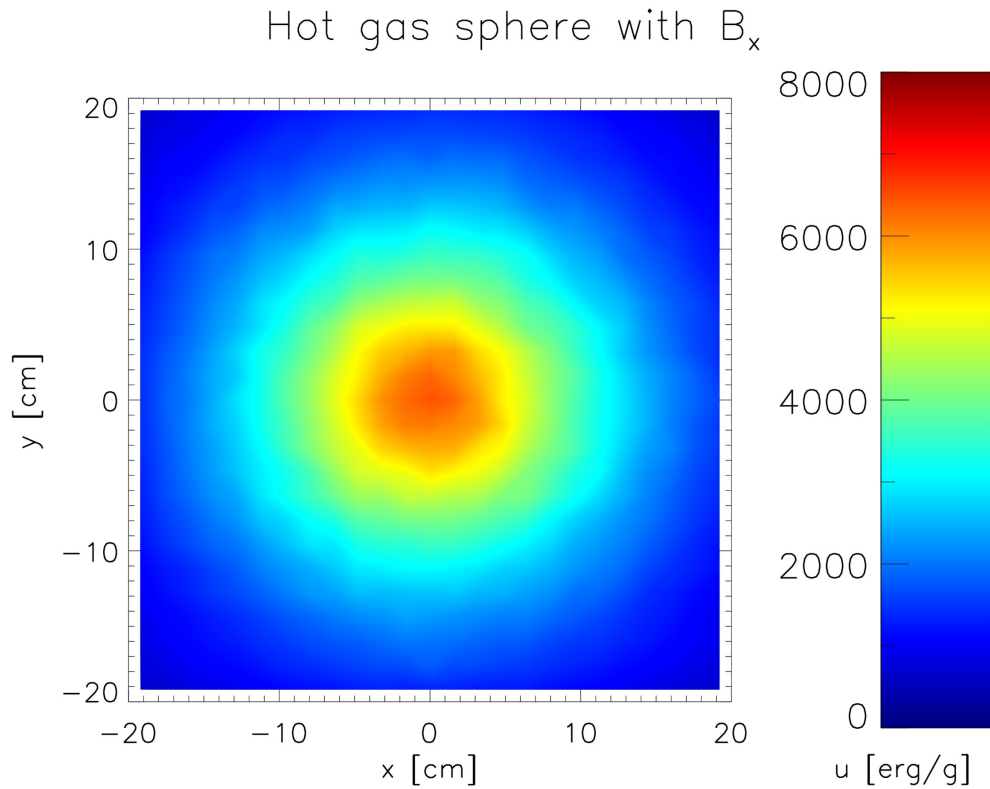


Figure 36: Hot gas bubble with a homogeneous magnetic field in positive  $x$ -direction using implementation type **3b**. Plotted is only the simulation result. In comparison to figure 35 the temperature is overall lower and the anisotropy is less present.

## 4.4 Summing up the test results

In the last section we have presented several ideas, how to implement anisotropic thermal conduction and thoroughly tested the approaches with different temperature and magnetic field setups. Before we finally come to cosmological simulations with the new code, we want to sum up our findings so far and try to decide, which implementation(s) we use for further runs.

### Implementation type **1a/b**:

We have seen in all tests, that for the approach of only weighting the conduction coefficient with the projection of temperature gradient and magnetic field, it does not make a difference if we recalculate this projection in each iteration step of the conjugate gradient solver, or not. Therefore **1a** and **1b** are equal and to save computation time we can neglect the recalculation.

In the hot sphere test we have seen, that this approach does not produce the expected result at all. It generated an anisotropy, but in the wrong spatial direction. It is not clear to us why this happened, but nevertheless this rules out the approach.

Except of this strong criterion we could anyway use this approach only in a very limited way, since it does not allow us to implement, how much we want to suppress conduction perpendicular to the magnetic field: It assumes always a total suppression, which is probably sufficient for galaxy clusters. However one would need be careful when it comes to other applications.

### Implementation type **2**:

We have seen that although the split approach gives us always more or less the expected solution, it has several limitations and problems on it's own:

The temperature step test in comparison to the sinusoidal setup revealed, that this approach has a serious problem with discontinuities in the temperature distribution. The outcome is in general not to bad, however we can not guarantee for temperature to be transported only from warm to cold regions. This leads not only to wrong physical results but also creates a lot of noise in the simulation out-

comes, since the conjugate gradient is not designed to work properly under these circumstances.

Additionally this approach uses two SPH loops, which limits its use to high order kernels only. Otherwise we would see much bigger errors and a lot more noise. Besides that, this approach is numerically highly inefficient (about twice the computation time as the other implementations), so it is not very wise to continue using it since we found better alternatives.

#### Implementation type **3a/b**:

These two implementations show promising results and it is very hard to judge, which one is better. The tests we did totally confirm our thoughts in section 4.2.3: If the setup is not extremely anisotropic we get very good results with the fully anisotropic approach (**1a**). For the temperature step test where we aligned the magnetic field totally perpendicular to the temperature gradient, we saw heat flux in the wrong direction similar to implementation type **2**. Still in general the results looked better with approach **3a**. And without the discontinuity we could not see this kind of wrong behaviour at all, which makes this implementation probably the best overall choice.

The isotropised version (**3b**) did never not show this kind of wrong transport of heat, however it could never reproduce the analytic solutions of our tests exactly due to the fact that we added an artificial isotropic term into the numerics. It is also because of that, that this implementation violates one of our prerequisites: to be able to fully suppress conduction perpendicular to magnetic fields (except of numerical noise of course). The isotropic component will always conduct heat, which makes total suppression impossible.

Both types show noise in the presence of discontinuities in the temperature distribution, however they reproduce the analytic solution very well. So they are the most favoured approach so far. It is hard to decide, which one is the better approach, since both have their advantages and disadvantages and all the errors we saw for them are only on a very small scale when it comes to cosmological dynamics. Therefore we will run our cluster simulations with both implementations and try to further judge from the outcome of these simulations.

## 5 Application to Galaxy Clusters

In this section we describe an existing set of cluster simulations, which we use for resimulations with various setups. We analyse the effects of our anisotropic conduction implementation in section 5.2 and discuss the influence of cooling, star formation and supernova feedback onto the simulation.

Afterwards we conclude by comparing our results to cosmological simulations including anisotropic conduction carried out by other groups in section 5.3.

### 5.1 Sample clusters from the Dianoga set

Resimulating a cosmological box from the Dianoga set, we are able to start with reference runs without thermal conduction and compare the outcome to existing simulations. Afterwards we can study the effects of isotropic as well as anisotropic thermal conduction.

The Dianoga set consists out of several galaxy clusters with masses  $M > 10^{15} M_{\odot}/h$ . A sample of 20 of these clusters is mentioned for the first time in the PhD thesis of [Bonafede, 2010] and further analysed in [Bonafede et al., 2011].

Following [Bonafede et al., 2011], we carry out our simulations with a  $\Lambda$ CMD<sup>34</sup> cosmological model using:

- $\Omega_m = 0.24$ : the cosmic matter density
- $\Omega_b = 0.04$ : the baryonic content
- $\Omega_{\Lambda} = 0.76$ : the vacuum energy density (cosmological constant)
- $h = 0.72$ : the Hubble parameter ( $H_0 = h \cdot 100 \text{ km}/(s \text{ Mpc})$ )

The initial power spectrum for density fluctuations is set up as  $P(k) \propto k^{0.96}$  using  $\sigma_8 = 0.8$  as amplitude on the scale of  $8 \text{ Mpc}/h$ .

---

<sup>34</sup>A cosmological constant and a cold dark matter component. For details see for example [Schneider, 2008].

We start with a cosmological box which produces one of the smaller Dianoga cluster in order to be able to run more simulations using different settings with moderate computational cost. Knowing that a smaller cluster may not be hot enough to show drastic differences between different conduction implementations<sup>35</sup>, it provides us at least with the opportunity to see, if the code produces reasonable results. For further reference please note, that the initial conditions we choose are identified by the id *g1574117*. This particular box is not treated in [Bonafede et al., 2011], but we will still be able to see, if our results in general fit their outcomes.

In the initial conditions gas particles are put in a box with side length of about 40 *Mpc*. Around this, there is a bigger box of length 1 *Gpc* with dark matter particles using varying resolution, to make sure that the evolution of the cluster is done correctly but to save computation time in the outskirts of the box.<sup>36</sup> This means, that the mass of the dark matter particles is increased outwards in three discrete steps. The different resolution steps and the gas particles are shown in figure 37. This cosmological box contains about  $3.8 \cdot 10^6$  dark matter and  $8.6 \cdot 10^5$  gas particles.

Having defined the initial conditions we describe the results of our different simulations in the next subsections.

---

<sup>35</sup>Since the conduction coefficient is proportional to  $T^{5/2}$ .

<sup>36</sup>In the  $\Lambda$ CDM cosmological model gravitational interaction of dark matter is expected to dominate the structure formation process. Therefore gas has to be put only in the region of interest, where we know that a structure forms by dark matter only runs.

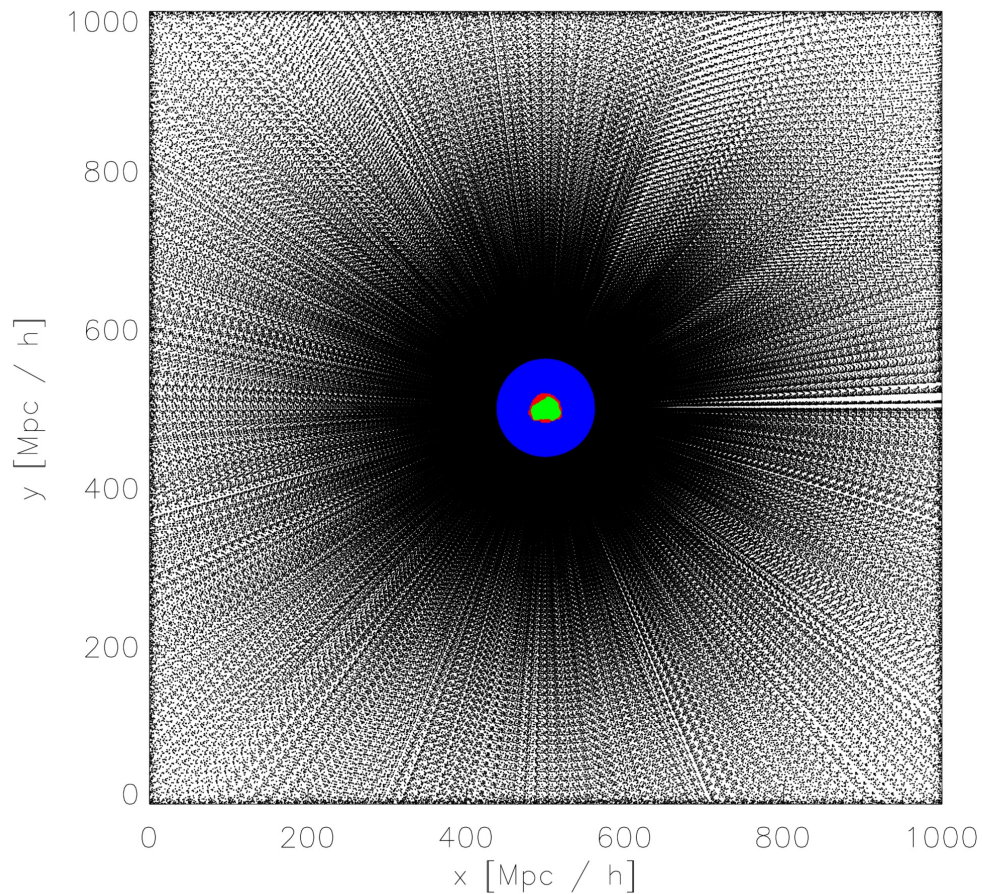


Figure 37: Plotted are all the particles in the initial conditions for the cosmological box g1574117. The green area in the center displays the high resolution gas particles ( $m = 1.56 \cdot 10^8 M_{\odot}$ ), where we expect the cluster to form. The red particles are dark matter particles with good resolution ( $m = 8.44 \cdot 10^8 M_{\odot}$ ). The other colors indicate dark matter particles with resolution decreasing outwards.

## 5.2 Comparison runs with different settings

Having picked and described the initial conditions of the cosmological box we want to simulate, we start with a reference run in which we do not include thermal conduction and neither radiative cooling nor star formation and feedback in order to check, if our code produces reasonable results with this basic configuration. Then we discuss the effects of our different conduction implementations. In subsection 5.2.3 we will include cooling into the picture, to see how this changes the evolution of the magnetic fields and the temperature distribution of the cluster.

Since we need magnetic fields for the anisotropic conduction we include MHD in all of our simulations. The effects of the current MHD implementation onto cluster evolution (and of course test problems) is described for example in [Dolag and Stasyszyn, 2009], therefore we will not discuss this any further in this thesis.

### 5.2.1 Analysing a non-conductive run

For the beginning we have a short look at the evolution of the gas in the cosmological box, which is plotted in figure 38. These six snapshots range from redshift  $z = 3.42$  to the present universe, i.e.  $z = 0$ .<sup>37</sup> Plotted is a mixture of density and temperature using the ray-tracing plotting routine Splotch ([Dolag et al., 2008b]). We can clearly see a cluster evolve in the region with gas particles, but these plots can hardly be used for a quantitative analysis.

Using the SUBFIND module in GADGET ([Springel et al., 2001]), we can automatically identify structures in the run and get virial radii and masses. Depending on the used definition<sup>38</sup> we get an output of  $r_{vir} \approx (1.3 - 2.0) Mpc/h$  and  $M_{vir} \approx (1.8 - 2.8) 10^{15} M_{\odot}$ . One example for the definition is given by [Peterson and Fabian, 2006] as the radius where the density is equal to two hundred times the critical density:

$$r_{vir} = 200 \cdot 3 \frac{H^2}{8\pi G} \quad (5.2.1)$$

<sup>37</sup>the simulation is started at redshift 70.

<sup>38</sup>The virial radius is defined at a point of a certain density, which is a factor (which can vary) times the mean or the critical density. Depending on the used definition one gets different results for the virial radius and all derived quantities.

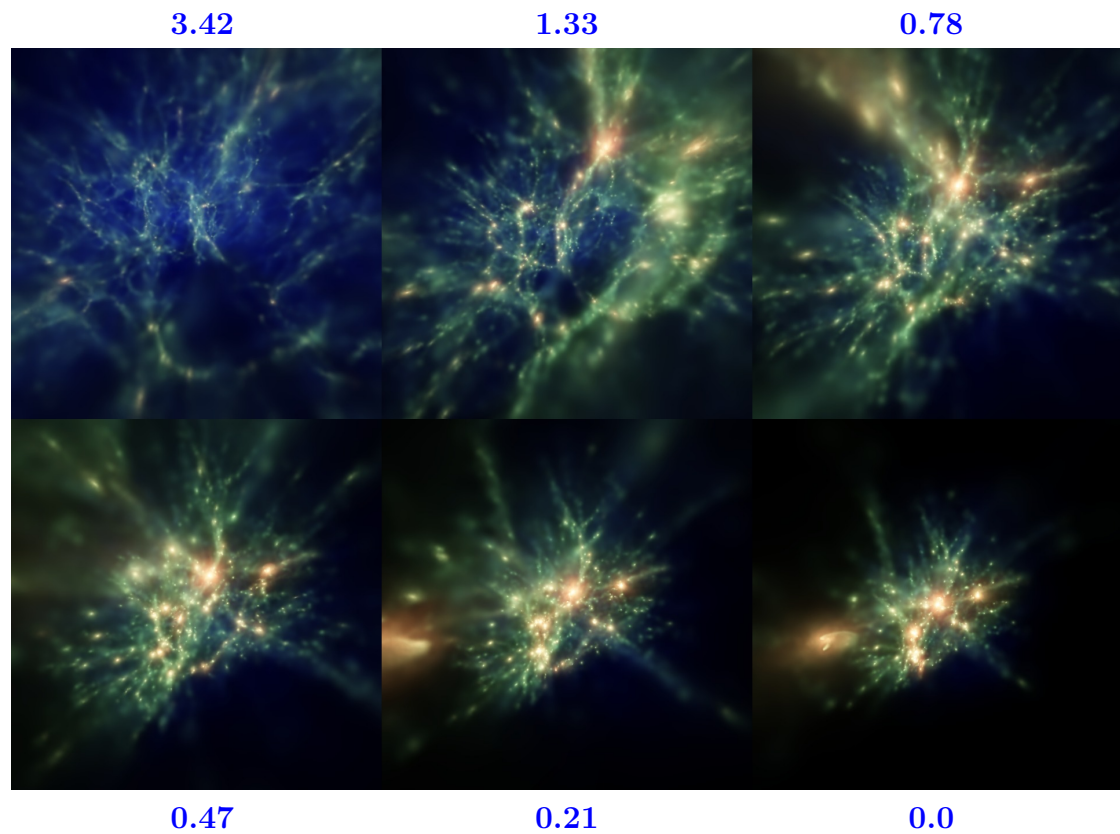


Figure 38: Evolution of g1574117 of the Dianoga sample without cooling, star formation and conduction. Plotted are 6 different snapshots at redshifts given by the blue numbers. Color coded is the internal energy, the intensity is determined by the density. The shown box has a side length of  $40 Mpc$ . The plots have been made using Splotch. [Dolag et al., 2008b]

using the Hubble parameter at redshift  $z$

$$\frac{H}{H_0} = \sqrt{\Omega_m (1+z)^3 + 1 - \Omega_m} \quad (5.2.2)$$

which gives typical virial radii in the range from 1 to 3  $Mpc$  for observed clusters. Therefore our outcomes are right on average.

Compared to most of the clusters in [Bonafede et al., 2011] we produce a comparable virial mass but slightly smaller radius. Still our values fit well enough in the picture to exclude big errors.

As a next step we have a closer look on the magnetic fields and the temperature distribution in this simulation before we rerun it with thermal conduction enabled.

As initial magnetic field we set up a homogeneous distribution described by

$$\vec{B}_{init} \approx \begin{pmatrix} 1.2 \cdot 10^{-8} \\ 0 \\ 0 \end{pmatrix} Gauss \quad (5.2.3)$$

We will not have any closer look at the detailed evolution of the magnetic field, but rather analyse the outcome at redshift  $z = 0$ . For a qualitative overview we have plotted the magnetic field squared over the whole gas region and a zoom in on the central part of the cluster in figure 39. This is a measure of the magnetic pressure which is defined as

$$p_B = \frac{\vec{B}^2}{8\pi} \quad (5.2.4)$$

We can identify several hotspots in the gas with magnetic field strengths up to  $B = 10^{-5} Gauss$ . This matches the observations discussed in section 1.2 very well. The center of the galaxy cluster, which we define via a maximum in the density, contains the strongest magnetic fields in the whole box, since the gas fell down in the potential well dragging magnetic field lines with it and therefore increasing the overall field strengths. The other maxima probably refer to satellite structures, which we will not further investigate here.

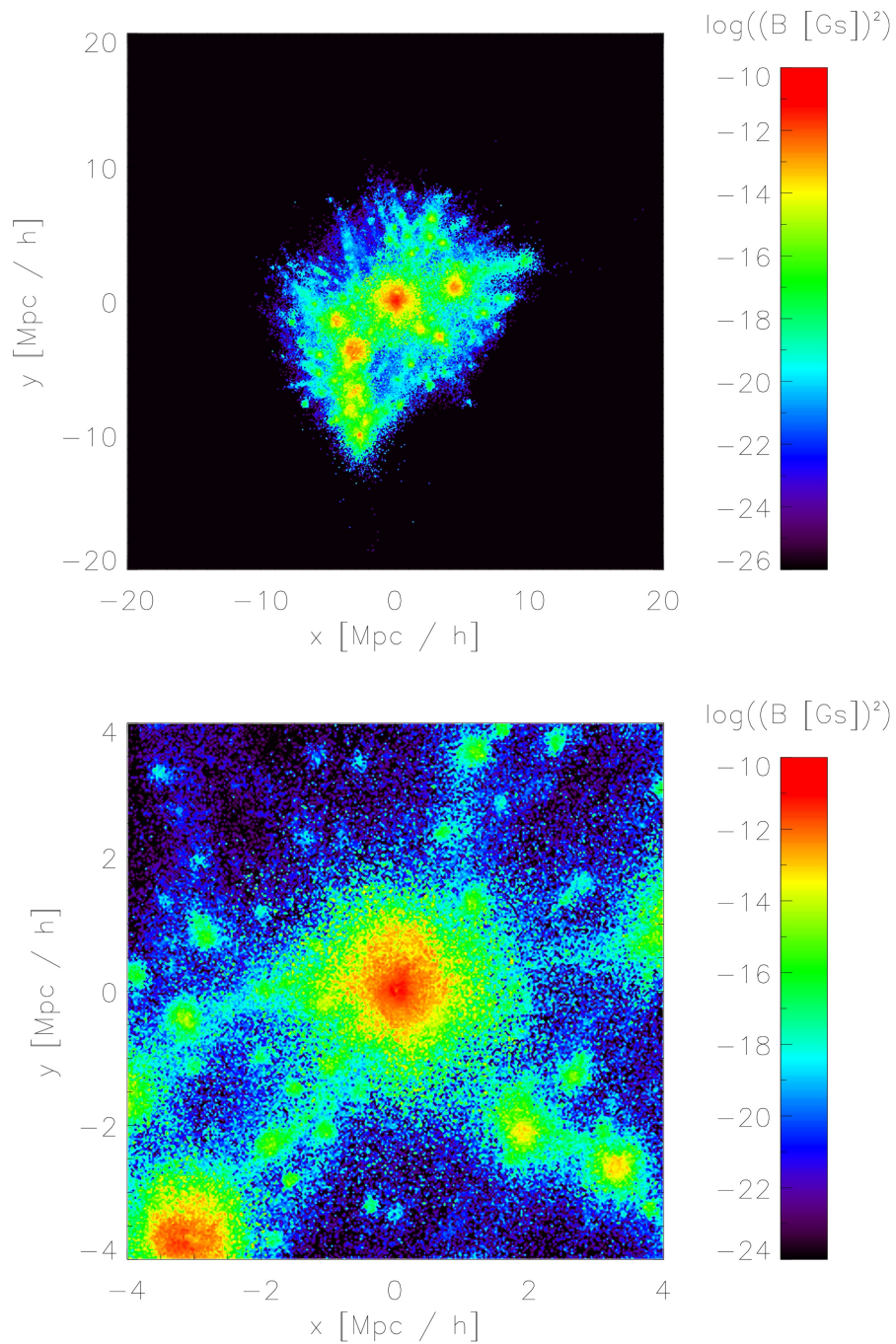


Figure 39: Magnetic pressure map of the cosmological box g1574117 simulated with only basic physics (i.e. no conduction, cooling etc.). Shown is the whole gas in the box and a zoom in the central region.

Please note, that we have used a simple binning algorithm, to generate these maps. Instead of using a fixed slice through the temperature map we kept the number of particles for the averaging process fixed, in order to guarantee reasonable outcomes in high as well as low density regions. Please note that we do not perform a proper SPH averaging<sup>39</sup>, but calculate rather a simple arithmetic mean. This explains, why we see a grained picture especially in the zoom plot. However it provides us with the opportunity to identify small scale structure, which could be washed out by proper SPH smoothing.

In section 2.4 we showed two predictions for the shape of the magnetic fields in a cluster: a power law for both the radial magnetic fields and the tangential component times the inflow velocity. In figure 40 we plotted these quantities for the central part of g1574117 and fitted the two powers laws onto the data points (green lines). We see immediately, that the radial magnetic field component scales indeed as  $B_r \propto r^{-2}$ . We fitted only the inner part until  $2 \text{ Mpc}/h$ , since this is the central region which we can identify as the cluster without any satellites.

For the tangential component of the magnetic field we do not see the predicted power law  $B_t \propto (r \cdot v_{in})^{-1}$  matching at all.

Now let us analyse the properties of the temperature distribution. In figure 41 we show a similar map plot, as for the magnetic pressure above (fig. 39). We see, that the two main regions with high magnetic pressure contain mostly hot gas. However the temperature distribution shows a smoother picture in comparison to the rather isolated magnetic field maxima. The cluster center contains temperatures up to  $10^8 K$  which matches observations very well (please see section 1 for details).

---

<sup>39</sup>I.e. weighting the neighbours with the smoothing kernel while summing over their values.

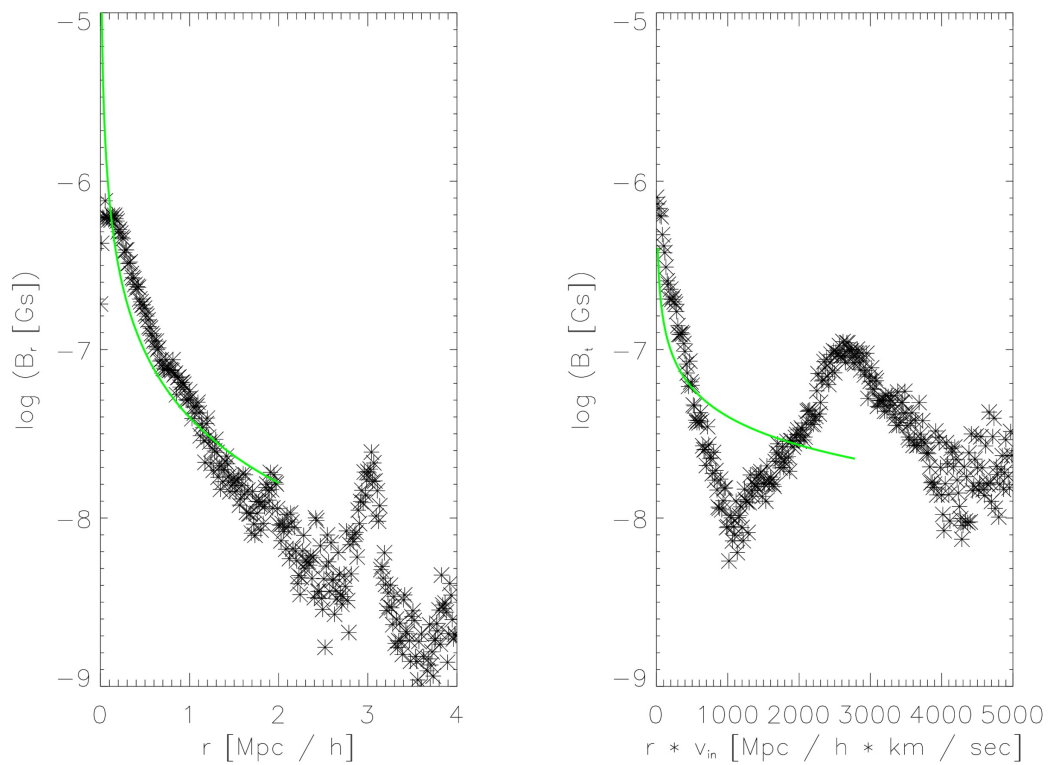


Figure 40: A more quantitative analysis of the magnetic fields in the central region of g1574117.

Left we plotted the radial magnetic field strength against the distance from the center and fitted the predicted behaviour onto the curve in green.

The right plot shows the tangential magnetic field times the inflow velocity against the distance from the center of the cluster. Again we plotted the expected behaviour in green.

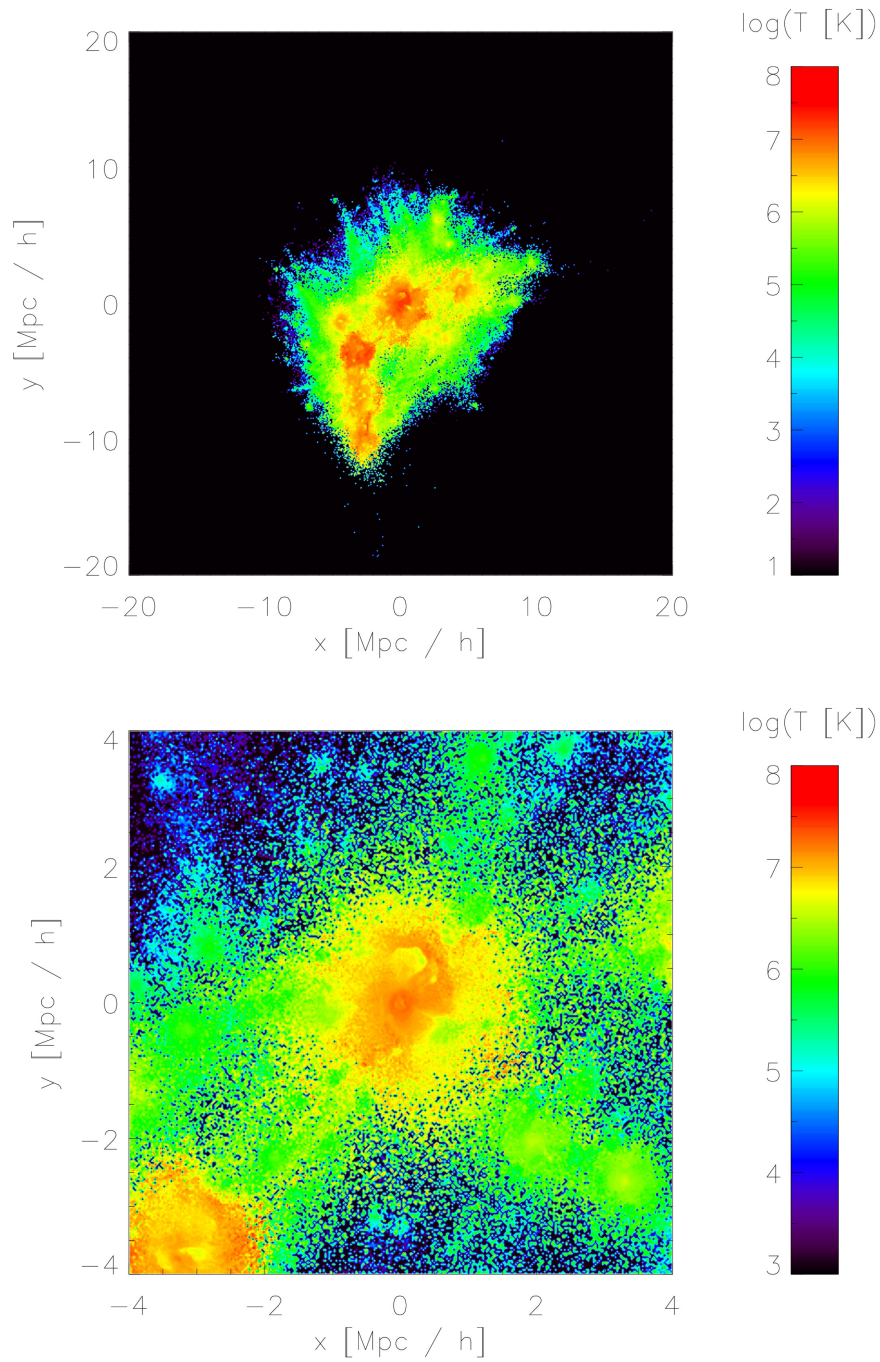


Figure 41: Temperature map of the cosmological box g1574117 simulated with only basic physics. Shown is the whole gas in the box and again a zoom in the central region.

Since this heat map is only a very qualitative plot, we investigate the temperature profile further, by having a closer look at the radial distribution shown in figure 42. For low radii the temperature rises to a peak value of  $2 \cdot 10^7 K$  from which it starts dropping. This is consistent with existing adiabatic simulations by [Jubelgas et al., 2004].

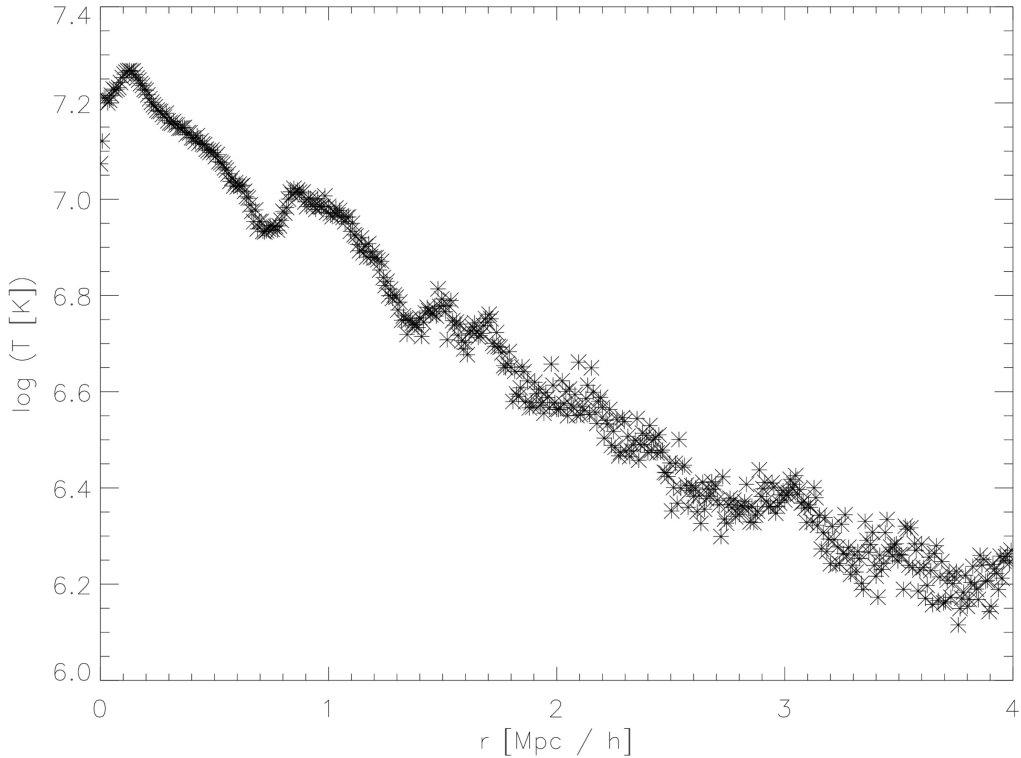


Figure 42: Radial temperature distribution of g1574117. The plot shows very well the expected behaviour, details are discussed in section 5.2.1.

Additionally the temperature should drop by about  $1/3$  at the virial radius, which means we expect a temperature of  $T \approx 5 \cdot 10^6 K$  at a radius of  $r \approx 1.5 Mpc/h$ . The plotted curve shows this behaviour, therefore we conclude that the simulation has produced a successful result.

For a review of measured temperature profiles (amongst others) of clusters versus typical simulation results please see [Borgani et al., 2008]. A comparison with figure 11 in this paper shows, that our results reproduce the expected behaviour pretty well.

Our temperature curve shows an increasing amount of scatter the farther we go out from the cluster center. As we did before with the magnetic field analysis we limit ourself for the inner  $2 Mpc/h$  for reliable results.

In section 2.4 we discussed, that the magnetic pressure should be comparable or even bigger than the thermal pressure in some regions of clusters. To investigate this we define the two ratios

$$\begin{aligned}\beta_{kin} &= \frac{p_{kin}}{p_{mag}} = \frac{nk_B T}{B^2/8\pi} \\ \beta_{therm} &= \frac{p_{therm}}{p_{mag}} = \frac{\rho v^2/2}{B^2/8\pi}\end{aligned}\tag{5.2.5}$$

In figure 43 we plotted the radial dependence of these ratios as well as the magnetic pressure compared to the thermal and the kinetic pressure over the whole box.

We see that the magnetic pressure is much lower than the kinetic and the thermal pressure in most regions of the box at  $z = 0$ . Only in some parts we get a magnetic pressure which exceeds the kinetic component slightly and becomes comparable to the thermal one. Therefore we conclude, that the magnetic field evolution is indeed relevant but in general not dominant for the overall dynamics of the cluster gas.

The analysis of earlier snapshots<sup>40</sup> shows, that this result is stable during the evolution of the cluster. Only in the very beginning we have a way lesser magnetic component which is biased due to our choice for the initial magnetic field.

---

<sup>40</sup>We do not present earlier snapshots here, since they provide hardly any more information.

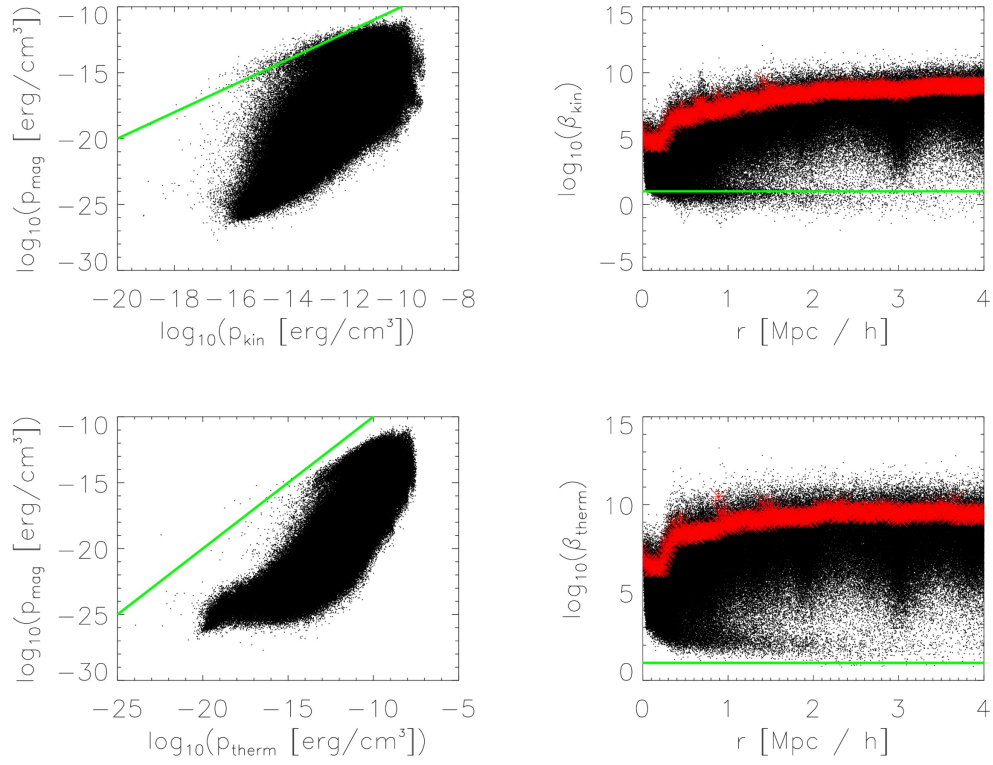


Figure 43: Comparison of the magnetic pressure and the thermal/kinetic pressure for g1574117. Black dots are the values for all particles, while the red stars show indicate the mean values. The green lines indicate, where the plotted pressure components are equal. We see that the magnetic field is in general not the driving factor for the dynamic evolution of the gas, since the magnetic pressure is nearly everywhere smaller than the other two components.

### 5.2.2 Changes due to different conduction implementations

Let us now compare these results to the outcome of simulations with different conduction implementations enabled. These will be

- Isotropic conduction with  $1/3 \cdot \kappa_{Sp}$  as an overall suppression to mimic anisotropic conduction like we argued at the end of section 4.3.1.
- Anisotropic conduction implementation type **3a**: the fully anisotropic approach consistent formulated in one SPH loop. We got overall much better test results with this formulation, than by using implementation type **1** and **2**, therefore we will not use these two approaches any further.
- The similar approach **3b** where we isotropised the equations of **3a** to prevent non physical heat flow to cost of a total suppression of energy transport perpendicular to magnetic fields.

In section 4.2.4 we mentioned, that we could include a physically calculated suppression factor into these implementations instead of assuming a total one. Details how this factor has to be calculated can be found in section 2.2. From our findings about the magnetic field strengths in the last subsection we see immediately, that this suppression will be always close enough to zero, due to it's dependence on the magnetic field, that it would not make any difference to include the proper calculation here. Therefore we will not show any comparison plots regarding this factor and always consider fully suppressed transport of heat orthogonal to magnetic field lines.

The most interesting part is certainly the change of temperatures due to the different conduction schemes.

At first we have a look at the zoomed in temperature maps of all four runs shown in figure 44. We see only very slight differences between those plots. Either this cluster is simply not massive enough to show very different results or our binning algorithm just can not resolve these differences well enough.

To get quantitatively useful results we will have to investigate the radial temperature profiles instead. These are shown in a comparison plot in figure 45, which shows us the different behaviours of the implementations much better.

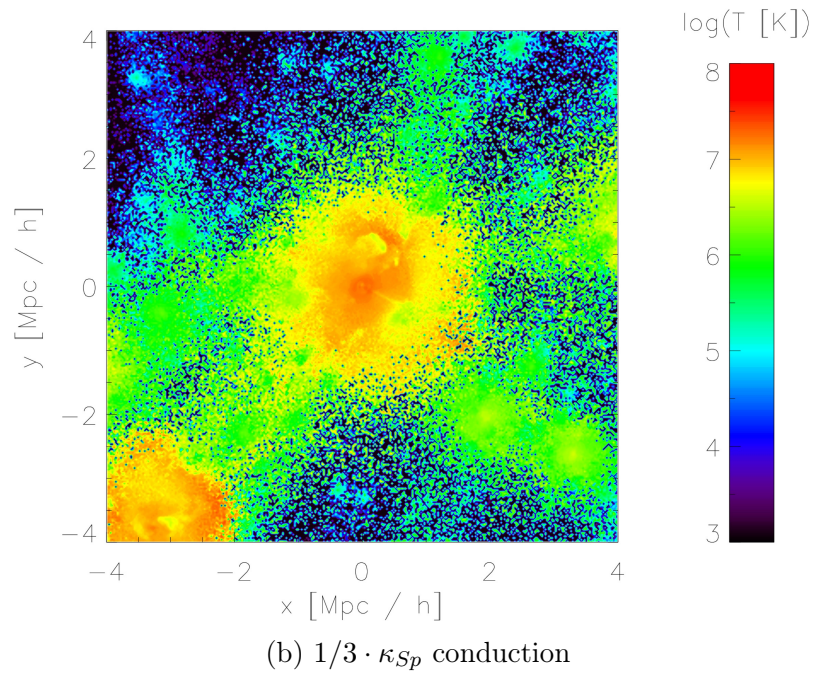
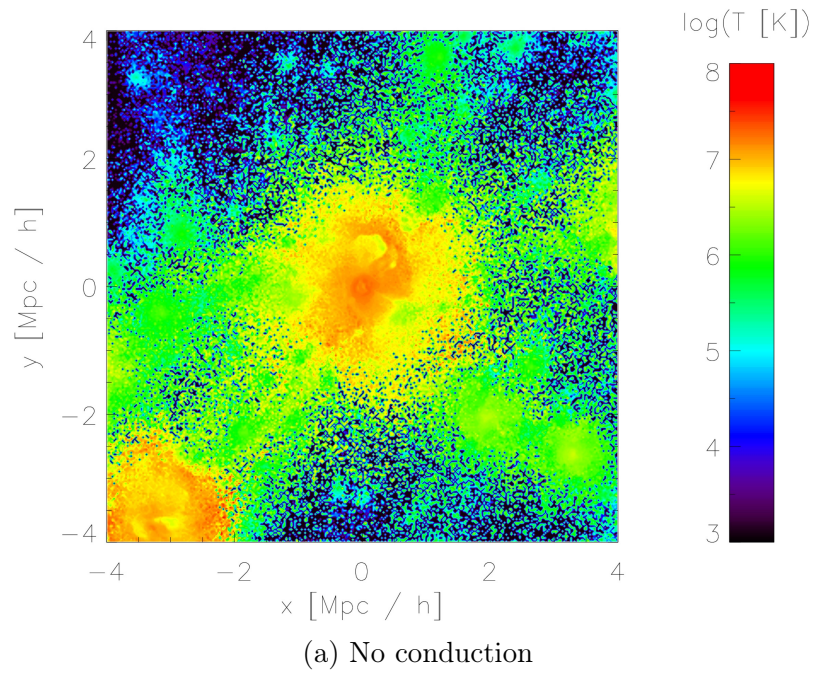


Figure 44: To be continued on the next page.

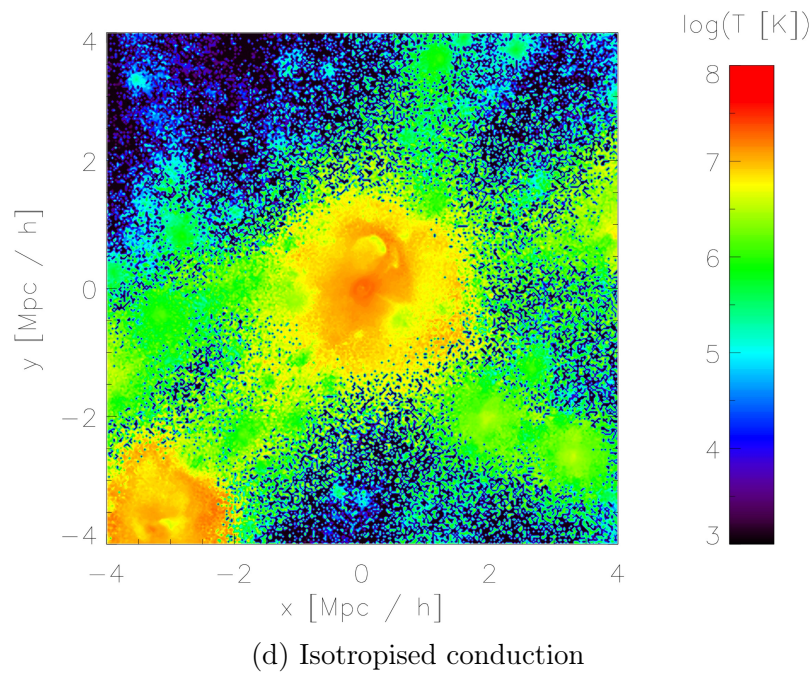
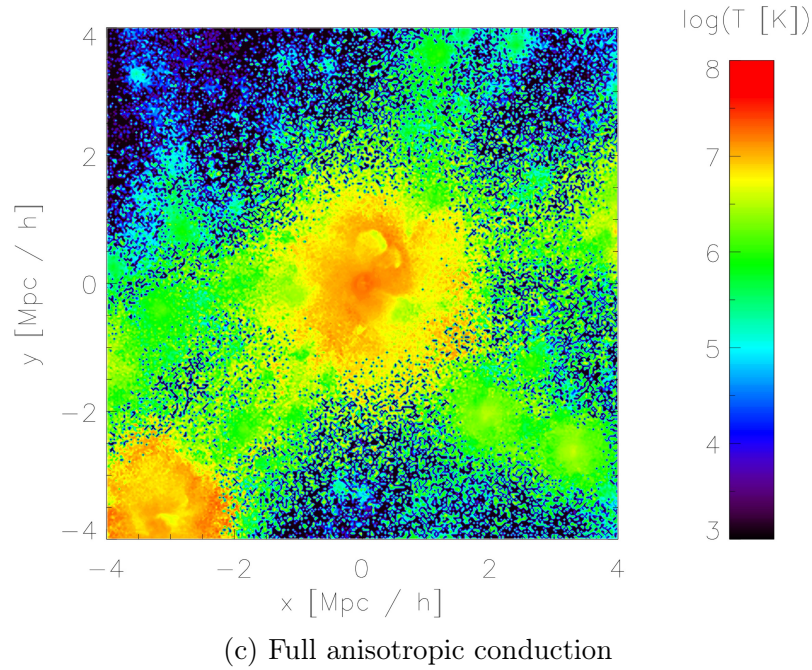


Figure 44: Temperature maps of the central region of g1574117 with four different conduction settings. We can see only very slight differences between the four plots probably due to the map-making algorithm we chose.

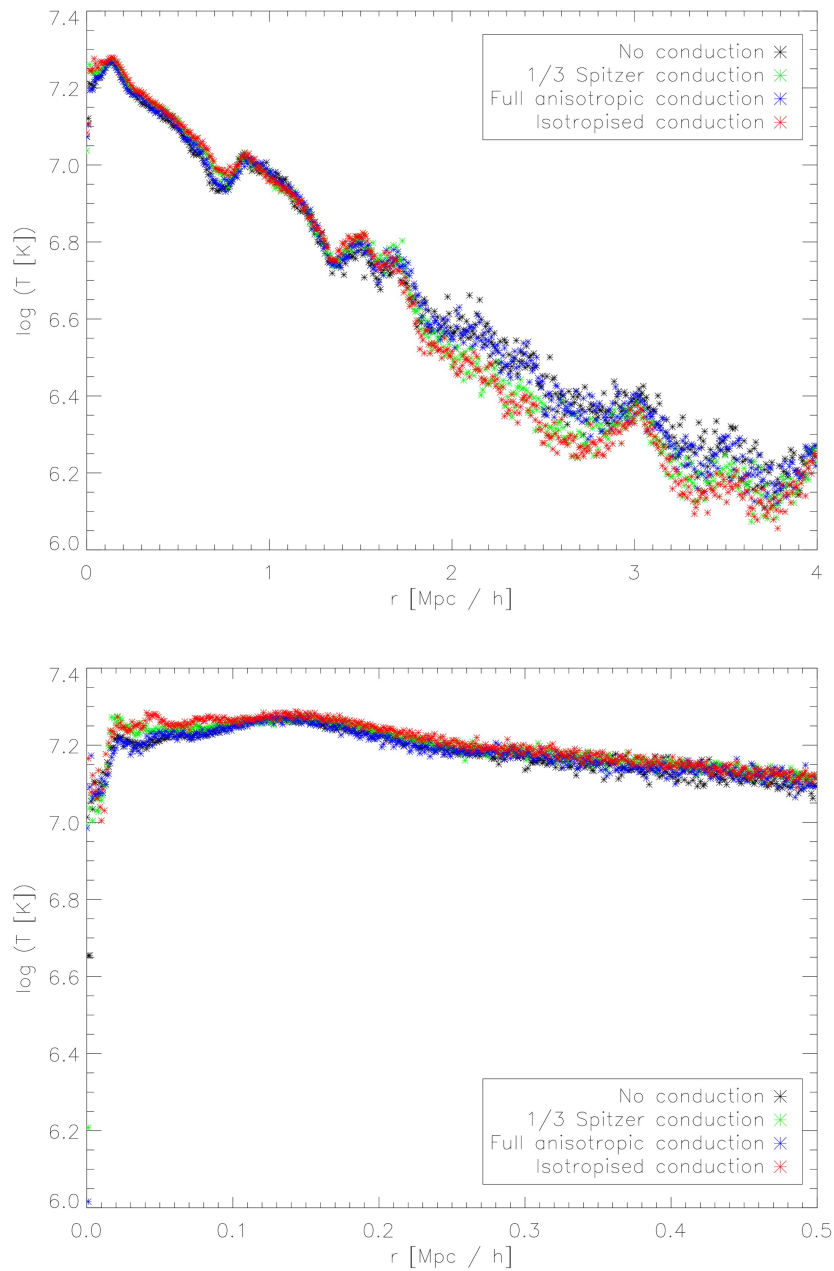


Figure 45: Plotted are the radial temperature distributions of all four runs without cooling and star formation. The lower plot is a zoom in into the very central region of the cluster. One can see clearly the order of the different approaches regarding the net energy transport i.e. how strong conduction is statistically suppressed in each scheme.

However one has to keep in mind, that this galaxy cluster is neither spherical symmetric nor homogeneous. Therefore the radial averaging eliminates the footprint of most substructures in the core part and produces a lot of scatter farther out from the center.

In the upper plot we see, that all four conduction settings produce a similar radial temperature distribution at  $z = 0$ . The net cluster dynamics are not influenced that much, since all the features in the plot stay consistent for all implementations. We can clearly identify how strong the net energy transport of each approach is:

No cond. < Full anisotropic cond. < 1/3 Spitzer cond. < Isotropised cond.

The bigger the net conduction the hotter are the inner parts and cooler are the outer parts of the cluster. This behaviour is consistent with the findings of [Jubelgas et al., 2004]. The turnaround point at which the gas gets colder instead of hotter is about the virial radius  $r = r_{vir}$ .

Let us shortly repeat the problem we wanted to solve with our simulations: Cooling flow models usually result in very high mass deposition rates which lead to expectations of a lot of cold gas in the cluster center. Since observers do not find that much cold gas, we were looking for an additional process which could work against the cooling flow, i.e. heat up the gas in the inner cluster part. With inner parts we do not mean only the very center here, but a more expanded region perhaps up to the virial radius. This is exactly the effect thermal conduction has in our simulations. But we see only a very small impact in this simulation, which is probably not sufficient to offset the cooling flow alone.

Naturally we get less net conduction with an anisotropic implementation, which even lowers the effectiveness of the process. However an anisotropic conduction should prevent a complete washing out of detailed structure in the temperature distribution as is found with an isotropic implementation (see for example [Dolag et al., 2004]). Unfortunately we did not see much change in the substructure of our temperature maps in figure 44 probably due to our map making algorithm and the cluster being not very hot in the inner region.

But before we jump to final conclusions we have to include radiative cooling, star formation and feedback in our simulations, like we will discuss in the next subsection.

### 5.2.3 Adding radiative cooling, star formation and supernova feedback

Now that we compared the effects of different conduction implementations onto adiabatic simulations, we want to include radiative cooling, star formation and supernova feedback into the picture.<sup>41</sup> For a clear identification, we will refer to these runs as "with cooling".

We will discuss the difference between non conductive runs with and without these settings. This has the advantage, that the effect of anisotropic conduction in simulations with cooling can be better analysed separately. Unfortunately we ran into some numerical problems with the existing code, when combining cooling and isotropic conduction. Therefore we will not be able to present this properly in this thesis due to time limitations. Instead we refer to our paper [Arth et al., 2013] (in prep.), where we will discuss this.

In figure 46 we plotted the temperature map from the non conductive run before and as comparison the outcome of the simulation with cooling. One can see that a lot of particles with temperature of about  $10^4 K$  are blown outwards of the compact structure of the cluster and its satellites. Overall the temperature distribution is less peaked in the cluster core but shows rather big isothermal regions. The outer parts of the gas distribution are up to a factor of 10 hotter.

For more quantitative results we have a look at the radial temperature distribution, which is shown in figure 47. We plotted again the temperature distribution up to  $r = 4 Mpc$  as well as a zoom in into the cluster's central region.

This plot agrees with our analysis of the temperature map in the matter, that the gas in the outskirts of the cluster has gotten much hotter and more or less isothermal. What looked as a less peaked core temperature in the less resolved map above, is described by a slightly higher maximal temperature in combination with a more expanded cool core region, as we can see in the zoom plot. This matches again pretty well with the findings of [Jubelgas et al., 2004].

Compared to how much difference thermal conduction made in the last subsection, we see a bigger influence of cooling, star formation and supernova feedback here. Still the combination with conduction could change the picture again quite a bit.

---

<sup>41</sup>Details on the cooling model will be given later in this subsection.

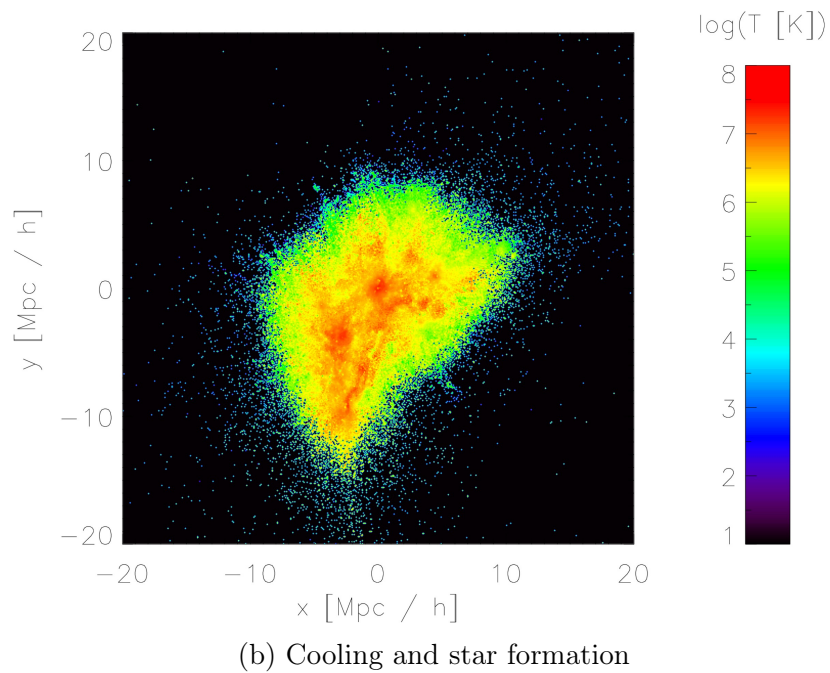
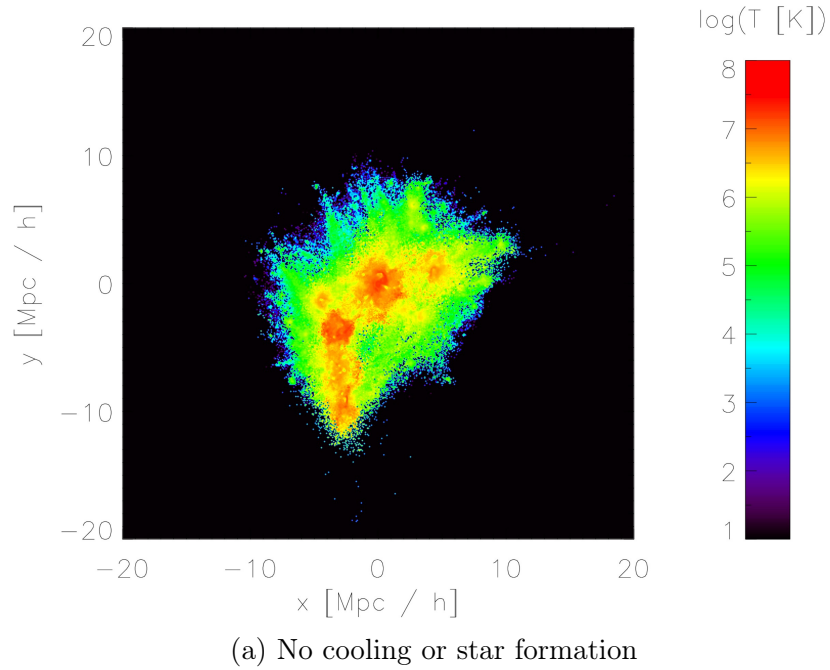


Figure 46: Again the temperature map of the box g1574117 showing simulations with and without cooling. Both runs have been carried out without thermal conduction.

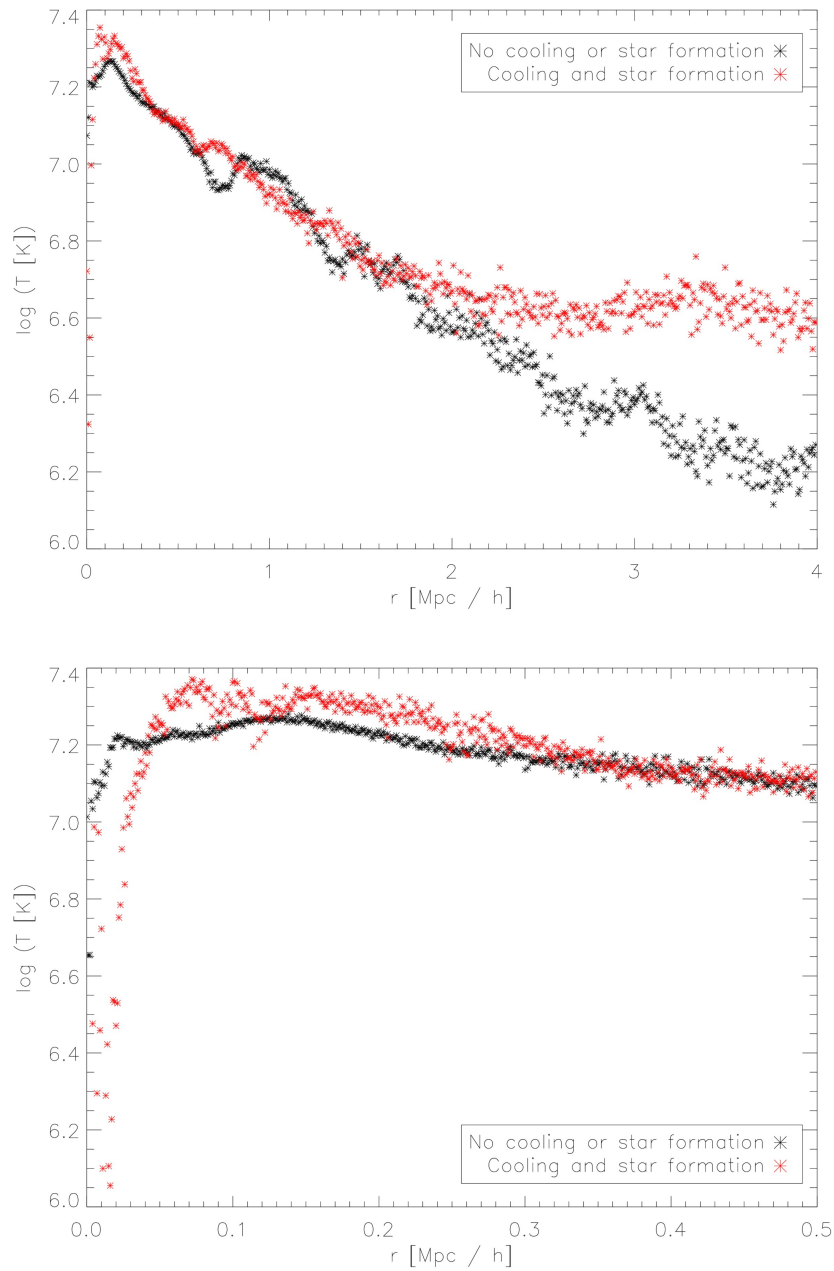


Figure 47: Plotted is the radial temperature distribution for the cluster in box g1574117. The two curves compare the non conductive runs with and without cooling, star formation and feedback. The lower plot shows a zoom in of the very central region.

Now let us have a look at the magnetic field. In figure 48 we plotted the radial magnetic field component again with and without cooling.

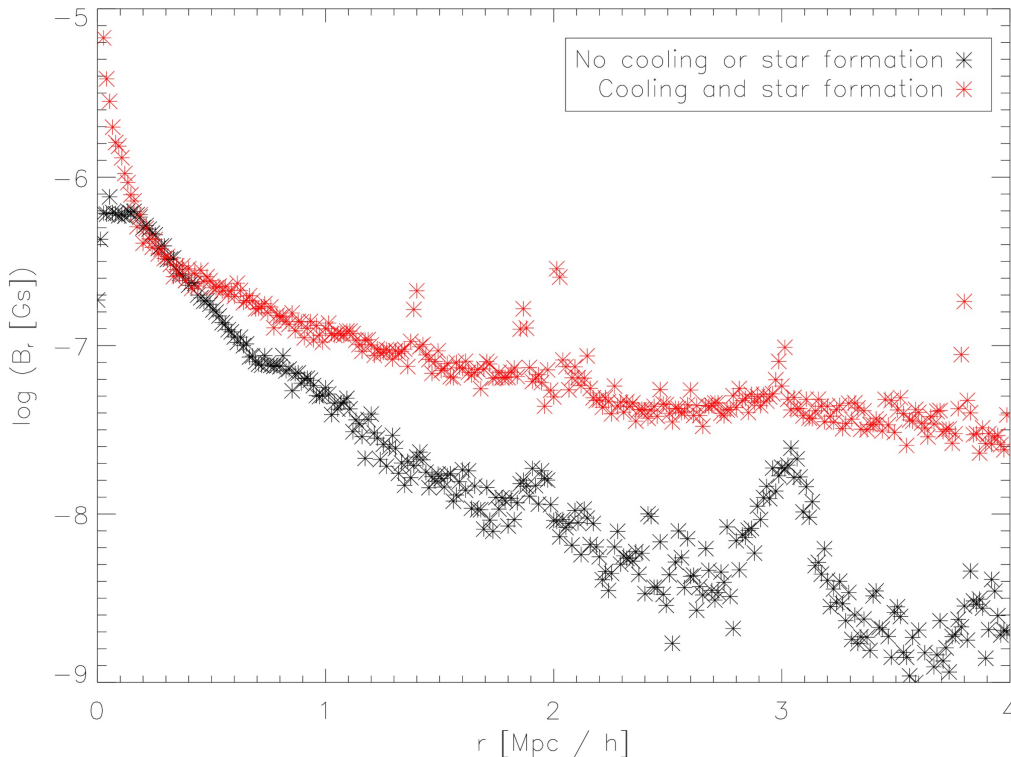


Figure 48: This plot shows the radial component of the magnetic field again as a comparison of non conductive runs with and without cooling.

We see immediately that we get much higher radial magnetic fields in the cooling run than before. The little plateau at small radii ( $r \leq 0.2 \text{ Mpc}/h$ ) is lost, instead the peak rises up to the order of  $10^{-5} \text{ Gauss}$ . This matches the predicted behaviour of  $B_r \propto r^{-2}$  much better than former results in section 5.2.1.

Additionally the peaks we saw earlier are now damped and nearly not visible any more. The overall distribution is now much more homogeneous and shows less scatter.

Now that we have a run which includes radiative cooling, we can do some further analysis on this. In section 1.1 we defined the cooling radius as the radius, where the cooling time equals the age of the universe. The cooling time can be

calculated via equation 1.1.5. It is dependent on the temperature and the number density. Additionally we need the cooling function for this calculation. To calculate the cooling function, like it is used in our code, is rather complicated and goes beyond the scope of this thesis. A detailed description can be found in [Katz et al., 1996].

However for the purpose of showing how this can be done, we try to use the values we can approximately read off of figure 2, which is the high temperature branch of the curve. Therefore we should get at least some reasonable results for the inner region of the cluster. Considering a primordial distribution of hydrogen and helium only, we approximate the plotted curved as

$$\Lambda = 4.75 \cdot 10^{-24} \frac{\text{erg cm}^3}{\text{s}} \cdot \begin{cases} 1 & \text{for } T \leq 2 \cdot 10^6 \text{ K} \\ \left(\frac{T}{2 \cdot 10^6 \text{ K}}\right)^{0.361} & \text{else} \end{cases} \quad (5.2.6)$$

Plugging everything together, we get a relation of the cooling time with the radius as is shown in figure 49.

We marked the condition of the cooling time being equal to the Hubble time and also the first radius where this condition is reached. As one can see we can not really define one precise cooling radius since we still have a lot of fast cooling gas even beyond this point. It is not very surprising that such a large area of different cooling times at different radii is covered, since the cluster is not very homogeneous as we have seen for example in the temperature map plots.

We see, that the cluster core cools extremely fast as well as some other structures in the ICM which can probably be identified as galaxies.

A more detailed analysis of this plot is not reliable, since we used a very approximative cooling function to generate it, where we totally omitted the behaviour of cooling in low temperature regions.

At this point we would like to present further analysis of cooling runs with different conduction implementations. As already mentioned we have to omit this here and refer to [Arth et al., 2013] (in prep.), where we will discuss this.

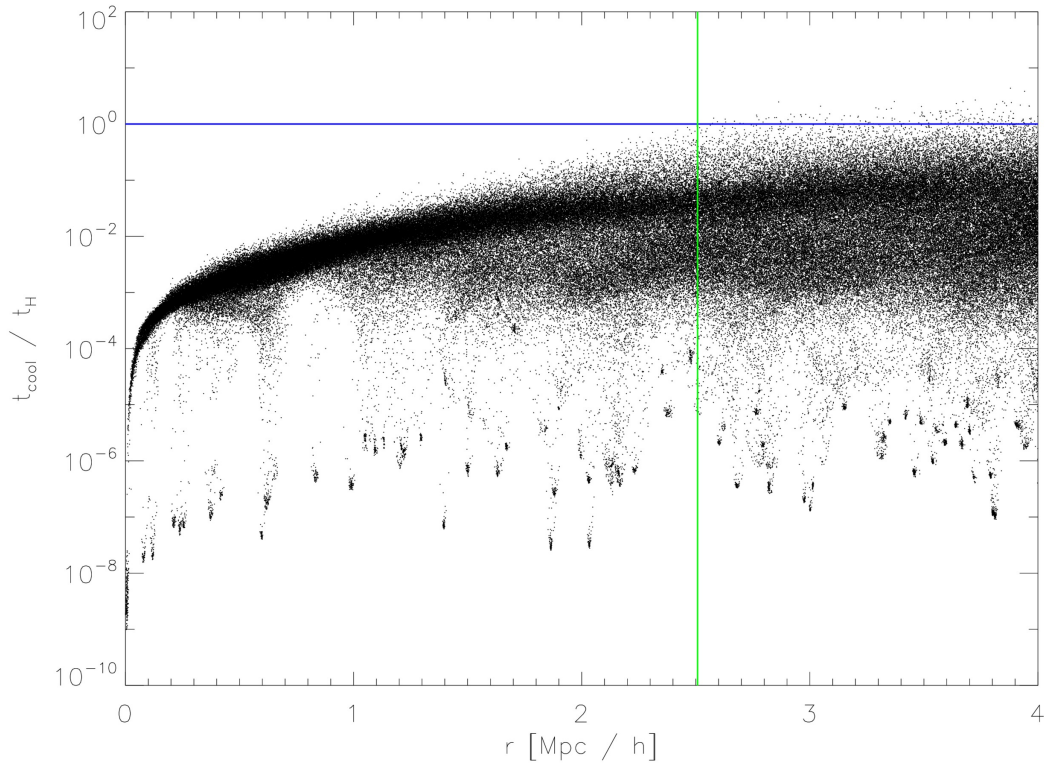


Figure 49: Plotted is the cooling time versus the radius for the inner part of the cosmological box g1574117. The blue horizontal line marks the age of the universe, i.e. the Hubble time, while the green vertical line shows the first radius where  $t = t_H$  is reached.

### 5.3 Comparison to existing simulations with grid codes

Having done some analysis of our new conduction implementations on a cosmological box, we want to compare our results briefly to those of other groups simulating galaxy clusters with grid codes. We will in particular give some reference to exemplary papers about simulations done with ATHENA ([Stone et al., 2008]), FLASH ([Fryxell et al., 2000]) and ENZO ([Bryan and Norman, 1997]).

In general we see, that anisotropic thermal conduction is usually implemented using the same basic approach as we did: aligning the energy transport with the magnetic field lines and eventually calculate a suppression factor perpendicular to the field. Furthermore the grid code implementations have the same problem concerning non physical heat flux, as we did. A solution how this is handled is given in [Sharma and Hammett, 2007] using a heat flux limiter to preserve monotonicity.

Let us start with the results obtained with the ATHENA code. As an example we refer to the work of [Parrish and Stone, 2005], [Bogdanović et al., 2009] and [Avara et al., 2013]. These papers cover a lot of detailed analysis of various properties of the ICM, which we did not discuss in our analysis. An example would be the extensive studies of plasma instabilities, like the **magnetothermal instability** (MTI) or the **heat flux buoyancy instability** (HBI), and their effect on the magnetic field structure and therefore the efficiency of thermal conduction. The mentioned works show that these instabilities are indeed very crucial for the evolution of the magnetic structure in a cluster. [Avara et al., 2013] present 2D simulations to analyse the development and influence of the instabilities separately. However we will not discuss this any further in this thesis.

Additionally the initial choice of the magnetic field's shape seems to have a major influence. [Bogdanović et al., 2009] find, that the resulting cluster can either develop a rather isothermal core or show a catastrophic collapse. Intermediate results are also shown, mostly strongly dependent on the initial conditions. Therefore our results might be strongly biased by the choice of a homogeneous magnetic field in our initial conditions. In total they find, that thermal conduction slows down the cooling process, but can not prevent it.

In the paper of [Ruszkowski et al., 2011] the recent work using FLASH is presented. Again there are studies regarding the growth and influence of plasma instabilities. Similar to our results they find, that radiative cooling has in general a much bigger impact on the temperature distribution of a cluster than thermal conduction. Their simulation result in much hotter central cluster regions, than ours do. Therefore they find a flattening of the inner temperature profile when including conduction, while we find an increase of internal energy. Conduction also offsets cooling a bit, but it is according to this paper not a solution to stop it completely.

Additionally they find an amplification of the magnetic field when including radiative cooling which matches our results very well.

Regarding the most recent work with ENZO on this topic, [Vazza et al., 2010] show many radial temperature distributions for different cluster runs. The overall shape matches our results pretty well, and we see that features like the bumps we got in our results are common to most clusters but very individual. Therefore they are probably not worth to be investigated any further.

[Smith et al., 2013] present the latest cluster simulations with ENZO with focus on thermal conduction. In contrast to the other papers we mentioned, they used only an isotropic implementation but varied the effectiveness of the transport between total suppression and full Spitzer conduction. They find decreasing temperatures with increasing conduction coefficient up to  $r = 3 \cdot r_{200}$ , while we saw this behaviour only for  $r \gtrsim r_{vir}$ . They agree with the previously presented works in the fact, that thermal conduction delays the cooling catastrophe but can not stop it totally.

Summing up, we see that our results are overall consistent with the existing analyses of the effects of anisotropic thermal conduction in cluster evolution. We conclude that a lot more work has to be done, to further study various aspects of the ICM in our simulations.

## 6 Conclusion and Outlook

In this thesis we derived several approaches for implementations of anisotropic thermal conduction into the SPH code GADGET 3. We presented the numerical derivations and discussed the quality of the approaches by using several rather easy test cases. We managed to derive a fully anisotropic conduction scheme as well as a modified version to preserve monotonicity of the heat flux. Afterwards we presented simulations of a cosmological box and analysed the effect of the new schemes compared to isotropic conduction and non conductive runs onto the temperature distribution as well as the evolution of the magnetic fields. We also included a discussion of the effects of cooling, star formation and supernova feedback.

We found that anisotropic conduction has a very similar effect onto our cluster as the isotropic implementation with a corresponding suppression factor. Thermal conduction can delay the cooling of the cluster's core a bit but not completely offset a cooling flow. Therefore we conclude, that thermal conduction alone can not solve the cooling flow problem and prevent gas to cool more and more over time.

However we simulated only one cosmological box, therefore we have no statistics to verify our results. Only a comparison with grid code simulations shows that our results are consistent with recent work about this topic. Nevertheless we have to carry out more simulations and especially study, how anisotropic conduction influences the evolution of bigger clusters. There we should see a much bigger effect to analyse the properties of anisotropic heat conduction in more details.

Additionally we will need to perform much more detailed analyses regarding for example the time evolution of the core temperature and the influence of plasma instabilities.

Furthermore we want to mention, that there are also other applications for our newly developed numerical scheme, which are interesting to study: On the one hand we have rather similar simulations of cooling flows regarding elliptical galaxies instead of clusters ([Binney and Cowie, 1981]). On the other hand there are a lot of completely different topics like the interaction of supernova remnant shocks with interstellar clouds as they are presented in [Orlando et al., 2008].



## 7 List of figures

1	Temperature profile of different clusters . . . . .	2
2	Cooling times for different abundances . . . . .	7
3	Cooling time measurements . . . . .	8
4	Optical image of the <b>Perseus</b> cluster . . . . .	11
5	Multi-wavelength image of <b>NGC 1275</b> . . . . .	12
6	Detailed X-ray image of the <b>Perseus</b> cluster . . . . .	13
7	X-ray spectrum of the <b>Perseus</b> cluster core region . . . . .	14
8	X-ray line emission . . . . .	15
9	Radio observation of the <b>Perseus</b> cluster . . . . .	17
10	Radio observations of <b>Hydra A</b> . . . . .	40
11	Schematics for magnetic flux loops . . . . .	42
12	Different density estimates . . . . .	46
13	Normalisation conditions for cubic kernel in 1D . . . . .	56
14	Normalisation conditions for quintic kernel in 1D . . . . .	57
15	Normalisation conditions for Wendland c6 kernel in 1D . . . . .	59
16	Schematic of test particle setup . . . . .	72
17	Temperature step without magnetic field . . . . .	87
18	Temperature step with 45° magnetic field (implementation <b>1a/b</b> ) . . . . .	89
19	Temperature step with 45° magnetic field (implementation <b>2</b> ) . . . . .	90
20	Temperature step with 45° magnetic field (implementation <b>2</b> ). Later timestep . . . . .	91
21	Temperature step with 45° magnetic field including a flux limiter (implementation <b>2</b> ) . . . . .	92
22	Temperature step with 45° magnetic field (implementation <b>3a</b> ) . . . . .	93
23	Temperature step with 45° magnetic field (implementation <b>3b</b> ) . . . . .	94
24	Temperature step with parallel magnetic field . . . . .	97
25	Temperature step with perpendicular magnetic field . . . . .	99
26	Temperature step with chaotic magnetic field . . . . .	103
27	Sinusoidal zero boundaries test . . . . .	107
28	Sinusoidal periodic test . . . . .	109

29	Sinusoidal periodic test with parallel magnetic field . . . . .	111
30	Sinusoidal periodic test with 45° magnetic field . . . . .	113
31	Sinusoidal periodic test with perpendicular magnetic field . . . . .	115
32	Hot gas bubble without magnetic field . . . . .	118
33	Hot gas bubble with $B_x$ (implementation <b>1a</b> ) . . . . .	119
34	Hot gas bubble with $B_x$ (implementation <b>2</b> ) . . . . .	120
35	Hot gas bubble with $B_x$ (implementation <b>3a</b> ) . . . . .	121
36	Hot gas bubble with $B_x$ (implementation <b>3b</b> ) . . . . .	122
37	Initial particle distribution for g1574117 . . . . .	127
38	Evolution of g1574117 . . . . .	129
39	Magnetic pressure map of g1574117 . . . . .	131
40	Magnetic fields in g1574117 . . . . .	133
41	Temperature map of g1574117 . . . . .	134
42	Radial temperature distribution of g1574117 . . . . .	135
43	Pressure comparison of g1574117 . . . . .	137
44	Temperature maps of g1574117: different conduction schemes . . .	139
45	Radial temperature distribution for g1574117: different conduction schemes . . . . .	141
46	Temperature map of g1574117: cooling and star formation . . . . .	144
47	Radial temperature distribution for g1574117: cooling and star for- mation . . . . .	145
48	Radial magnetic field distribution for g1574117: cooling and star formation . . . . .	146
49	Cooling times of g1574117 . . . . .	148

## Appendices

50	Complex integration path . . . . .	C2
----	------------------------------------	----

## 8 Sources

[ast, 2013] (2013). AstronomyOnline.org Cosmology - Galaxies, <http://astronomyonline.org/Cosmology/Galaxies.asp>. 06.10.2013.

[Aghanim et al., 2013] Aghanim, N., Arnaud, M., Ashdown, M., Aumont, J., Bacigalupi, C., Banday, A. J., Barreiro, R. B., Bartlett, J. G., Battaner, E., Benabed, K., Bersanelli, M., Bielewicz, P., Bobin, J., Bock, J. J., Bonaldi, A., Bond, J. R., Borrill, J., Bouchet, F. R., Bridges, M., Bucher, M., Burigana, C., Butler, R. C., Calabrese, E., Cappellini, B., Catalano, A., Challinor, A., Chamballu, A., Chen, X., Chiang, H. C., Christensen, P. R., Church, S., Clements, D. L., Colombi, S., Colombo, L. P. L., Couchot, F., Coulais, A., Crill, B. P., Curto, A., Cuttaia, F., Danese, L., Davies, R. D., Davis, R. J., Bernardis, P. D., Rosa, A. D., Zotti, G. D., Delabrouille, J., Dickinson, C., Diego, J. M., Dolag, K., Dole, H., Donzelli, S., Douspis, M., Dunkley, J., Dupac, X., Efstathiou, G., Elsner, F., Eriksen, H. K., Finelli, F., Forni, O., Frailis, M., Fraisse, A. A., Franceschi, E., Gaier, T. C., Galeotta, S., Galli, S., Ganga, K., Giard, M., Giardino, G., Gratton, S., Gregorio, A., Gruppuso, A., Gudmundsson, J. E., Haissinski, J., Hamann, J., Hansen, F. K., Hanson, D., Harrison, D., Herranz, D., Hildebrandt, S. R., Hivon, E., Hobson, M., Holmes, W. A., Hornstrup, A., Hou, Z., Hovest, W., Jewell, J., Jones, W. C., Juvela, M., Keskitalo, R., Kisner, T. S., Kneissl, R., Knoche, J., Knox, L., Kunz, M., Lagache, G., Lasenby, A., Lattanzi, M., Laureijs, R. J., Lawrence, C. R., Leach, S., Leahy, J. P., Leonardi, R., Lesgourgues, J., Lewis, A., Liguori, M., Lilje, P. B., Lubin, P. M., Maino, D., Mandolesi, N., Maris, M., Marshall, D. J., and Martin, P. G. (2013). Planck 2013 results. XVI. Cosmological parameters.

[Arth et al., 2013] Arth, A., Dolag, K., Beck, A., Petkova, M., and Lesch, H. (2013). Anisotropic thermal conduction in Gadget. *in prep.*

[Avara et al., 2013] Avara, M. J., Reynolds, C. S., and Bogdanović, T. (2013). Role of magnetic field strength and numerical resolution in simulations of the heat-flux driven buoyancy instability.

- [Binney and Cowie, 1981] Binney, J. and Cowie, L. L. (1981). X-Ray Emission from M87: A Pressure Confined Cooling Atmosphere Surrounding a Low Mass Galaxy. *The Astrophysical Journal*, 247(1):247.
- [Bogdanović et al., 2009] Bogdanović, T., Reynolds, C. S., Balbus, S. A., and Parrish, I. J. (2009). Simulations of Magnetohydrodynamics Instabilities in Intra-cluster Medium Including Anisotropic Thermal Conduction. *The Astrophysical Journal*, 704(1):211–225.
- [Bonafede, 2010] Bonafede, A. (2010). *Magnetic Fields in Galaxy Clusters: Faraday Rotation and Thermal Emission*. PhD thesis.
- [Bonafede et al., 2011] Bonafede, A., Dolag, K., Stasyszyn, F. A., Murante, G., and Borgani, S. (2011). A non-ideal magnetohydrodynamic gadget: simulating massive galaxy clusters. *Monthly Notices of the Royal Astronomical Society*, 418(4):2234–2250.
- [Borgani et al., 2008] Borgani, S., Diaferio, A., Dolag, K., and Schindler, S. (2008). Thermodynamical Properties of the ICM from Hydrodynamical Simulations. *Space Science Reviews*, 134(1-4):269–293.
- [Bregman and David, 1989] Bregman, J. N. and David, L. P. (1989). Alternative Models of Cooling Flows. *The Astrophysical Journal*, 341:49–53.
- [Bronstein et al., 2008] Bronstein, I. N., Semendjajew, K. A., Muisol, G., and Muehlig, H. (2008). *Taschenbuch der Mathematik*. Harri Deutsch Verlag.
- [Bryan and Norman, 1997] Bryan, G. L. and Norman, M. L. (1997). Simulating X-Ray Clusters with Adaptive Mesh Refinement. In *12th Kingston meeting: Computational Astrophysics*.
- [Chandran and Cowley, 1998] Chandran, B. and Cowley, S. (1998). Thermal Conduction in a Tangled Magnetic Field. *Physical Review Letters*, 80(14):3077–3080.
- [Cleary and Monaghan, 1999] Cleary, P. W. and Monaghan, J. J. (1999). Conduction Modelling Using Smoothed Particle Hydrodynamics. *Journal of Computational Physics*, 148(1):227–264.

- [Cowie and McKee, 1977] Cowie, L. L. and McKee, C. F. (1977). The Evaporation of Spherical Clouds in a Hot Gas. I. Classical and Saturated Mass Loss Rates. *The Astrophysical Journal*, 211:135–146.
- [Dehnen and Aly, 2012] Dehnen, W. and Aly, H. (2012). Improving convergence in smoothed particle hydrodynamics simulations without pairing instability. *Monthly Notices of the Royal Astronomical Society*, 1082.
- [Dolag et al., 2008a] Dolag, K., Borgani, S., Schindler, S., Diaferio, A., and Bykov, a. M. (2008a). Simulation Techniques for Cosmological Simulations. *Space Science Reviews*, 134(1-4):229–268.
- [Dolag et al., 2004] Dolag, K., Jubelgas, M., Springel, V., Borgani, S., and Rasia, E. (2004). Thermal Conduction in Simulated Galaxy Clusters. *The Astrophysical Journal*, 606(2):2000–2003.
- [Dolag et al., 2008b] Dolag, K., Reinecke, M., Gheller, C., and Imboden, S. (2008b). Splotch: visualizing cosmological simulations. *New Journal of Physics*, 10(12):125006.
- [Dolag and Stasyszyn, 2009] Dolag, K. and Stasyszyn, F. A. (2009). An MHD gadget for cosmological simulations. *Monthly Notices of the Royal Astronomical Society*, 398(4):1678–1697.
- [Fabian, 1994] Fabian, A. C. (1994). Cooling Flows in Clusters of Galaxies. *Annual Review of Astronomy and Astrophysics*, 32(1):277–318.
- [Fabian, 2002] Fabian, A. C. (2002). Cooling flows in Clusters of Galaxies. In *Lighthouses of the Universe: The Most Luminous Celestial Objects and Their Use for Cosmology*.
- [Fabian et al., 1981] Fabian, A. C., Hu, E. M., Cowie, L. L., and Grindlay, J. (1981). The distribution and morphology of X-ray-emitting gas in the core of the Perseus cluster. *Astrophysical Journal*, 248:47–54.
- [Fabian et al., 2003] Fabian, A. C., Sanders, J. S., Allen, S. W., Crawford, C. S., Iwasawa, K., Johnstone, R. M., Schmidt, R. W., and Taylor, G. B. (2003). A deep Chandra observation of the Perseus cluster: shocks and ripples. *Monthly Notices of the Royal Astronomical Society*, 344(3):L43–L47.

- [Fabian et al., 2006] Fabian, A. C., Sanders, J. S., Taylor, G. B., Allen, S. W., Crawford, C. S., Johnstone, R. M., and Iwasawa, K. (2006). A very deep Chandra observation of the Perseus cluster: shocks, ripples and conduction. *Monthly Notices of the Royal Astronomical Society*, 366(2):417–428.
- [Flynn, 2006] Flynn, C. (2006). Astrophysics II, Lecture 3: Accelerated charges and bremsstrahlung, <http://www.astro.utu.fi/~cflynn/astroII/>. 23.04.2013.
- [Frank-Kamenezki, 1967] Frank-Kamenezki, D. A. (1967). *Vorlesungen über Plasmaphysik*. VEB Deutscher Verlag der Wissenschaften.
- [Fryxell et al., 2000] Fryxell, B., Olson, K., Ricker, P., Timmes, F. X., Zingale, M., Lamb, D., MacNeice, P., Rosner, R., Truran, J., and Tufo, H. (2000). FLASH: An Adaptive Mesh Hydrodynamics Code for Modeling Astrophysical Thermonuclear Flashes. *The Astrophysical Journal Supplement Series*, 131(1).
- [Golant et al., 1980] Golant, V. E., Zhilinsky, A. P., and Sakharov, I. E. (1980). *Fundamentals of Plasma Physics*.
- [Huba, 2011] Huba, J. D. (2011). NRL PLASMA FORMULARY Supported by The Office of Naval Research.
- [Jubelgas et al., 2004] Jubelgas, M., Springel, V., and Dolag, K. (2004). Thermal conduction in cosmological SPH simulations. *Monthly Notices of the Royal Astronomical Society*, 351(2):423–435.
- [Katz et al., 1996] Katz, N., Weinberg, D. H., and Hernquist, L. (1996). Cosmological Simulations with TreeSPH. *Astrophysical Journal Supplement*, 105.
- [Komarov et al., 2013] Komarov, S., Churazov, E., and Schekochihin, A. (2013). Suppression of local heat flux in a turbulent magnetized intracluster medium. page 10.
- [Kronberg, 1994] Kronberg, P. P. (1994). Extragalactic magnetic fields. *Reports on Progress in Physics*, 57(4):325–382.

- [Landau and Lifschitz, 2007] Landau, L. D. and Lifschitz, E. M. (2007). *Lehrbuch der theoretischen Physik VI Hydrodynamik*. Harri Deutsch GmbH, Moskau, 5th edition.
- [Loeb, 2002] Loeb, A. (2002). Are X-ray clusters cooled by heat conduction to the surrounding intergalactic medium? *New Astronomy*, 7(6):279–282.
- [McGraw-Hill Companies, 2013] McGraw-Hill Companies (2013). McGraw-Hill Dictionary of Scientific & Technical Terms, <http://encyclopedia2.thefreedictionary.com/Lorentz+gas>. 26.04.2013.
- [Meiksin, 1990] Meiksin, A. (1990). A Non-Steady Cooling Flow Model for NGC 1275 (Perseus). In *Evolution of the universe of galaxies; Proceedings of the Edwin Hubble Centennial Symposium*, Berkeley. Astronomical Society of the Pacific.
- [Monaghan, 1992] Monaghan, J. J. (1992). Smoothed Particle Hydrodynamics. *Annual Review of Astronomy and Astrophysics*, 30(1):543–574.
- [Narayan and Medvedev, 2001] Narayan, R. and Medvedev, M. V. (2001). Thermal Conduction in Clusters of Galaxies. *The Astrophysical Journal*, pages 129–132.
- [Orlando et al., 2008] Orlando, S., Bocchino, F., Reale, F., Peres, G., and Pagano, P. (2008). The importance of magnetic-field-oriented thermal conduction in the interaction of snr shocks with interstellar clouds. *The Astrophysical Journal*, 678(1):274–286.
- [Owers et al., 2011] Owers, M. S., Nulsen, P. E. J., and Couch, W. J. (2011). Minor Merger-Induced Cold Fronts in Abell 2142 and Rxj1720.1+2638. *The Astrophysical Journal*, 741(2):122.
- [Owers et al., 2009] Owers, M. S., Nulsen, P. E. J., Couch, W. J., and Markevitch, M. (2009). A High Fidelity Sample of Cold Front Clusters From the Chandra Archive. *The Astrophysical Journal*, 704(2):1349–1370.
- [Parrish and Stone, 2005] Parrish, I. J. and Stone, J. M. (2005). Nonlinear Evolution of the Magnetothermal Instability in Two Dimensions. *The Astrophysical Journal*, 633(1):334–348.

- [Peterson and Fabian, 2006] Peterson, J. R. and Fabian, A. C. (2006). X-ray spectroscopy of cooling clusters. *Physics Reports*, 427(1):1–39.
- [Peterson et al., 2003] Peterson, J. R., Kahn, S. M., Paerels, F. B. S., Kaastra, J. S., Tamura, T., Bleeker, J. A. M., Ferrigno, C., and Jennigan, J. (2003). High-Resolution X-Ray Spectroscopic Constraints on Cooling-Flow Models for Clusters of Galaxies. *The Astrophysical Journal*, 590(1):207–224.
- [Petkova and Springel, 2009] Petkova, M. and Springel, V. (2009). An implementation of radiative transfer in the cosmological simulation code gadget. *Monthly Notices of the Royal Astronomical Society*, 396(3):1383–1403.
- [Pfenniger and Combes, 1994] Pfenniger, D. and Combes, F. (1994). Is dark matter in spiral galaxies cold gas? II. Fractal models and star non-formation. *Astronomy and Astrophysics*, 285:94–118.
- [Pistinner and Shaviv, 1996] Pistinner, S. and Shaviv, G. (1996). Can tangled magnetic fields suppress thermal conduction in cluster cooling flows? *The Astrophysical Journal*, 459:147–155.
- [Price, 2012] Price, D. J. (2012). Smoothed particle hydrodynamics and magnetohydrodynamics. *Journal of Computational Physics*, 231(3):759–794.
- [Rechester and Rosenbluth, 1978] Rechester, A. B. and Rosenbluth, M. (1978). Electron heat transport in a Tokamak with destroyed magnetic surfaces. *Physical Review Letters*, 40(1):38–41.
- [Rosner and Tucker, 1989] Rosner, R. and Tucker, W. H. (1989). On Magnetic Fields, Heating And Thermal Conduction In Halos, And The Suppression Of Cooling Flows. *The Astrophysical Journal*, 338:761–769.
- [Ruszkowski et al., 2011] Ruszkowski, M., Lee, D., Brüggén, M., Parrish, I. J., and Oh, S. P. (2011). Cosmological Magnetohydrodynamic Simulations of Cluster Formation With Anisotropic Thermal Conduction. *The Astrophysical Journal*, 740(2):81.
- [Saad, 2000] Saad, Y. (2000). *Iterative Methods for Sparse Linear Systems*. 2nd edition.

- [Salomé and Combes, 2003] Salomé, P. and Combes, F. (2003). Cold molecular gas in cooling flow clusters of galaxies. *Astronomy and Astrophysics*, 667:657–667.
- [Sarazin, 1986] Sarazin, C. (1986). *X-ray emission from clusters of galaxies*, volume 58.
- [Sarazin, 2008] Sarazin, C. (2008). *Gas Dynamics in Clusters of Galaxies*.
- [Schneider, 2008] Schneider, P. (2008). *Einführung in die Extragalaktische Astronomie und Kosmologie*. Springer Berlin Heidelberg New York, 1st (corrected) edition.
- [Sharma and Hammett, 2007] Sharma, P. and Hammett, G. W. (2007). Preserving monotonicity in anisotropic diffusion. *Journal of Computational Physics*, 227(1):123–142.
- [Smith et al., 2013] Smith, B., Voit, G. M., Ventimiglia, D., and Skillman, S. W. (2013). Cosmological simulations of isotropic conduction in galaxy clusters.
- [Soker, 1997] Soker, N. (1997). Magnetic Fields and Inflow in Cluster Cooling Flows. In *Galactic Cluster Cooling Flows. ASP Conference Series*, page 182, Haifa at Oranim.
- [Soker, 2010] Soker, N. (2010). Magnetic fields in cooling flow clusters: a critical view. In *Galaxy Clusters*, pages 1–22, Garching.
- [Soker and Sarazin, 1990] Soker, N. and Sarazin, C. (1990). The Role of Magnetic Fields in Cluster Cooling Flows. *The Astrophysical Journal*, 348:73–84.
- [Soker et al., 2001] Soker, N., White, R. E. I., David, L. P., and McNamara, B. R. (2001). A moderate cluster cooling flow model. *The Astrophysical Journal*, 549:832–839.
- [Spitzer, 1956] Spitzer, L. J. (1956). *Physics of fully ionized gas*. Interscience Publishers.
- [Spitzer and Härm, 1953] Spitzer, L. J. and Härm, R. (1953). Transport Phenomena in a Completely Ionized Gas. *Physical Review Letters*, 89(5):977–981.

- [Springel, 2005a] Springel, V. (2005a). The cosmological simulation code GADGET-2. *Monthly Notices of the Royal Astronomical Society*, 364(4):1105–1134.
- [Springel, 2005b] Springel, V. (2005b). User guide for GADGET-2. pages 1–46.
- [Springel, 2010] Springel, V. (2010). Smoothed Particle Hydrodynamics in Astrophysics. *Annual Review of Astronomy and Astrophysics*, 48(1):391–430.
- [Springel et al., 2001] Springel, V., White, S. D. M., Tormen, G., and Kauffmann, G. (2001). Populating a cluster of galaxies – I . Results at  $z = 0$ . *Monthly Notices of the Royal Astronomical Society*, 328(3):726–750.
- [Stone et al., 2008] Stone, J. M., Gardiner, T. a., Teuben, P., Hawley, J. F., and Simon, J. B. (2008). Athena: A New Code for Astrophysical MHD. *The Astrophysical Journal Supplement Series*, 178(1):137–177.
- [Taylor et al., 2006] Taylor, G. B., Gugliucci, N. E., Fabian, A. C., Sanders, J. S., Gentile, G., and Allen, S. W. (2006). Magnetic fields in the centre of the Perseus cluster. *Monthly Notices of the Royal Astronomical Society*, 368(4):1500–1506.
- [Taylor et al., 1990] Taylor, G. B., Perley, R. A., Inoue, M., Kato, T., Tabara, H., and Aizu, K. (1990). VLA Observations of the Radio Galaxy Hydra A (3C 218). *The Astrophysical Journal*, 360:41–54.
- [Vazza et al., 2010] Vazza, F., Brunetti, G., Gheller, C., and Brunino, R. (2010). Massive and refined: a sample of large galaxy clusters simulated at high resolution. I:Thermal gas and properties of shock waves.
- [Voigt and Fabian, 2004] Voigt, L. M. and Fabian, A. C. (2004). Thermal conduction and reduced cooling flows in galaxy clusters. *Monthly Notices of the Royal Astronomical Society*, 347(4):1130–1149.
- [Zakamska and Narayan, 2003] Zakamska, N. L. and Narayan, R. (2003). Models of Galaxy Clusters with Thermal Conduction. *The Astrophysical Journal*, 582:162–169.

## Appendix A The Conjugate Gradient Method

### Isotropic formulation

As mentioned in section 4.1, we want to solve equation 4.1.13 with the conjugate gradient method. For detailed information about the mathematical properties of the integrator please see [Saad, 2000]. In the following derivation we basically follow [Petkova and Springel, 2009].

For simplicity we use a formulation with specific internal energy:

$$\frac{du_i}{dt} = \frac{\mu(\gamma - 1)}{k_B} \sum_j \frac{\kappa_{ij} m_j}{\rho_i \rho_j} \frac{\vec{x}_{ij} \cdot \nabla_i W_{ij}}{|\vec{x}_{ij}|^2} (u_i - u_j) \quad (\text{A.1})$$

At first we need to discretize the timestep in this equation, by using

$$\frac{du_i}{dt} \rightarrow \frac{\Delta u_i}{\Delta t} = \frac{u_i^{n+1} - u_i^n}{\Delta t} \quad (\text{A.2})$$

where the super-index denotes to which timestep the variables belong to. We factor all the constants on the right side together into one variable  $a_{ij}$ . Then we get

$$u_i^{n+1} = u_i^n + \sum_j a_{ij} (u_i^{n+1} - u_j^{n+1}) \quad (\text{A.3})$$

Which we can rewrite into a matrix - vector multiplication of the form

$$\mathbf{A} \cdot \vec{x} = \vec{b} \quad (\text{A.4})$$

by defining:

- The constant vector  $b_i := u_i^n$
- The solution vector  $x_j := u_j^{n+1}$
- And the constant matrix  $A_{ij} := \delta_{ij} \left( 1 - \sum_k a_{ik} \right) + a_{ij}$

$\mathbf{A}$  and  $\vec{b}$  are known, so we need to invert the matrix to get the result. Since the matrix' dimension is the number of particles squared, this inversion is computationally not feasible. However we can use the fact, that the  $\mathbf{A}$  is a very sparse

---

matrix, since for each particle (line number) we take only the energy transfer from and to the direct neighbours (column number) into account. Therefore we do not even need to do the full conjugate gradient method, but we can use it as an iterative method which will converge quite fast to a viable approximation of the correct solution. As our tests show, usually two or three iterations give already sufficiently accurate results.

For the algorithm to succeed, we have a few conditions on the matrix  $\mathbf{A}$ : It needs to be real, symmetric and positive definite. We have no imaginary units in our equations, so the first condition is always fulfilled. The symmetry can be easily checked, since  $a$  is already symmetric.<sup>42</sup> Physically this corresponds to the conservation of energy which should anyway be either fulfilled right away or enforced by symmetrization.

The positive definiteness can be argued like the following: In the continuous limit the matrix becomes diagonal. Positive definite for a symmetric and real matrix means that the eigenvalues are positive. In this case this corresponds to heat being transported only in the correct direction along the temperature gradient and not in both. This should also be fulfilled, however to check the general matrix  $\mathbf{A}$  for positive definiteness is not possible analytically.

As we see in the more general derivation in section 4.2.3 the full equation can be written with a 3x3 matrix for each particle pair, which has to be positive definite then. In the case of isotropic conduction this matrix is simply the unit matrix, therefore positive definiteness is automatically given.

Considering all these properties, we can solve this equation with the implicit conjugate gradient method. Written in pseudo code the algorithm looks like following:

---

<sup>42</sup>Please note, that we would have to consider the real internal energy, hence the above equation multiplied by  $m_i$ .

```

r_0 = b - A x_0
p_0 = r_0
for (k=0; true; k++) {
  a_k = r_k^t r_k / (p_k^t A p_k)
  x_{k+1} = x_k + a_k p_k
  r_{k+1} = r_k - a_k A p_k
  if (r_{k+1} small enough)
    return x_{k+1}
  c_k = r_{k+1}^t r_{k+1} / (r_k^t r_k)
  p_{k+1} = r_{k+1} + c_k p_k
}

```

---

Indices are an indicator for the iteration step and  $\hat{t}$  indicates transposition. The pseudo code is basically taken from [Saad, 2000] page 191.

## Anisotropic formulation: The split up approach

For the more complicated approach of equation 4.2.12 we have to reconsider how to build up the matrix. Again we can look at the magnetic field term isolated, the other one is handled like the isotropic implementation above. Plugging in all the short hand notation we had in section 4.2 and discretizing similar to before, we get the following:<sup>43</sup>

$$\begin{aligned}
u_i^{n+1} = u_i^n + \frac{\mu(\gamma - 1)\Delta t}{k_B} \\
\cdot \sum_j m_j \left[ \frac{\kappa_j}{\rho_j^3} \left( \hat{B}_j \cdot \sum_k m_k (u_k^{n+1} - u_j^{n+1}) \nabla_j W_{jk} \right) \hat{B}_j \right. \\
\left. + \frac{\kappa_i}{\rho_i^3} \left( \hat{B}_i \cdot \sum_k m_k (u_k^{n+1} - u_i^{n+1}) \nabla_i W_{ik} \right) \hat{B}_i \right] \cdot \nabla_i W_{ij}
\end{aligned} \tag{A.5}$$

To translate this equation into the form matrix times vector we need some intermediate steps which however resemble, what we did before. We will formulate

---

<sup>43</sup>We omit the index  $B$  of all  $\kappa$  to avoid confusion with the particle index

the two sums as the product with two matrices and later combine them (due to associativity) to one final matrix.

At first we have a look at the first term with the inner sum and abbreviate all the constants:

$$\sum_k \frac{m_k \kappa_j}{\rho_j^3} (u_k^{n+1} - u_j^{n+1}) (\hat{B}_j \cdot \nabla_j W_{jk}) \hat{B}_j = \sum_k b_{jk} (u_k^{n+1} - u_j^{n+1}) \quad (\text{A.6})$$

Then we can define the matrix

$$B_{jk} = b_{jk} - \delta_{jk} \sum_l b_{jl} \quad (\text{A.7})$$

for which holds, that

$$\sum_k b_{jk} (u_k^{n+1} - u_j^{n+1}) = \sum_k B_{jk} u_k^{n+1} =: v_j^{n+1} \quad (\text{A.8})$$

We can identify this term in equation A.5 a second time for  $j \rightarrow i$ . Now we calculate analogously for the outer sum over  $j$ . Plugging in equation A.8 we get

$$\begin{aligned} & \frac{\mu(\gamma-1)\Delta t}{k_B} \sum_j m_j (v_j^{n+1} + v_i^{n+1}) \nabla_i W_{ij} \\ &= \sum_j a_{ij} (v_j^{n+1} + v_i^{n+1}) \\ &= \sum_j A_{ij} v_j^{n+1} \end{aligned} \quad (\text{A.9})$$

with

$$A_{ij} = a_{ij} + \delta_{ij} \sum_m a_{im} \quad (\text{A.10})$$

At last we need to collect the remaining  $u_i^{n+1}$  which gives an additional  $\delta_{ik}$  and we subtract our previous findings to combine everything to one single matrix:

$$\begin{aligned} C_{ik} &= \delta_{ik} - \sum_j A_{ij} B_{jk} \\ &= \delta_{ik} + \sum_j \left[ \delta_{ij} \sum_m a_{im} + a_{ij} \right] \left[ \delta_{jk} \sum_l b_{jl} - b_{jk} \right] \end{aligned} \quad (\text{A.11})$$

For which holds, that

$$\sum_k C_{ik} u_k^{n+1} = u_i^n \quad (\text{A.12})$$

Now we can check the properties of this matrix  $\mathbf{C}$ . To verify the symmetry under exchange of  $i$  and  $k$ , we multiply the brackets out and check the resulting four terms independently in the  $j$ -sum:

1.  $\sum_j \delta_{ij} \sum_m a_{im} \cdot \delta_{jk} \sum_l b_{jl} = \delta_{ik} \sum_m a_{im} \sum_l b_{il}$   
is symmetric because of the delta function ✓
2.  $-\sum_j \delta_{ij} \sum_m a_{im} \cdot b_{jk} = -\sum_m a_{im} \cdot b_{ik}$   
has no defined symmetry, since the density and the magnetic field in  $b$  are not symmetrized and the kernel derivative in  $a$  changes ✗
3.  $\sum_j a_{ij} \cdot \delta_{jk} \sum_l b_{jl} = a_{ik} \cdot \sum_l b_{kl}$   
has no defined symmetry.  $a$  is antisymmetric, however the kernel derivative in  $b$  changes ✗
4.  $-\sum_j a_{ij} \cdot b_{jk}$   
has no defined symmetry, since the kernel in  $a$  as well as in  $b$  change ✗

So we can leave out the first term in the sum and also the  $\delta$  function before the sum for further checks. Since we do not see a term wise symmetry in the terms 2-4, we sum them again up and try to find an overall behaviour. Renaming the summation indices and plugging in  $a$  and  $b$  we get

$$\begin{aligned} & \sum_j (-a_{ij} b_{ik} + a_{ik} b_{kj} - a_{ij} b_{jk}) \\ &= \frac{\mu(\gamma-1)\Delta t}{k_B} \sum_j \left[ -\frac{m_j m_k \kappa_i}{\rho_i^3} (\hat{B}_i \cdot \nabla_i W_{ik}) (\hat{B}_i \cdot \nabla_i W_{ij}) \right. \\ & \quad + \frac{m_k m_j \kappa_k}{\rho_k^3} (\hat{B}_k \cdot \nabla_k W_{kj}) (\hat{B}_k \cdot \nabla_i W_{ik}) \\ & \quad \left. - \frac{m_j m_k \kappa_j}{\rho_j^3} (\hat{B}_j \cdot \nabla_j W_{jk}) (\hat{B}_j \cdot \nabla_i W_{ij}) \right] \quad (\text{A.13}) \end{aligned}$$

---

We can ignore the masses again, since we would have to multiply the whole equation by  $m_i$  anyway and each term contains all three mass terms. After we exchange  $i \leftrightarrow k$ , we see that:

- The new term **1** matches up the old term **2**
- The new term **2** matches up the old term **1**
- The new term **3** matches up the old term **3**

Therefore the matrix in total is symmetric and valid for the algorithm. The matrix should also be positive definite, due to the same argument as before. But this time we really cannot check this analytically. However we presented some thoughts on this matter from a physical point of view in section 4.2, where we argue that the positive definiteness should be fulfilled.

## Final anisotropic formulation

Now we can come to the last approach we discussed (section 4.2.3) and show how to write equation 4.2.37 in conjugate gradient formalism. As we have already stated in the corresponding subsection, this is very similar to the isotropic case. Nevertheless we will show the full solution for the sake completeness.

Discretizing the timestep we get for the part along the magnetic field lines

$$u_i^{n+1} = u_i^n + \sum_{j=1}^{N_{ngb}} c_{ij} (u_i^{n+1} - u_j^{n+1}) \quad (\text{A.14})$$

with

$$c_{ij} = -\frac{(\gamma - 1)\mu}{k_B} \cdot \frac{m_j \Delta t}{\rho_i \rho_j} \cdot \frac{\vec{x}_{ij}^\top}{|\vec{x}_{ij}|^2} \left( \tilde{\mathbf{A}}_i + \tilde{\mathbf{A}}_j \right) \nabla_i W_{ij} \quad (\text{A.15})$$

We can then write this as the matrix equation

$$\mathbf{C} \cdot \vec{x} = \vec{b} \tag{A.16}$$

with:

- $C_{ij} := \delta_{ij} (1 - \sum_k c_{ik}) + c_{ij}$
- $x_j := u_j^{n+1}$
- $b_i := u_i^n$

Finally we have to check again the conditions for the conjugate gradient method to work properly:

We see, that the total energy is conserved since  $\tilde{\mathbf{A}}$  and therefore  $\mathbf{c}$  and  $\mathbf{C}$  are symmetric.

For the isotropised version we get the same equations just without the tilde above each  $\mathbf{A}$ .

We argued about positive definiteness already in section 4.2.3: The fully anisotropic formulation can violate this condition which can lead to non-physical heat flows as well as numerical instabilities since the method in principle requires it to be given. The isotropised version is constructed such, that in definitely fulfils positive definiteness.



## Appendix B The second order error term

In this appendix we want to present the detailed calculations for the second order error term in the Taylor approximation of section 4.2.3. We will evaluate all the different cases of equation 4.2.17 depending on the different possibilities for the four indices:

$$T_{\alpha\beta\gamma\delta} = \int d^3\vec{x}_j \frac{(\vec{x}_{ij})_\alpha (\vec{x}_{ij})_\beta (\vec{x}_{ij})_\gamma (\vec{x}_{ij})_\delta}{|\vec{x}_{ij}|^3} \cdot W'_{ij} \quad (\text{B.1})$$

We distinguish between the following three cases, which we will address one after another:

1. At least three indices are unequal
2. All indices are equal
3. The indices form two pairs, e.g.  $\alpha = \beta$  and  $\gamma = \delta$

### 1. At least three indices are unequal

If at least three of the four indices are unequal, then there is at least one integration where the integrand contains only a single  $\vec{x}_{ij}$  component. Since the denominator and  $W'_{ij}$  are even functions with respect to  $\vec{x}_j$ , the integrand for this component is in total an odd function which will vanish when integrating over the whole (symmetric!) domain. Therefore the whole integral is equal to zero.

### 2. All indices are equal

If all indices are equal, we start the calculations with substituting the integration variable  $\vec{x}_j \rightarrow \vec{x}_{ij}$  without further implications on the integration. Then equation 4.2.17 simplifies to

$$T_\alpha = \int d^3\vec{x}_{ij} \frac{(\vec{x}_{ij})_\alpha^4}{|\vec{x}_{ij}|^3} \cdot W'_{ij} \quad (\text{B.2})$$

Using a short hand notation  $T_\alpha := T_{\alpha\alpha\alpha\alpha}$ .

Since  $W'_{ij}$  is only dependent on  $|\vec{x}_{ij}|$  we go over to spherical coordinates for  $\vec{x}_{ij}$ .

---

We can arbitrarily choose the rotation of our coordinate system. For simplicity we let  $(\vec{x}_{ij})_\alpha$  be along the  $z$ -axis of the coordinate system. This gives us

$$T_\alpha = \int dr \int d\phi \int d\theta r^2 \sin \theta \cdot (r \cos \theta)^4 \cdot \frac{W'(r)}{r^3} \quad (\text{B.3})$$

We can easily perform the  $\phi$  and  $\theta$  integrations and get

$$\begin{aligned} T_\alpha &= 2\pi \left[ -\frac{1}{5} \cos^5 \theta \right]_0^\pi \int dr r^3 W'(r) \\ &= \frac{4\pi}{5} \int dr r^3 W'(r) \end{aligned} \quad (\text{B.4})$$

Next we perform a partial integration, where the boundary term vanishes, since the kernel is monotonically decreasing towards zero. It remains:

$$T_\alpha = -\frac{12\pi}{5} \int dr r^2 W(r) \quad (\text{B.5})$$

For further calculations we can either choose a proper normalised kernel, like the Gaussian given by [Price, 2012], to integrate this equation or we stay with the general  $W$  and instead reconsider the normalisation condition of the kernel given by equation 3.1.2:

$$\int_V d\vec{x}_{ij} W(\vec{x}_{ij}) = 1 \quad (\text{B.6})$$

Translating this equation into spherical coordinates and evaluating the  $\phi$  and  $\theta$  integrations we get for every kernel:

$$\int dr r^3 W'(r) = \frac{1}{4\pi} \quad (\text{B.7})$$

Therefore the overall result for this case is:

$$T_\alpha = -\frac{3}{5} \quad (\text{B.8})$$

### 3. The indices form two pairs

This last case can be calculated pretty similar, except that we have to chose two indices, which have to be unequal, here. We take  $\alpha = 1$  and  $\beta = 3$ . Again written in a spherical coordinate system we get

$$T_{\alpha\beta} = \int dr \int d\phi \int d\theta r^2 \sin \theta \cdot (r \sin \theta \cos \phi)^2 \cdot (r \cos \theta)^2 \cdot \frac{W'(r)}{r^3} \quad (\text{B.9})$$

Using our results from the  $r$ - integration before we get

$$T_{\alpha\beta} = \underbrace{\int dr r^3 W'(r)}_{-\frac{3}{4\pi}} \underbrace{\int d\phi \cos^2 \phi}_{\pi} \underbrace{\int d\theta \sin^3 \theta \cos^2 \theta}_{\frac{4}{15}} = -\frac{1}{5} \quad (\text{B.10})$$

Putting everything together we arrive at the result stated in eq. [4.2.18](#):

$$T_{\alpha\beta\gamma\delta} = \begin{cases} -\frac{3}{5} & \text{if } \alpha = \beta = \gamma = \delta \\ -\frac{1}{5} & \text{if } \alpha = \beta \neq \gamma = \delta \\ -\frac{1}{5} & \text{if } \alpha = \gamma \neq \beta = \delta \\ -\frac{1}{5} & \text{if } \alpha = \delta \neq \beta = \gamma \\ 0 & \text{else} \end{cases} \quad (\text{B.11})$$



## Appendix C Complex integration

In section 4.3.2 we used some integrations of Gaussian (or Gaussian like) integrals with complex exponents. In this appendix we want to provide the complex integration including all details of the calculations.

The first integral we want to solve is the following complex Gaussian:

$$\int_{-\infty}^{\infty} dx e^{-(x+iy)^2} = ? \quad (\text{C.1})$$

For the special case  $y = y_0 = \text{const.}$  In other words, we want to prove, that equation 4.3.11 holds also for a complex exponent.

The main tool which we will use is the so called **Residue theorem** [Bronstein et al., 2008].

Let  $\Gamma$  be a closed curve in complex space and  $\text{Res}(f, a_k)$  the residue of  $f$  at  $a_k$ , then it holds that

$$\oint_{\Gamma} f(z) dz = 2\pi i \sum \text{Res}(f, a_k)$$

With the sum over all poles  $a_k$  enclosed by  $\Gamma$ .

Since the Gaussian has no residues, the right side simply vanishes and we can replace any integration path in the complex plane by another one with the same start and endpoint. To evaluate the given integral we chose the following path<sup>44</sup>, which we illustrate in figure 50:

$$\int_{-\infty}^{\infty} dx e^{-(x+iy)^2} = \int_{y_0}^0 d(iy) e^{-z^2} \Big|_{x=-\infty} + \int_{-\infty}^{\infty} dx e^{-z^2} \Big|_{y=0} + \int_0^{y_0} d(iy) e^{-z^2} \Big|_{x=\infty} \quad (\text{C.2})$$

Using that

$$e^{-z^2} \Big|_{x=\pm\infty} = e^{-(x+iy)^2} \Big|_{x=\pm\infty} = 0 \quad (\text{C.3})$$

<sup>44</sup>The additional  $i$  in the integrations along the imaginary axis comes from the fact, that the complex plane is defined as  $x - iy$ -plane.

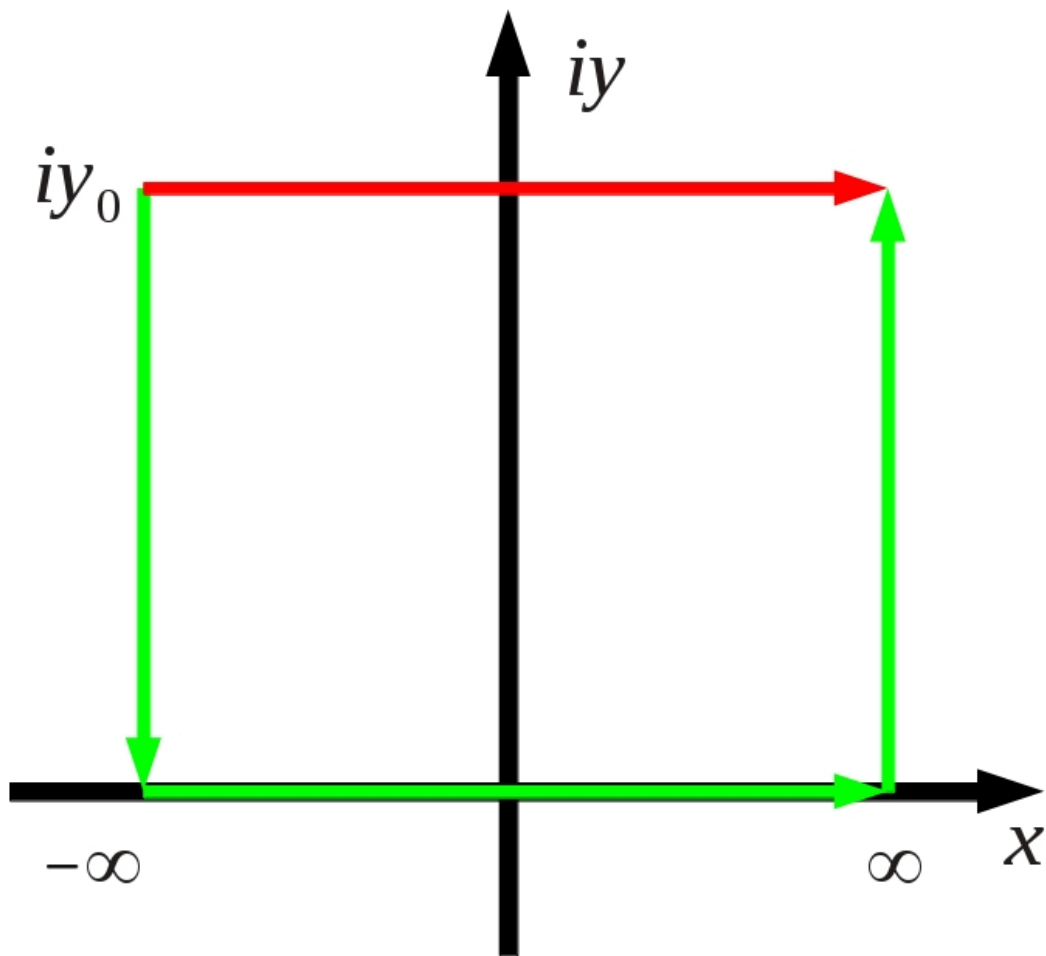


Figure 50: Alternative path for the integration in the complex plane. Instead of integrating the red way, we take the green one, which is equivalent due to the residual theorem. The three parts of this way correspond to the three terms in equation C.2.

we see, that only the integration along the real axis with imaginary part equal to zero remains and we see that equation 4.3.11 can indeed be used.

Otherwise for finite integral boundaries the calculation differs quite a bit.

We integrate a general integral of the form

$$\int_a^b dx e^{-\frac{(x-c-id)^2}{f}} = ? \quad (\text{C.4})$$

We will use the same kind of alternative path as before shown in figure 50 except that the integration boundaries of the second part are now finite. Therefore we will get error functions instead of the results of Gaussian integrals.

We start with the substitution:

$$\frac{x-c}{\sqrt{f}} \rightarrow x \quad (\text{C.5})$$

and integrate

$$\sqrt{f} \int_{\frac{a-c}{\sqrt{f}}}^{\frac{b-c}{\sqrt{f}}} dx \exp \left[ - \left( x - i \frac{d}{\sqrt{f}} \right)^2 \right] = ? \quad (\text{C.6})$$

Now we split the integral into the three shown paths. At first we integrate along the imaginary axis:

$$\begin{aligned} \sqrt{f} \int_{-\frac{d}{\sqrt{f}}}^0 d(iy) e^{-(x+iy)^2} \Big|_{x=\frac{a-c}{\sqrt{f}}} &= \sqrt{f} \int_{\frac{a-c}{\sqrt{f}} - i \frac{d}{\sqrt{f}}}^{\frac{a-c}{\sqrt{f}}} dy e^{-y^2} \\ &= \sqrt{f} \left[ \int_0^{\frac{a-c}{\sqrt{f}}} dy e^{-y^2} - \int_0^{\frac{a-c}{\sqrt{f}} - i \frac{d}{\sqrt{f}}} dy e^{-y^2} \right] \\ &= \frac{\sqrt{\pi f}}{2} \left[ \operatorname{erf} \left( \frac{a-c}{\sqrt{f}} \right) - \operatorname{erf} \left( \frac{a-c}{\sqrt{f}} - i \frac{d}{\sqrt{f}} \right) \right] \end{aligned} \quad (\text{C.7})$$

The next integral is along the real axis:

$$\sqrt{f} \int_{\frac{a-c}{\sqrt{f}}}^{\frac{b-c}{\sqrt{f}}} dx e^{-(x-iy)^2} \Big|_{y=0} = \frac{\sqrt{\pi f}}{2} \left[ \operatorname{erf} \left( \frac{b-c}{\sqrt{f}} \right) - \operatorname{erf} \left( \frac{a-c}{\sqrt{f}} \right) \right] \quad (\text{C.8})$$

---

And the integral back along the imaginary axis:

$$\begin{aligned} \sqrt{f} \int_0^{-\frac{d}{\sqrt{f}}} d(iy) e^{-(x+iy)^2} \Big|_{x=\frac{b-c}{\sqrt{f}}} & \quad (C.9) \\ & = \frac{\sqrt{\pi f}}{2} \left[ \operatorname{erf} \left( \frac{b-c}{\sqrt{f}} - i \frac{d}{\sqrt{f}} \right) - \operatorname{erf} \left( \frac{b-c}{\sqrt{f}} \right) \right] \end{aligned}$$

In total we get the result

$$\int_a^b dx e^{-\frac{(x-c-id)^2}{f}} = \frac{\sqrt{\pi f}}{2} \left[ \operatorname{erf} \left( \frac{b-c}{\sqrt{f}} - i \frac{d}{\sqrt{f}} \right) - \operatorname{erf} \left( \frac{a-c}{\sqrt{f}} - i \frac{d}{\sqrt{f}} \right) \right] \quad (C.10)$$

Which is exactly the same, as if we had integrated without using the complex plane.<sup>45</sup>

---

<sup>45</sup>For details about the error function please see the integrations in section [4.3.1](#).

# Acknowledgement

I want to take this opportunity to thank my family, friends and colleagues who have given me the possibility and helped me to come this far.

First of all thank you very much Harald for your support not only during this Masters project but for all the years since I attended your lectures for the first time in my Bachelor studies. Without your help and constant encouragement I would not be here right now.

Thank you Klaus for giving me so much support with my numerical work and the possibility to always show up in your office to ask a lot of questions.

Thanks a lot Alex for this great year and especially all the good advice you have given me. It was (and still is) a great pleasure to work with you.

Furthermore a big thanks to my parents and grandparents for the financial support they have given me.

Finally a special thanks goes to my friends Marco Häuser and Ralph Müller who always had time for me to annoy them with calculations and all the problems I encountered during my work. Thanks a lot Marco for taking so much time to read this whole thesis and give me a lot of useful comments.

Also thanks to my other colleagues and friends for all the useful discussions we had.



# Declaration of academic integrity

I hereby declare that this thesis is my own work and that I have not used any sources and aids other than those stated in the thesis.

München, September 11, 2013

---

Alexander Arth